Defects in Hard-Sphere Colloidal Crystals

Thesis advisor: Frans Spaepen Maria Christina Margareta Persson Gulda

Defects in Hard-Sphere Colloidal Crystals

Abstract

Colloidal crystals of 1.55 μm diameter silica particles were grown on {100} and flat templates by sedimentation and centrifugation. The particles interact as hard spheres. The vacancies and divacancies in these crystals are not in equilibrium, since no movement of single vacancies is observed. The lack of mobility is consistent with the extrapolation of earlier simulations at lower densities. The volume of relaxation of the vacancy has a plausible value for these densities as the volume of formation is approaching the volume in a close-packed crystal. The volume of relaxation for the divacancy is smaller than that of two vacancies, so that the association of two vacancies into a divacancy requires extra volume, and hence extra entropy. The mean square displacement of the nearest neighbors of the vacancies is an order of magnitude larger than that of the nearest neighbors of particles. The mobility of the divacancies is consistent with the extrapolation of older simulations and is similar to that associated with the annihilation of the vacancy-interstitial pair. The volume of motion of the divacancies is $\Delta V_m = 0.19 V_o$ (V_o: close-packed volume) and the entropy of motion is $\Delta S_m = 0.49 k_B T$. Dislocation-twin boundary interactions can be observed by introducing strain via a misfit template. The dislocations formed are Shockley partials. When a dislocation goes through the boundary, two more dislocations are created: a reflected dislocation and one left at the boundary, both with the same magnitude Burgers vector. The dislocations relieve a to-

tal of about a third of the misfit strain. The remaining strain is sufficiently large to move the dislocation up to the boundary and close to sufficient to move the dislocation through the boundary. A small amount to extra strain energy is needed to cause nucleation of the two additional dislocations after a waiting time.

For two important mentors:

Uriel Nauenberg and Frans Spaepen.

Contents

Acknowledgements

First, I would like to thank my adviser Professor Frans Spaepen for always finding the time to guide, advice, and encourage my work throughout my PhD. His enthusiasm and encouragement have meant a lot to me. I also would like to thank Frans for the breadth of the education he has given me. No matter if it is science, current affairs, or words origins and meanings, our discussions have always been delightful. I am very grateful for the time he has allowed me to be a part of his lab.

Secondly, I would like to thank labmate Katharine Jensen for countless hours of help and for being a fantastic friend. I am convinced that Kate will become a successful professor, and, more importantly, an incredible adviser and mentor, if she so chooses that path.

I would like to thank all members of our group who have, through the years, enlightened my day. Professor Eric Maire spent a year with us and I learned a great amount from his experience and his approach to tackling research problems. I also very much enjoyed our conversations and laughs. Some of the most fun experiments were conducted together with Professor

Maire. Furthermore, Roxanne was a good mentor my first year, sharing office space with Demet and Emily through the years has always led to many laughs, and Ingo, Nobutomo, and Fei have all been a pleasure to get to know and work with. I would like to thank Dan Pennochio, who I never personally worked with, but whose data I used for some of my analyses. I would also like to thank Adrian from the group next door for distracting me with delicious homemade cakes and fun topics to debate.

Peter Schall, who did much of the work on which this thesis is based, has been generous with his time and offered many helpful discussions.

Outside of lab, I would like to thank Winthrop House for allowing me to be a part of their vibrant, talented, and incredibly welcoming community for three years as a house tutor. I have found many valuable friends to keep for life amongst the House's leadership, colleagues, staff, and students. My time at Harvard could not have been more enriching.

One person that has had a significant impact on my life is golf coach Anne Kelly at University of Colorado, Boulder. Without her belief in me and her encouragement, I would never have got the opportunities that I have been so fortunate to experience so far. I also like to thank Professor Uriel Nauenberg who gave me the time and space to discover the greater questions research has to offer.

I would like to thank friends back home for being tremendously valuable to me through my early school years and beyond. Life has been incredibly fun every time we come together. You mean a lot to me even though we have spent most of the past 10 years far apart.

Lastly, and most of all, I would like to thank my family, who have

always been very close to me. My sister, Charlotte, for always being there when I need her. There is no more loyal person in the whole world and I am incredibly fortunate to have her as my sister. My life in America has been an amazing experience, but it has been challenging at times to be so far away from home. Having my sister next door has been invaluable. My parents, Britt-Marie and Hans, have always supported, encouraged, and challenged me when needed. When no one else has believed in me, they have, without even the slightest doubt. They have given me unconditional love throughout my whole upbringing and I could never thank them enough for it. I would never be the person I am today, and I could never have fulfilled all my dreams, without them.

List of Figures

List of Tables

1

Introduction

Collodial crystals can be studied to mimic atomic crystals [1] [2]. Due to the size of atoms, observing atomic crystals can be difficult because the resolution at such a small scale is limited, and the time scale at which movements happens is faster than the imaging processing. Therefore, scientists through the years have sought alternative methods to study atomic interactions. One such model was developed by Lawrence Bragg, who invented the bubble raft where small soap bubbles formed close-packed 2D

crystals [3]. Locally, the 2D crystals could be perfect, but grain boundaries were observed when crystals were grown on a larger scale. Other defects could also be introduced. Vacancies could be created by destroying single bubbles and watching them migrate. Dislocations were studied by performing compression and shear. This model worked very well in 2D, but it was not effective for 3D observation.

A better 3D model is the hard-sphere system. Colloidal crystals can be used as a hard-sphere system in which point and line defects are created during growth. The defects can also be introduced by manipulating the growth [4] [5] or by using external forces on an already grown crystal [6]. The best way to observe these crystals and their defect interactions is confocal microscopy [7]. This thesis covers some aspects of point and line defects in hard-sphere colloidal crystals and their interactions.

Chapter 2 focuses on the methods and theory of obtaining colloidal crystals with different orientations, structures, and defect densities. The formation of hard-sphere crystals driven by entropy and volume fraction is described. The important ingredients for successful synthesis of a colloidal system that can easily be observed and imaged in a confocal microscope are provided. A large part of the chapter is devoted to the actual fabrication steps involved in growing a crystal.

Chapter 3 explores point defects, with a particular emphasis on vacancies. Statistical measurements are made of volumes, concentrations, and movement. There have been computer simulations of hard-sphere systems [8] [9] and experiments on colloidal crystals [10], but no work so far has shown experimental vacancy motion in hard-sphere colloidal crystals. A

straightforward method for finding the vacancies in the crystal is described. Moving vacancies are found close to distortions, grain boundaries, and dislocation lines, but no single vacancies move. In contrast, motion can be observed for divacancies and the jump frequency can be compared to previous simulation work at lower densities. Also, interstitials next to vacancies are briefly discussed.

Chapter 4 investigates the interaction between a twin boundary and a dislocation. Many experiments and simulations have been performed on this topic [11] [12], but this experiment offers a unique view of the interaction on the particle level. The dislocation - twin boundary interaction is important in order to understand work hardening, yield stress, and ductility of a material [13]. Grain boundaries in general are well-known to hinder the motion of dislocations, leading to higher yield strength [13]. However, grain boundaries can also decrease the elongation to failure ratio in a tensile test; in other words, decrease the ductility of the material. Simulations and experiments on dislocation - twin boundary interactions indicate that a dislocation can be divided into two parts, one that piles up in the boundary and one that penetrates [14] [15] [16]. This leads to higher yield strength and leaves the ductility unchanged, and therefore increases the overall toughness of the material [16]. In this chapter a Shockley partial dislocation in a face-centered cubic (FCC) crystal, introduced by lattice strain, moves towards a Σ 3 $\{111\}$ twin boundary during the growth of the colloidal crystal. When the partial dislocation hits the boundary, the motion stops for a while before penetration, indicating that a build-up in strain energy by the growth of the crystal is needed to drive the process.

2

Methods and Theory for Obtaining and Observing a Colloidal Hard-Sphere Crystal

Hard-sphere colloidal particles are ten thousand times larger than atoms, but the behavior of defects in their respective crystals are strikingly similar. This chapter will give a detailed description to how one can obtain colloidal crystals with different structures and orientation, as well as how to introduce defects. An overview of methods for observing and securing particle locations is given as well.

2.1 Colloidal Suspension

2.1.1 Recipe

The colloidal particles in this experiment were provided by mircomod Partikeltechnologie GmbH. They are amorphous silica particles with a diameter, d, of 1.55 μm, polydispersity, σ/d (σ: variance), <3.5%, and a density of 2.0 g/cm^3, which gives a mass of 3.9×10^{-15} kg. This raw stock of colloids (1.5%) is mixed into a solution with deionized water (35.4%), dimethyl sulfoxide (DMSO) (61.9%) and fluorescein (1.2%). The DMSO is used for matching the index of refraction between the colloids and the solution. This is important for two reasons: 1) it makes it possible to scan deep into the sample with a confocal microscope, since scattering from particles above and below is limited; 2) it minimizes van der Waals forces between the particles, which is important to obtain a hard-sphere interaction between the spheres. The fluorescein is used to create a good contrast between the colloids and the fluid in the microscope (the particles appear as black dots in the bright scattering liquid). The fluorescein also adds some salt ions, which reduces the Debye screening length to less than 10 nm [17]. The density of the solution is just a little higher than that of water, 1.10 g/cm^3. Sometimes, a more concentrated version of colloids is desirable. With more colloids in the suspension, the crystal grows higher. If more raw stock is added to the suspension to obtain a new total fraction, $f_{RawStock}$, the fraction of water, f_{water}, decreases in order that the index of refraction of the water-DMSO

solution remains the same:

$$f_{water} = 0.369\% - f_{RawStock} \tag{2.1}$$

The fraction $f_{RawStock}$ is used to predict experimental crystal height in Section 2.16.

2.1.2 Minimization of polydispersity

The polydispersity of the raw stock $\frac{\sigma}{d}$ has been measured to be <3.5% [17]. In order to improve the polydispersity further and remove secondary particles, the colloidal suspension is sonicated and vortexed, then left to have the colloids settle for about 3 hours. This time is determined by the settling velocity, $v_{settling}$. These colloids accelerate due to gravity, g, until the drag force, F_d, equals the gravitational force F_g. At that moment, the colloid has reached $v_{settling}$. The gravitational force is [18]:

$$F_g = mg = \frac{4}{3}\pi a^3 \Delta\rho g \tag{2.2}$$

where the radius of the sphere is a $(= d/2)$ and the difference in density between the particle and the liquid, is $\Delta\rho$. The drag force depends on the viscosity of the liquid, η, the velocity, v, and again the radius of the particle, a [18]:

$$F_d = 6\pi\eta a v \tag{2.3}$$

$v_{settling}$ is then [18]:

$$v_{settling} = \frac{4a^2\Delta\rho g}{18\eta} \tag{2.4}$$

For the conditions described above, and with viscosity, η, found to be $\sim$ 1.6×10^{-3} Pa.s [17], the settling velocity is 2.7 mm/hour (7×10^{-7} m/s). Since this velocity is proportional to a^2, a 6 hour wait (with a traveling distance of 16mm) before the colloids are drawn from the sample is sufficient to be out of the range of those particles that are half the size (with a traveling distance of 4mm) or twice as big (with a traveling distance of 64mm). Colloids are then drawn with a pipette 1-2 cm below the liquid height.

2.1.3 Choosing the particle size

The particles size needs to be small enough for gravity not to overcome the thermal energy that is the source of Brownian motion. The thermal energy of a single hard-sphere particle in a liquid is $U_{thermal} = \frac{3k_BT}{2}$. In this case the particle has 3 degrees of freedom (translational only). By comparing the thermal energy with the kinetic energy, $U_{kinetic} = \frac{mv^2}{2}$, the particles have an average Brownian velocity, $<v_b>$, of [18]:

$$< v_b >=\sqrt{\frac{3k_BT}{m}} \tag{2.5}$$

where k_B is the Boltzmann constant, T is the temperature and m is the mass of the particle. For the particles in these experiments, at room temperature, the value is 2×10^{-3}m/s, 10^4 times larger than the settling velocity [18].

2.2 Crystal Growth

2.2.1 Hard-sphere colloidal crystals are formed due to entropy

In atomic crystals, at a given pressure, the temperature determines what phase the matter exists in. For hard-sphere systems, instead, the volume fraction, ϕ, is the variable that determines the phase. Consider Helmholtz free energy, F, at constant volume:

$$F = U - TS \tag{2.6}$$

where U is the internal energy and S is the entropy. For the internal energy we only need to consider the kinetic energy of the particles, $U_{thermal} = \frac{3}{2}k_B T$, and the Helmholtz free energy becomes:

$$F = (\frac{3}{2}k_B - S)T \tag{2.7}$$

For any temperature, minimizing F occurs only by maximizing the entropy, S. The entropy depends on the volume fraction of the particles, ϕ [18]. As the volume fraction, ϕ, increases the colloidal suspension goes from a fluid phase to fluid-crystal coexistence at ϕ=0.494 and to a crystalline phase at ϕ=0.545 [19] [20], as shown in Figure 2.1. If the colloids are compressed together quickly (e.g. by centrifugation) with the right boundary conditions on a template, an amorphous structure can be obtained above ϕ=0.58 ($\sim$ glass transition) [21]. The closest-packed amorphous structure has ϕ=0.64 [22].

The equation of state for colloidal crystals is similar to that of an ideal gas. If P is the osmotic pressure, ρ is the number density of particles, k_B is the Boltzmann's constant, T is temperature, then:

$$P = \rho k_B T Z(\phi) \tag{2.8}$$

where Z is the compressibility factor that only depends on ϕ [18]. By fitting the molecular dynamics data by Alder and Wainwright [23], Hall [24] provided the following expression for the compressibility factor of a hard-sphere FCC crystal:

$$\begin{aligned} Z(\beta) = 2.557696 + 0.1253077\beta + 0.1762393\beta^2 - 1.053308\beta^3 \\ +2.818621\beta^4 - 2.921934\beta^5 + 1.118413\beta^6 + \frac{12 - 3\beta}{\beta} \end{aligned} \tag{2.9}$$

where β:

$$\beta(\phi) = 4(1 - \frac{\phi}{\phi_o}) \tag{2.10}$$

and ϕ_o is the close-packed packing fraction.

2.2.2 Crystal height

The height to which we grow the crystals is important and can be obtained from the colloid concentration of the suspension, the volume of the suspension and the volume fraction of the crystal. The company that fabricates the colloids, Micromod, specifies 50 mg silica per milliliter of raw stock, i.e. $\rho_{SilicaRawStock}$=50 mg/cm^3. The suspension of colloids used for imaging, can be made with different fractions, $f_{RawStock}$, of the raw stock. The volume of

raw stock needed is:

$$V_{RawStock} = V_{Cell} f_{RawStock} \tag{2.11}$$

where V_{Cell} is the volume in the cell that depends on the cross-sectional area of the cell, A_{Cell}, and the height to which one fills the sample h_{Cell}. Therefore, the amount of raw stock becomes:

$$V_{RawStock} = A_{Cell} h_{Cell} f_{RawStock} \tag{2.12}$$

The mass of silica in the cell, m_{Silica}, is the volume of raw stock, $V_{RawStock}$, multiplied by the density of silica in that stock, $\rho_{SilicaRawStock}$:

$$m_{Silica} = V_{RawStock} \rho_{SilicaRawStock} = A_{Cell} h_{Cell} f_{RawStock} \rho_{SilicaRawStock} \tag{2.13}$$

The volume of silica, V_{Silica}, is the mass of silica, m_{Silica}, divided by the density of silica itself, ρ_{Silica}=2 g/cm^3;

$$V_{Silica} = \frac{m_{Silica}}{\rho_{Silica}} = \frac{A_{Cell} h_{Cell} f_{RawStock} \rho_{SilicaRawStock}}{\rho_{Silica}} \tag{2.14}$$

The volume of the crystal, $V_{Crystal}$, depends on the volume of silica, V_{Silica}, and the volume fraction of the crystal, $\Phi_{Crystal}$:

$$V_{Crystal} = \frac{V_{Silica}}{\Phi_{Crystal}} = \frac{A_{Cell} h_{Cell} f_{RawStock} \rho_{SilicaRawStock}}{\rho_{Silica} \Phi_{Crystal}} \tag{2.15}$$

The volume of the crystal, $V_{Crystal}$, is the cross-sectional area of the crystal, A_{Cell}, multiplied by the height of the crystal, $h_{Crystal}$; hence the height will

not depend on the cross-sectional shape of the cell:

$$h_{Crystal} = \frac{h_{Cell} f_{RawStock} \rho_{SilicaRawStock}}{\rho_{Silica} \Phi_{Crystal}} \tag{2.16}$$

For any given $f_{RawStock}$ and $\Phi_{Crystal}$, we need to fill the cell to the height h_{Cell} in order to obtain a specific crystal height, $h_{Crystal}$:

$$h_{Crystal} = \frac{h_{Cell} f_{RawStock} 50\ mg/cm^3}{\Phi_{Crystal} 2\ g/cm^3} = 0.025\ \frac{h_{Cell} f_{RawStock}}{\Phi_{Crystal}} \tag{2.17}$$

2.2.3 Structure, orientation, and defects

When colloidal particles settled onto a flat glass slide, close-packed hexagonal crystals form with many grain boundaries, stacking faults and point defects. The crystals are random hexagonal close-packed (RHCP) where the layers occur in a random order in positions ABCACABCBA of a hexagonal close-packed layer (see Figure 2.2), rather than perfect hexagonal close-packed (HCP) with order ABABAB, or face-centered cubic (FCC) with order ABCABC. A layer in a RHCP crystal grown on a flat glass slide is shown in Figure 2.3 and 2.4. Figure 2.3 focuses on point defects where the yellow arrows indicate vacancies, the blue arrows indicate split intersitials and red arrows indicate substitutional impurities. Figure 2.4 focuses on the line defects with two dislocations indicated in red and an unrelaxed grain boundary indicated in green. The yellow triangles indicate that three crystals with the same orientation come together, which is a way to tell that the defect in between is a dislocation or stacking fault, not a grain boundary.

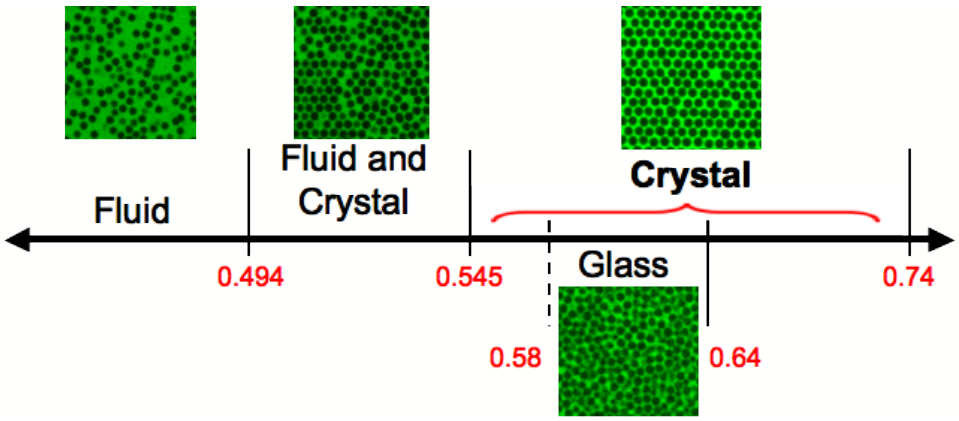

Figure 2.1: A phase diagram for hard sphere colloidal crystals. As the volume fraction, ϕ, increases the colloid solution goes from a fluid phase to fluid-crystal coexistence at ϕ=0.494 and to a crystalline phase at ϕ=0.545. If the colloids are compressed together quickly (by centrifugation) with the right boundary conditions in a template, an amorphous structure can be obtained above ϕ=0.58. The most close-packed amorphous structure has a ϕ=0.64.

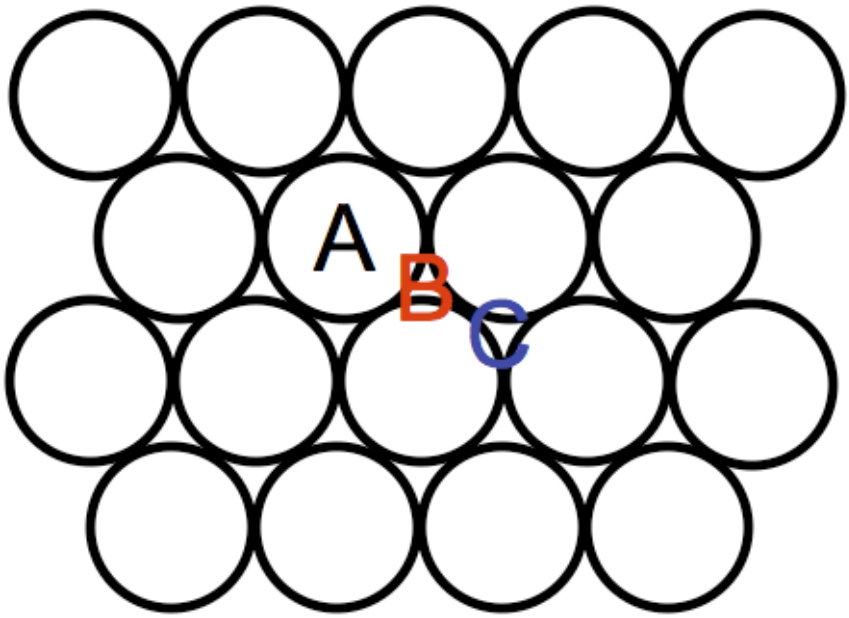

Figure 2.2: Crystal indicating position for an A (black), a B (red), and a C (blue) layer.

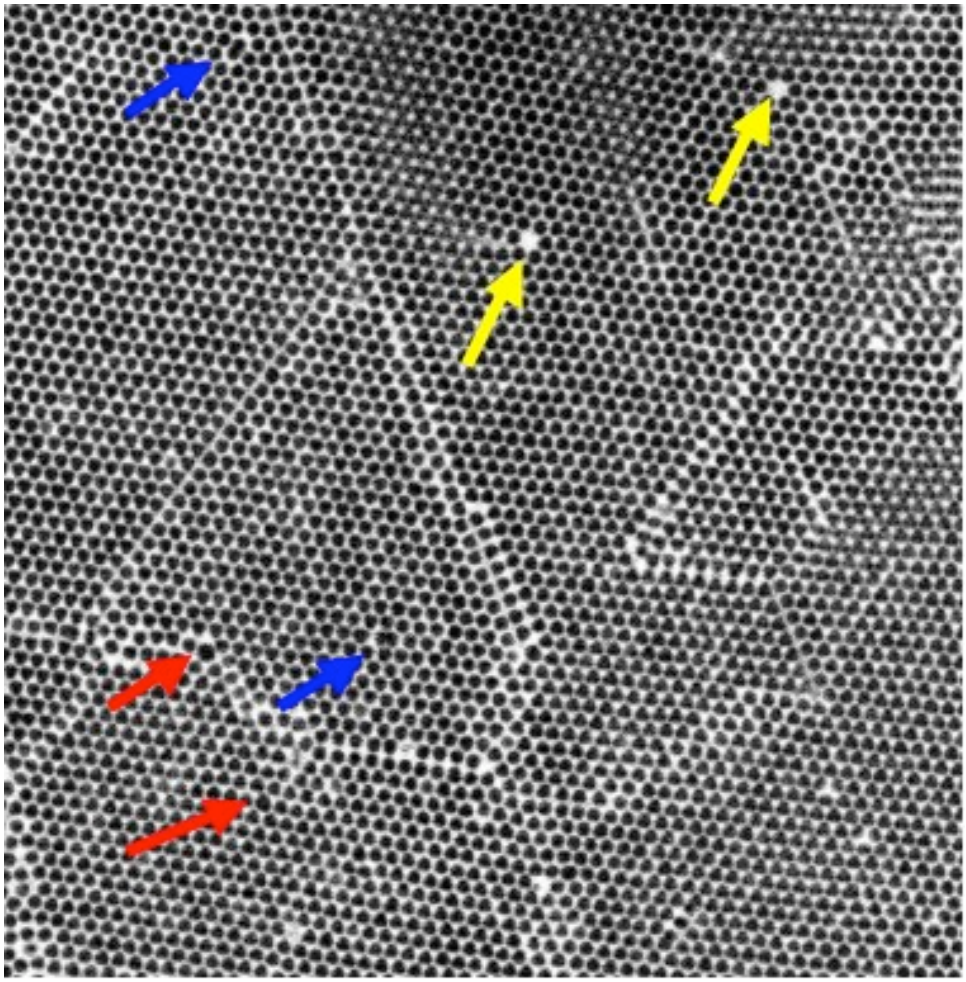

Figure 2.3: A layer in a random hexagonal close-packed crystal grown on a flat glass slide showing the point defects. The yellow arrows indicate vacancies, the blue arrows indicate split intersitials and red arrows indicate substitutional impurities.

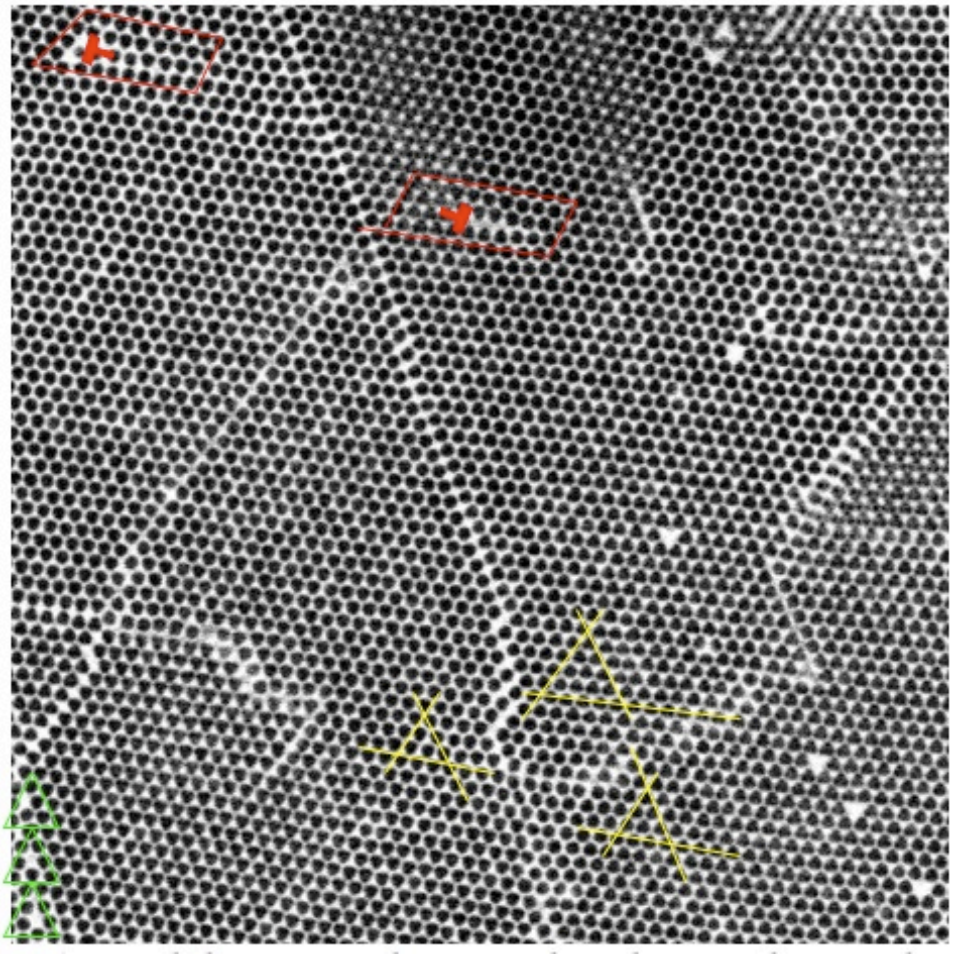

Figure 2.4: Same crystal as in Figure 2.3 with line defects. Two dislocations are indicated in red and an unrelaxed grain boundary in green. The yellow triangles reveal that three crystals with the same orientation come together, indicating either a dislocation or a stacking fault.

2.2.4 The importance of a template

If a specific structure or orientation is desired, the glass slide needs to contain a template, a pattern of holes, to direct the colloids by making them each settle into one hole. Once the first layer has been arranged, the layers above follow. Templates work very well for {100} and {110} FCC structures, in which there is only one way each layer can be arranged. However, if a {111} orientation is patterned, a RHCP will grow rather than a HCP or FCC. This is due to the two positions the next layer can chose. It could still be worthwhile to make a template even in this case if a less defective or strained crystal in the {111} orientation is desired. The ideal lattice spacing for a desired thickness of the crystal can be found from the equation of state [17]. If a particular tilt grain boundary is desired, it can be patterned into the template [5]. Amorphous structures, and an interface between an amorphous phase and a crystal can be formed on appropriate templates as well. Finally, dislocations can be introduced by either as misfit dislocations by increasing or decreasing the lattice spacing [4], or by indentation of the crystal [6]. (See Chapter 4 for more details). The crystals are grown overnight, or centrifuged in a few minutes. Centrifugation decreases the sample preparation time and leaves fewer defects, but is only ideal for {100} FCC crystals [17]. When manufacturing the templates it is also important that the holes are deep enough so that the particles have stable positions. This critical depth, d_c, corresponds to the kinetic energy from Browinian motion, $U_{kinetic} = \frac{mv_b^2}{2}$, being equal to the potential energy, mgd, where d is the depth of the hole:

$$d_c = \frac{v_b^2}{2g} \tag{2.18}$$

Given v_b above, $d_c \sim 100$nm. Our holes have been measured to be around ~ 700nm. Appendix A gives step-by-step instructions on how to make templates.

2.3 Sample Preparation

The sample preparation is straightforward once the templates and the colloidal suspension have been obtained. A small cylinder is cut from a plastic cylindrical pipette. Both the cylinder and the template are cleaned with isopropanol and dried with air. The cylinder is glued onto the glass slide with the desired pattered and cured under UV light for at least one hour. The glue used here is "Norland optical adhesive 81". Curing time depends on the amount of glue used. It is important that the cell be completely sealed to prevent leaks. The colloidal suspension, prepared using the recipe described in Section 2.1.1, is sonicated and vortexed. The desired amount of suspension is pipetted and dropped down into the cell. The sample is left on a flat dark surface overnight to crystallize. If a {100} pattern is used, a crystal can be obtained faster by centrifuging [17]. The height of the crystal is determined by the amount of raw stock colloids used $f_{RawStock}$ and the height to which the cell is filled, h_{Cell}, as discussed in Section 2.2.2.

2.4 Confocal Microscope

The optical microscope has been widely used for centuries. However, at high magnification, the depth of focus becomes limiting. Marvin Minsky invented a solution to this problem in 1957 [25]. Minsky placed a pinhole in front of the detector that blocks all light other than that from the point confocal with

the pinhole. That point is scanned in the sample by two rotating mirrors (x,y) and a translation of the sample in the z-direction (along the optic axis). The computer constructs the image from the signals given by the detector. The data presented in this work was all taken on a tandem Leica confocal microscope with a 100x objective lens.

3

Point Defects in Hard-Sphere Colloidal Crystals

Perfect crystals are very hard to find. When a crystal forms, multiple defects work themselves into the crystal. Defects can be divided into three categories; point, line, and planar. Point defects, include vacancies, interstitials, and substitutional impurities; line defects are dislocations or disclinations; and planar defects include stacking faults and grain boundaries. When sufficient time has passed, these defects should come to

equilibrium with each other. However, given the duration of our experiments, and the mobility of the defects, equilibrium is not established. This chapter will focus on vacancies and divacancies in hard-sphere colloidal crystals. There will also be a brief discussion of interstitials.

3.1 Introduction

3.1.1 Vacancies

A vacancy is an empty lattice sight that would be occupied with an atom in a perfect crystal. The colloidal hard-sphere crystals have many vacancies, just like atomic crystals. In order to understand how many vacancies to expect, one needs to turn to thermodynamics: the state of thermodynamic equilibrium at constant pressure and temperature is reached when the Gibbs free energy, G, is a minimum.

$$G = H - TS \tag{3.1}$$

Therefore, the degree to which the increase in entropy, ΔS, compensates the increase in enthalpy of forming the point defect, ΔH, determine their concentration.

When a vacancy is formed, one can imagine removing an atom from the bulk and placing it at the surface of the crystal. If there are n vacancies, ΔH is the sum of each individual enthalpy increases, Δh [26]:

$$\Delta H = n\Delta h \tag{3.2}$$

For hard-sphere crystals the internal energy is zero and ΔH only depends on the pressure, p, and the volume difference creating a vacancy, ΔV_v, called volume of formation:

$$\Delta V_v = V_p + \Delta V_{relax} \tag{3.3}$$

where V_p is the crystal volume per particle and ΔV_{relax} is the amount of volume change in the surrounding crystal due to the presence of the empty space created by removal of the particle [8]. Our enthalpy becomes:

$$\Delta H = n\, p\, \Delta V_v \tag{3.4}$$

The entropy change, ΔS, to consider is both the entropy change of configuration, Δs_c, and entropy change of vibration, Δs_v per particle. Δs_c is determined by the number of ways N particles and n vacancies can be arranged into N + n lattice sites [26]:

$$\Delta S_c = k_B ln(\frac{(N+n)!}{N!\, n!}) = k_B[(N+n)ln(N+n) - Nln(N) - nln(n)] \tag{3.5}$$

Therefore, the free energy change obtained by introducing n vacancies into a crystal is:

$$\Delta G = n\Delta h - nT\Delta s_v - k_B T[(N+n)ln(N+n) - Nln(N) - nln(n)] \tag{3.6}$$

The equilibrium vacancy concentration is obtained by minimizing the free

energy with respect to the number of vacancies:

$$\begin{aligned}\frac{\delta\Delta G}{\delta n} &= \Delta h - T\Delta s_v - k_B T[ln(N+n) + \frac{N+n}{N+n} - ln(n) - \frac{n}{n}] \\ &= \Delta h - T\Delta s_v + k_B T ln(\frac{n}{N+n}) = 0\end{aligned} \tag{3.7}$$

Therefore, the equilibrium fraction of vacancies, x_v:

$$x_v = \frac{n}{N+n} = e^{-\frac{\Delta h - T\Delta s_v}{k_B T}} \tag{3.8}$$

The vacancy equilibrium concentration for different low density hard-sphere crystals close to melting point, obtained through simulations [8], has been found to be on the order of $10^{-6} - 10^{-3}$. Numerical studies for polydispersed hard-sphere colloidal crystals have shown vacancy equilibrium concentration on the order of 10^{-4} for 3.5% polydispersity [27] and theoretical values for monodispersed crystals shows $10^{-7} - 10^{-4}$ equilibrium concentration close to freezing point, where the vacancy concentration increases with decreasing density [28].

However, ours and others experimental results for hard-sphere colloidal crystals are not at equilibrium (see later for kinetic justification). We will show that we get 10^{-3}, others get $10^{-2} - 10^{-3}$ [10].

If a particle moves into the free space of the vacancy, the vacancy moves one lattice spacing to the original position of that particle. This can occur multiple times, as a random walk through the crystal. The motion also requires that the nearest neighbors next to the particle move slightly to open up a passage. The jump frequency of the vacancy, Γ, is related to the Gibbs free energy of motion (the increase in free energy of the activated

state), $\Delta G_m = \Delta H_m - T\Delta S_m = p\Delta V_m - T\Delta S_m$, in the following way:

$$\Gamma = \nu \times exp(\frac{\Delta G_m}{k_B T}) = \nu \times exp(\frac{p\Delta V_m - T\Delta S_m}{k_B T}) \tag{3.9}$$

where k_B is the Boltzmann constant and T is the temperature. ΔV_m is the change in volume due to expansion of channel. ΔS_m is the change in local vibrational entropy. ν is the attempt frequency of the vacancy to move and can be related to the diffusion rate, D, and the jump distance, λ, in the following way [29].

$$\nu = \frac{6D}{\lambda^2} \tag{3.10}$$

Diffusivity, D, can can be expressed in terms of viscosity, η, Boltzmann constant, k_B, temperature, T, and the radius, a, by applying Stokes-Einstein equation we get [29]:

$$D = \frac{k_B T}{6\pi\eta a} \tag{3.11}$$

Since λ in Equation 3.10 is equal to two particle radii, $2a$, we can find the following expression for ν:

$$\nu = \frac{k_B T}{4\pi\eta a^3} \tag{3.12}$$

Since $k_B = 1.38 \times 10^{-23}$ J/K, $T = 300$ K, $\eta = 1.6 \times 10^{-3}$ Pa.s [17] and $a = 1.55 \times 10^{-6}/2$ μm, $\nu \sim 0.6$ sec^{-1}.

3.1.2 Divacancies

When two vacancies occur next to each other at adjacent lattice sites, they form a divacancy. In a hard-sphere crystal, the overall free energy becomes smaller when two vacancies associate even though no bonds are present. The proximity of the two vacancies could allow extra volume relaxation, ΔV_a, as well as extra space for the neighbors to sample, thereby increasing the vibrational entropy by ΔS_a. The free energy of association $\Delta G_a = p\Delta V_a - T\Delta S_a$, relates the equilibrium concentration of vacancies, x_v, and divacancies, x_{v_2} [30] [8]:

$$\frac{x_{v_2}}{x_v^2} = exp(-\frac{\Delta G_a}{k_B T}) = exp(\frac{T\Delta S_a - p\Delta V_a}{k_B T}) \tag{3.13}$$

The extra freedom of the neighbors of a divacancy also makes it easier for the associated vacancies to jump. The jump frequency of divacancies has been found in computer simulations to be larger than for vacancies in hard-sphere crystals [8]. We also will confirm this in our much denser system.

3.1.3 Intersitials

An interstitial is an atom occupying a space in a crystal which is not a lattice site. These are much less common than vacancies due to their large enthalpy of formation. If an atom inside the crystal moves into position that is not a lattice site, leaving a vacancy behind, the vacancy-intersitial pair is called a Frenkel defect. The interstitial are non-equilibrium defects and will usually fall back into the vacancy if kinetics allows [30] [26].

3.2 Analyzing Data

3.2.1 Particle locating

In this chapter two sets of data are used. First, a RHCP crystal is grown on a flat surface, and a single vacancy is slowly scanned in the confocal microscope. This "zoomed-in" {111} data-set is used to get precise measurements of how the vacancy's nearest neighbors relax into the free open space. Second, a large sample with many vacancies is recorded over time to learn about vacancy statistics and observe possible movements. This large sample is centrifuged at 2200 rpm onto a {100} oriented template, creating a 50 μm thick FCC crystal, and referred to as the "zoomed-out" {100} data-set [31]. In order to process the first set of data (the vacancy layer is shown in Figure 3.1) the following parameters were used in particle location functions presented in Appendix B.

	x	**y**	**z**
um/pixel	0.034	0.034	0.042
lnoise	2	2	2
lobject	31	31	15
diameter	35	35	19
masksz	21	21	11
xyzmax	512	512	281
sep	21	21	9

Table 3.1: Parameters used for particle location in the "zoomed-in" {111} data-set

Using the 3D mask operation described in Appendix B together with the parameters in Table 3.1, Figure 3.2 was obtained and the centers of the particles were found. For precision on the sub-micrometer scale (as this set of

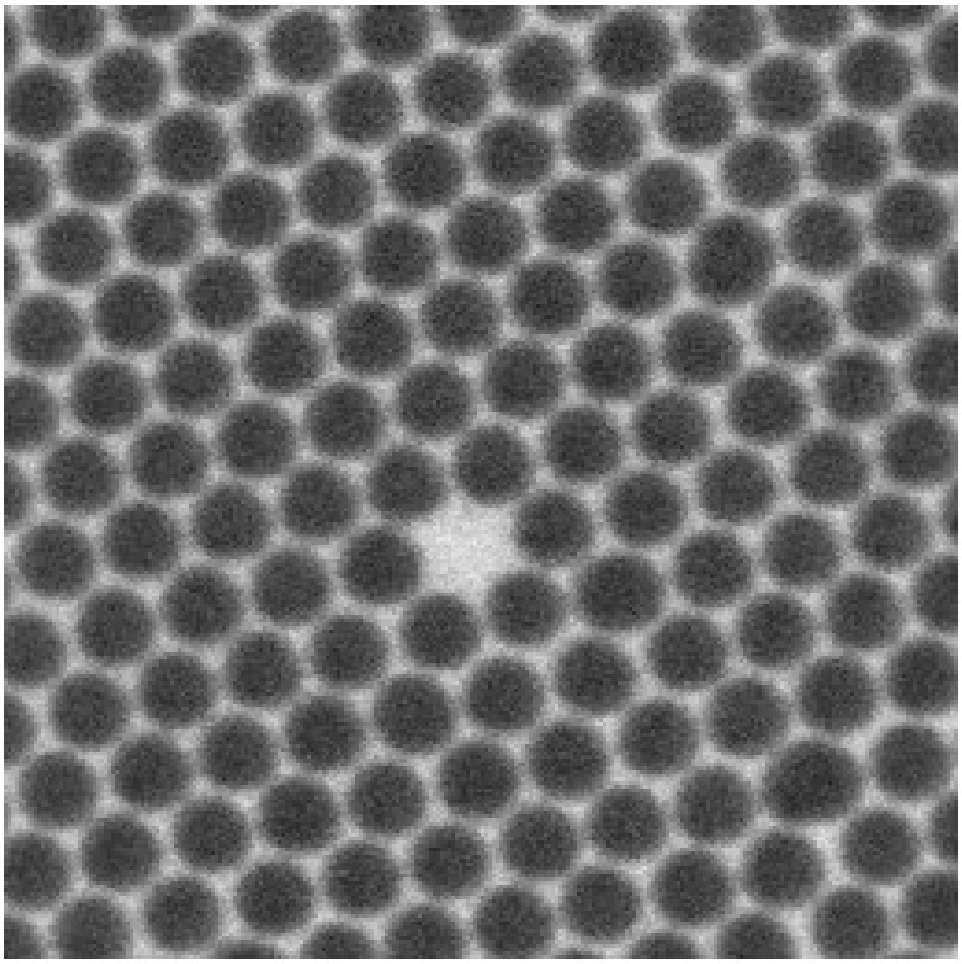

Figure 3.1: A raw 512 × 512 pixel high-resolution confocal image cutting through the middle of the vacancy in the "zoomed-in" {111} data-set.

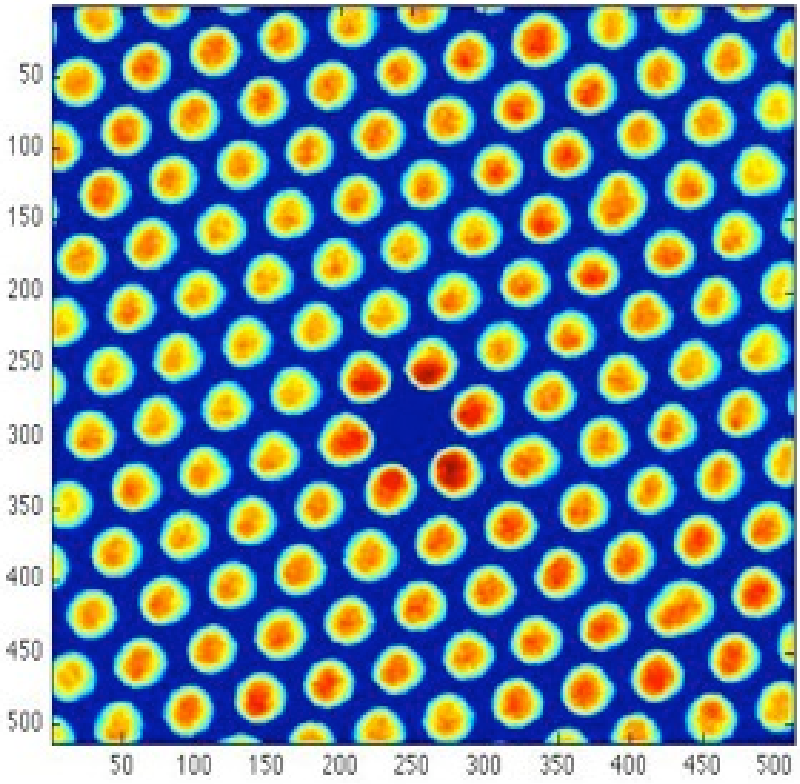

Figure 3.2: A 3D mask operation was preformed (as described as the bpass3dMB method in Appendix B) on the vacancy of in Figure 3.1 with parameters given in Table 3.1. The colors represents the intensity of the pixels in the picture which have arbitrary units, see Appendix B for more details. The more intense pixels are the ones closer to the center of the vacancy, meaning that the vacancies nearest neighbors spend more time trying to penetrate into the free space of the vacancy.

measurements requires) dimensional calibration is essential. To this purpose, a template with a {100} pattern and known dimensions was placed with its <100 >direction lined up with confocal's x-axis and its <010 >direction lined up with the confocal's y-axis. Through this method a correction with respect to the nominal microscope settings of +1% was obtained in x-direction and -4% in y-direction. To calibrate z, a more advanced method was used with the template coming in at an angle over the confocal lens [32] and a -10% correction was needed.

In the "zoomed-out" {100} data-set the particles were found with the function parameters shown in Table 3.2. Due to the size of the data set, this was only done for one quarter of the sample hence the 512 x 512 parameters for xyzmax instead of the whole set, 1024 x 1024.

	x	**y**	**z**
um/pixel	0.1515	0.1515	0.1300
lnoise	1	1	1
lobject	9	9	12
diameter	9	9	12
masksz	6	6	8
xyzmax	512	512	475
sep	3	3	4

Table 3.2: Parameters used for particle location in the "zoomed-out"{100} data-set

As before, the obtained values need to be corrected. This is done differently in this data set to above since we have a known lattice spacing in the template. The template has two repeat distances, $x_{template}$ and $y_{template}$, both equal to 1.63 μm, in two orthogonal directions. Unfortunately, the two directions are not lined up exactly with the x and y axis as in the previous calibration. Also, the template is not completely level; it has a slight tilt.

Therefore, each nearest neighbor vector has an x-, y-, and z-component in the confocal framework. Let's call these components' magnitudes ax, ay, and az for one direction with the total magnitude of $x_{template}$ and bx, by, and bz in the perpendicular direction with total magnitude $y_{template}$. The following equations can thus be obtained:

$$(ax \times \delta x)^2 + (ay \times \delta y)^2 + (az \times \delta z)^2 = x_{template}^2 \tag{3.14}$$

$$(bx \times \delta x)^2 + (by \times \delta y)^2 + (bz \times \delta z)^2 = y_{template}^2 \tag{3.15}$$

where δx, δy, and δz are the pixel/μm conversion factors. These three variables are unknown. However, we only have two equations and need a third one. To obtain the crystal spacing in z close to the template, call it $z_{template}$, we need to use the equation of state and geometry. At a crystal depth of 50 μm, the unstrained lattice parameter is 1.56 μm [17]. Imagine a unit cell with lengths x, y, and z. The body diagonal, D_{Body}, which is twice the nearest neighbor distance 1.56 μm, can be expressed as.

$$D_{Body}^2 = x^2 + y^2 + z^2 \tag{3.16}$$

Solving for z gives the following:

$$z = \sqrt{D_{Body}^2 - x^2 - y^2} \tag{3.17}$$

For an unstrained case, distances in x and y will both be d = 1.56 μm:

$$z = \sqrt{D_{Body}^2 - x^2 - y^2} = \sqrt{(2d)^2 - 2d^2} = \sqrt{2}d = \sqrt{2} * 1.56 = 2.21\mu\text{m} \tag{3.18}$$

However, both x and y are strained due to the template spacing. We know

that the strain in z, ε_z, for an isotropic system is related to the strain in x, ε_x, and y, ε_y , by Poisson's ratio, ν.

$$\varepsilon_z + \varepsilon_x\nu + \varepsilon_y\nu = 0 \tag{3.19}$$

In our case,

$$\varepsilon_{x,y} = \frac{1.63 - 1.56}{1.56} = 4.5\% \tag{3.20}$$

We take from density functional calculations [33] Poisson's ratio to be 0.37.

$$\varepsilon_z = -2\varepsilon_{x,y}\nu = -2 \times 0.045 \times 0.37 = -3.3\% \tag{3.21}$$

We can solve for $z_{template}$:

$$z_{template} = z(1 + \varepsilon_z) = 2.21 \times (1 - 0.033) = 2.14\mu\text{m} \tag{3.22}$$

A third equation can now be obtained similarly to equation 3.14 and 3.15.

$$(cx \times \delta x)^2 + (cy \times \delta y)^2 + (cz \times \delta z)^2 = z_{template}^2 \tag{3.23}$$

Calculating all nearest neighbor distances in the template plane and the distances perpendicular and close to the template, averages were made to find ax, ay, az, bx, by, bz, cx, cy, cz and solve for δx, δy, δz:

$$\delta x = 0.1538\mu\text{m/pixel} \tag{3.24}$$

$$\delta y = 0.1553\mu\text{m/pixel} \tag{3.25}$$

$$\delta z = 0.1099\mu\text{m/pixel} \tag{3.26}$$

3.2.2 Method to locate vacancies

Since the main interest with the "zoomed-out" {100} data-set was to find the center of many vacancies as time-efficiently and accurately as possible, a few methods were tried. The hope was to identify vacancies by finding significant increases in Voronoi volume for particles close to vacancies, decreases of coordination number of particles close to vacancies, or differences in nearest neighbor orientation of particles close to vacancies compared to the average particle. However, the most efficient way yet has been to invert the images before running the 3D mask method. (This is equivalent to not use the XYZ = 255-XYZ step described in Appendix B). Different parameters from those finding particles (Table 3.2) are also needed. This is due to the spacing between vacancies being much greater than for particles. The parameters used are presented in Table 3.3.

	x	**y**	**z**
μm/pixel	0.1515	0.1515	0.1300
lnoise	3	3	3
lobject	9	9	12
diameter	19	19	25
masksz	12	12	16
xyzmax	1024	1024	475
sep	7	7	9

Table 3.3: Parameters used for vacancy location in the "zoomed-out" {100} data-set

Figure 3.3 compares the same layer in the crystal with the two different 3D mask methods. The upper left image shows the 3D mask used to find particle centers. The upper right image uses the 3D mask parameters described in Table 3.3 to find vacancies. The color scale on the right represents

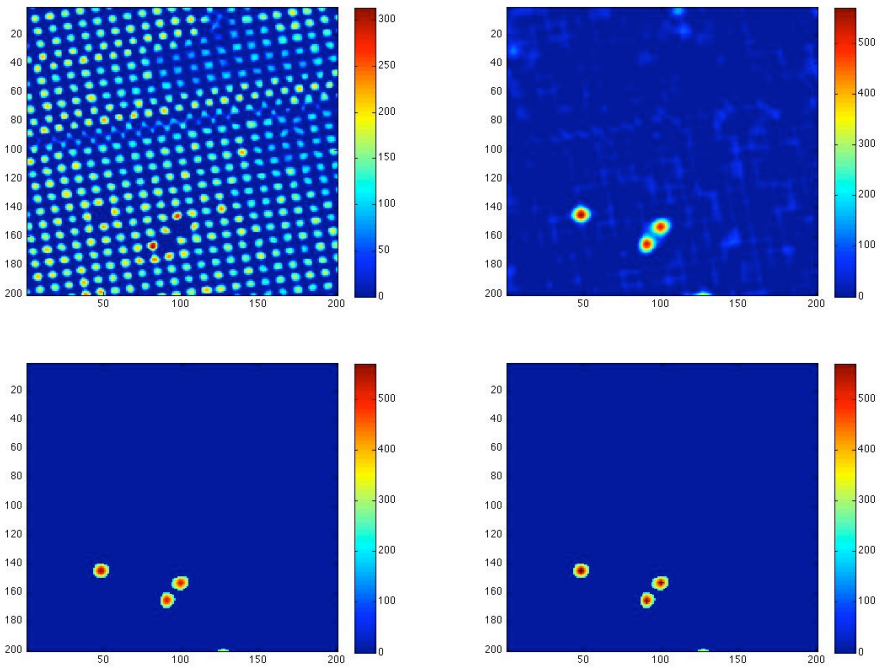

Figure 3.3: 3D mask applied to a {100} templated crystal to find particle and vacancy centers. The color scale on the right represents the intensity of the pixels in the picture, which have arbitrary units, see Appendix B for more details. The upper left image is used to locate particles. The upper right image shows the 3D mask performed on the same picture but inverted to locate vacancies. The lower left image uses a threshold of 36% of maximum pixel intensity to eliminate noise. Finally, the lower right image illustrates how to find the center of the vacancies by choosing the right parameters in the particle location method described in Appendix B.

the intensity of the pixels in the picture.

Since this 3D mask still leaves some area of undetermined space that is neither single vacancy nor divacancy, a threshold was applied to eliminate noise. Examples of noise could be grain boundaries with extra space, a stacking fault where the particles are out of plane, or a large distortions that increases the volume. The threshold was set at 36% of maximum pixel intensity in each image. The result is shown in the lower left images of Figure 3.3. Finally, the centers obtained from the particle location method described in Appendix B, are shown in the lower right image of Figure 3.3.

3.2.3 Nearest neighbors

For the "zoomed-out" {100} data-set, not every feature detected by the method above is a single vacancy. Many vacancies are close to a stacking fault or other defects. Some are also divacancies. Therefore, each detected vacancy was evaluated by close observation of its nearest neighbors, after which 1115 "perfect" single vacancies were retained for further investigation. Furthermore, for a fourth of the sample, the nearest neighbors for each particle and single vacancy were found. If a particle or vacancy had 12 nearest neighbors within 80-120% of the template's lattice spacing, it was considered an FCC particle or a single vacancy. This range was chosen to include, with some margin, the width of the first peak in the pair distribution function shown in Figure 3.4. This procedure identifies about 220 single vacancies and 76000 particles for any given time step in that specific fourth of the sample. Figure 3.5 shows the distribution of particles, evenly dividing the height of the crystal into quarters.

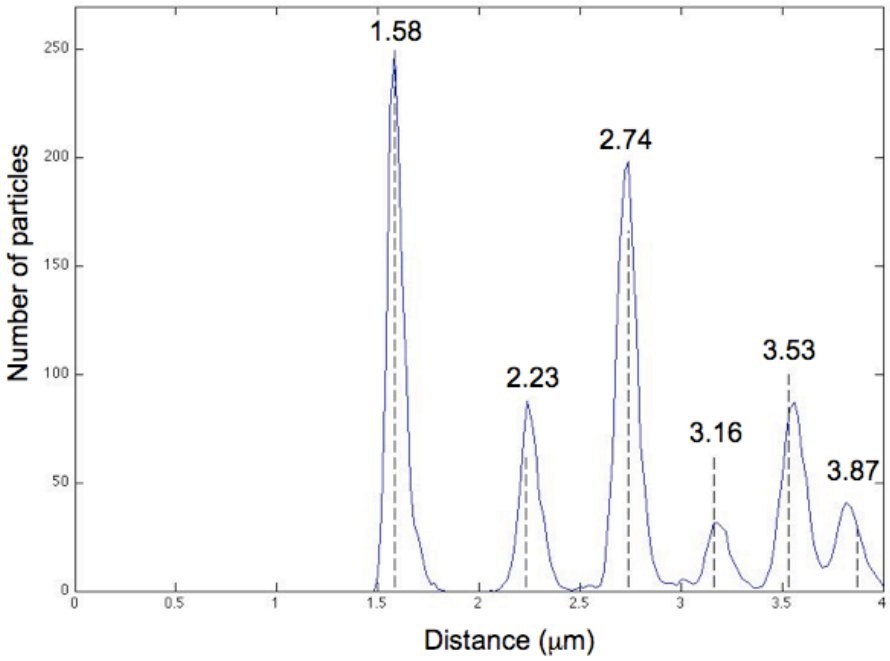

Figure 3.4: Pair distribution of the "zoomed-out" {100} data-set after using the particle locating parameters described in Table 3.2 and the confocal correction in equations 3.24, 3.25, and 3.26. The numbers above the peak indicated the peak location for a perfect FCC crystal with lattice parameter 1.56 μm, distance taken from equation of state. The height of the dashed lines indicated the predicted height based on the height of the first peak.

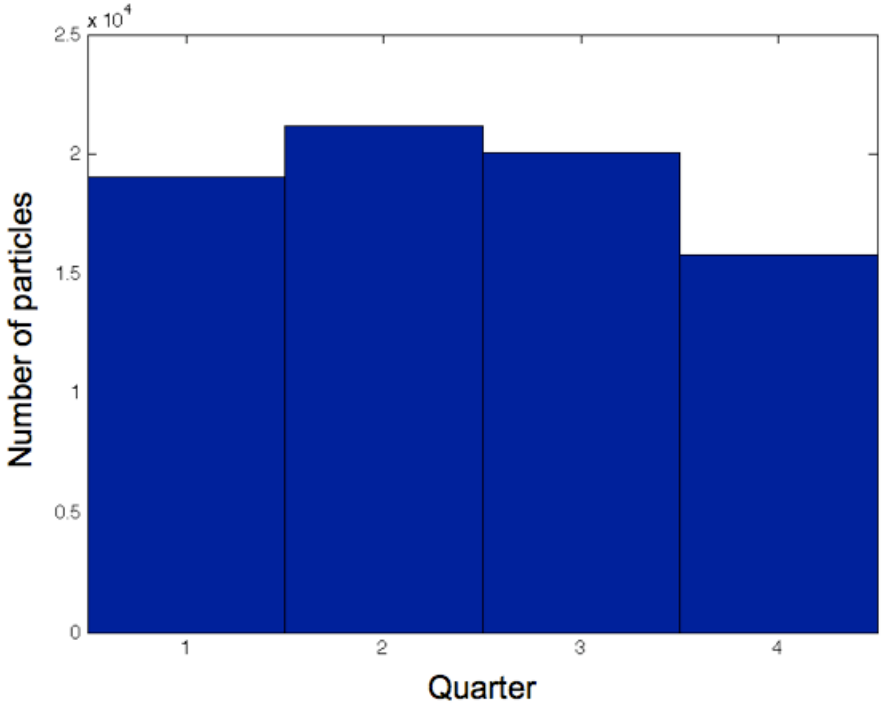

Figure 3.5: Histogram showing the number of particles with 12 nearest neighbors in the four quarters that divide up z evenly for one time step of the "zoomed-out" {100} data-set. Quarter 1 is next to the template.

3.2.4 Voronoi Volume

The Voronoi cell is the part of space closer to the center of a particle than to the center of any other. Its volume is a measure of the local volume per particle. The average Voronoi volume is the average volume per particle. The Voronoi cell for a perfect FCC particle is a rhombic dodecahedron, as shown in Figure 3.6, with 24 edges and 14 vertices.

MATLAB has many functions that can be used to obtain the volume and shape of the Voronoi cell. (1) For large data-sets where only the Voronoi volume of each particle is desired, vorn_vols.m can be used; (2) If both the shape and the volume are desired, voronoin.m and convhulln.m are used to obtain the vertices of the Voronoi cell for each particle as well as the volume contained within those vertices. In order to plot the Voronoi shape VoronoiShape.m was written to determine which vertices belong to which faces and edges. One can also calculate the average particle volume by hand using the raw image by counting the number of particles in a box of measured volume. Figure 3.7 shows how a parallelogram can be fitted on to the "zoomed-in" {111} crystal layers. Each layer has 36 particles enclosed within the drawn area however the top and bottom layers only contain half that amount since the box will cut these layers' particles in half. Therefore, the total number of particles, $N_{particles(111)}$ in the box is $36 \times 3 = 108$. The volume of the box, $V_{Box(111)}$, was calculated by finding the center of the particles at each vertex, calculating the vectors of the sides of the boxes, and taking an average in each direction. The angle between the vectors was also calculated and $V_{Box(111)}$, was found to be 326.5 μm^3. The average

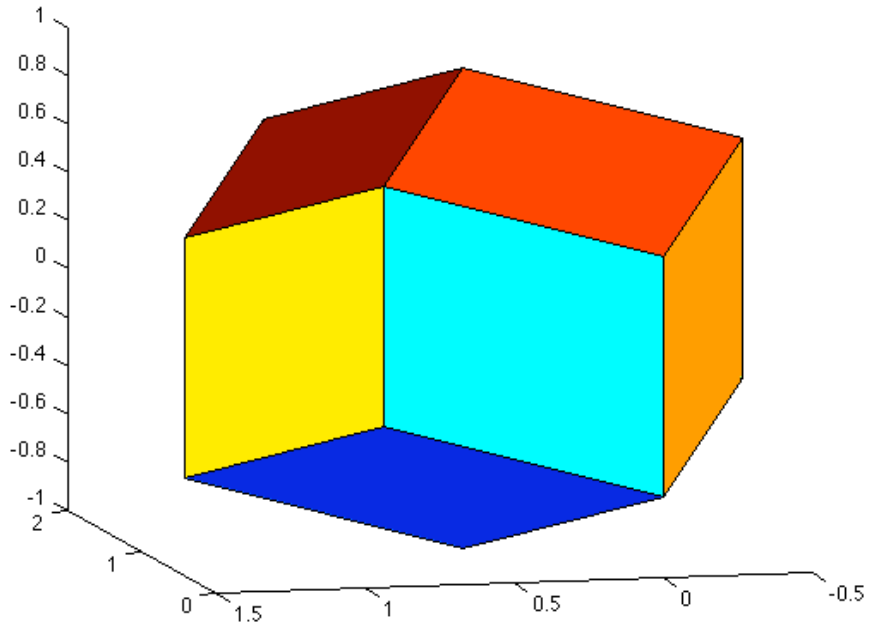

Figure 3.6: Voronoi cell surrounding a particle in an perfect FCC structure. It has 12 faces, 24 edges, and 14 vertices.

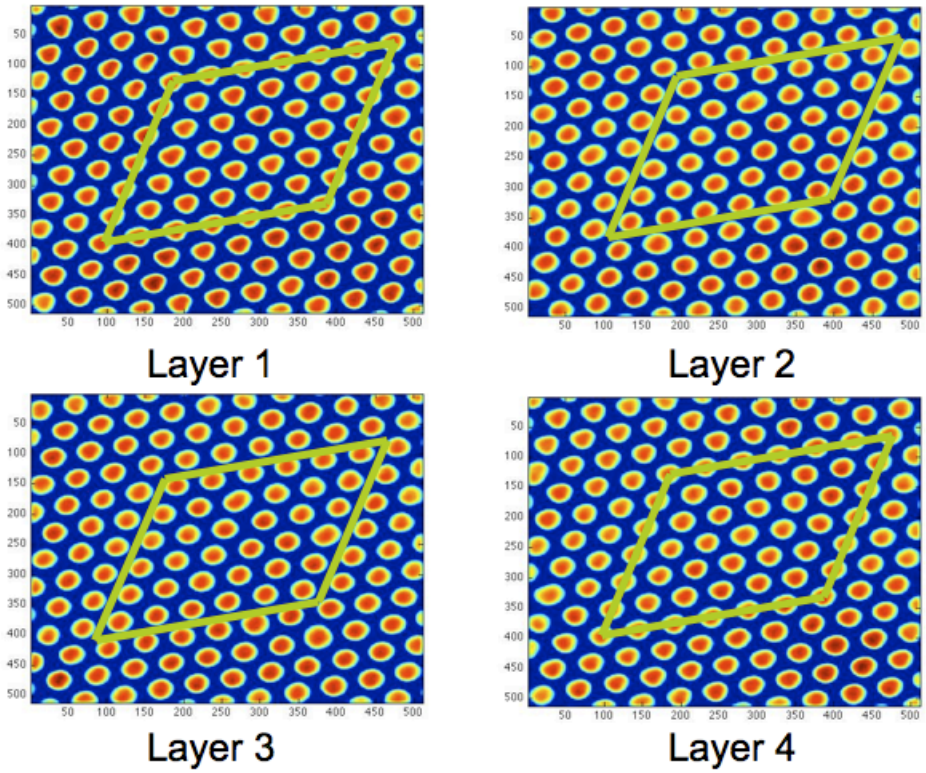

Figure 3.7: A box with known volume drawn onto the four layers in the "zoomed-in" {111} crystal. The number of particles in the box is 108.

particle volume in the "zoomed-in" {111} data-set was therefore 3.02 μm^3.

The same method was used for the "zoomed-out" {100} data-set to obtain a more accurate average particle volume for the whole crystal. Figure 3.8 shows the top and bottom layers of the box. (1st and 48th layer, respectively.) There are more defects in this data and stacking faults had moved through the upper layers of the box. $N_{Particles(100)}$ in each layer is 169 and $V_{Box(100)}$ is 21724 μm^3 so that the average particle volume here is 2.74 μm^3.

The particle volume does vary with height. The same method was used to calculate the particle volume in the first (bottom) 9 layers and the result was slightly larger, 2.85 μm^3. This difference is due to the fact that the set boundary condition in the template affects the first few layers by straining them. Therefore, as more stacking faults are introduced, the crystal relaxes (contracts), and the particle volume decreases in value. (See Chapter 4 for more details on the relationship between stacking faults and the nearest neighbor distance.) When equal amounts of stacking faults are present in the layers, the particle volume increases with height because of the smaller pressure head.

3.3 Results and Discussion

3.3.1 Single Vacancies

3.3.1.1 Concentration of vacancies in our samples

The number of lattice sites per vacancy was calculated by dividing the total volume, in which the 1115 single vacancies are contained by 2.74 μm^3, the average particle volume for the "zoomed-out" {100} data-set. This gives

384640 lattice sites, or $\sim$ 345 lattice sites/vacancy. This is similar to the result of Lee at al. [10] who reported 1-5 vacancies per 1000 particles. If we divide the height of the sample into four quarters (with the same number of particles in each), we observe an uneven distribution of the single vacancies with respect to height, as shown in Figure 3.9. The concentration of vacancies varies only slightly in the lower three quarters, but is significantly smaller in the top quarter. The decrease can be explained by the larger amount of time the particles at the top have had to settle and rearrange without a large pressure head from above. As we shall see, the mobility of the vacancies strongly depends on the local density. It could also be due to a larger number of stacking faults that have travelled through the top volume and allowed the vacancies to climb out when next to their bounding dislocation. (See Section 3.3.1.7 for an example of this.) Not all stacking faults at the top travel down towards the template. Only if the stacking fault's movement relieves misfit strain does the stacking fault travel down into the crystal. The first few layers contain fewer stacking faults because the dislocations stay at an offset distance above the template due to the zero displacement boundary conditions at the template. (See Chapter 4 for a more detailed description of stacking faults, dislocations, and offset.)

3.3.1.2 Nearest neighbors of Vacancies

Using the "zoomed-in" {111} data-set, we find that the nearest-neighbor shell around the vacancy is more compact than the nearest-neighbor shell around the average particle, as shown in Figure 3.10. The average distance between the nearest neighbors in the vacancy cluster is 1.50 μm, while that

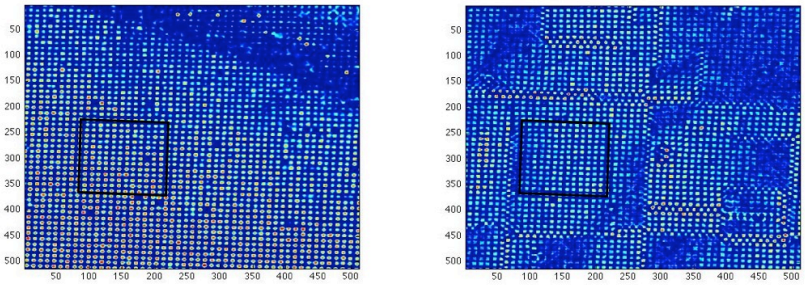

Figure 3.8: Bottom (the first layer of the crystal) and top layers (the 48th layer of the crystal) of the box used to obtain average particle volume in the sample. In between there are 46 layers with colloids not shown.

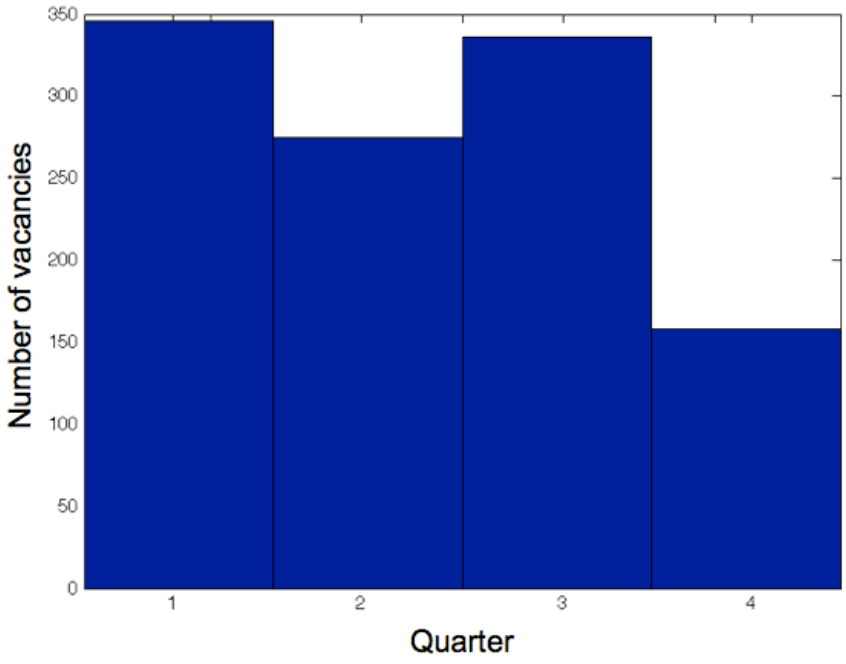

Figure 3.9: Histogram showing the number of vacancies in four quarters that divide up z evenly. Quarter 1 is next to the template.

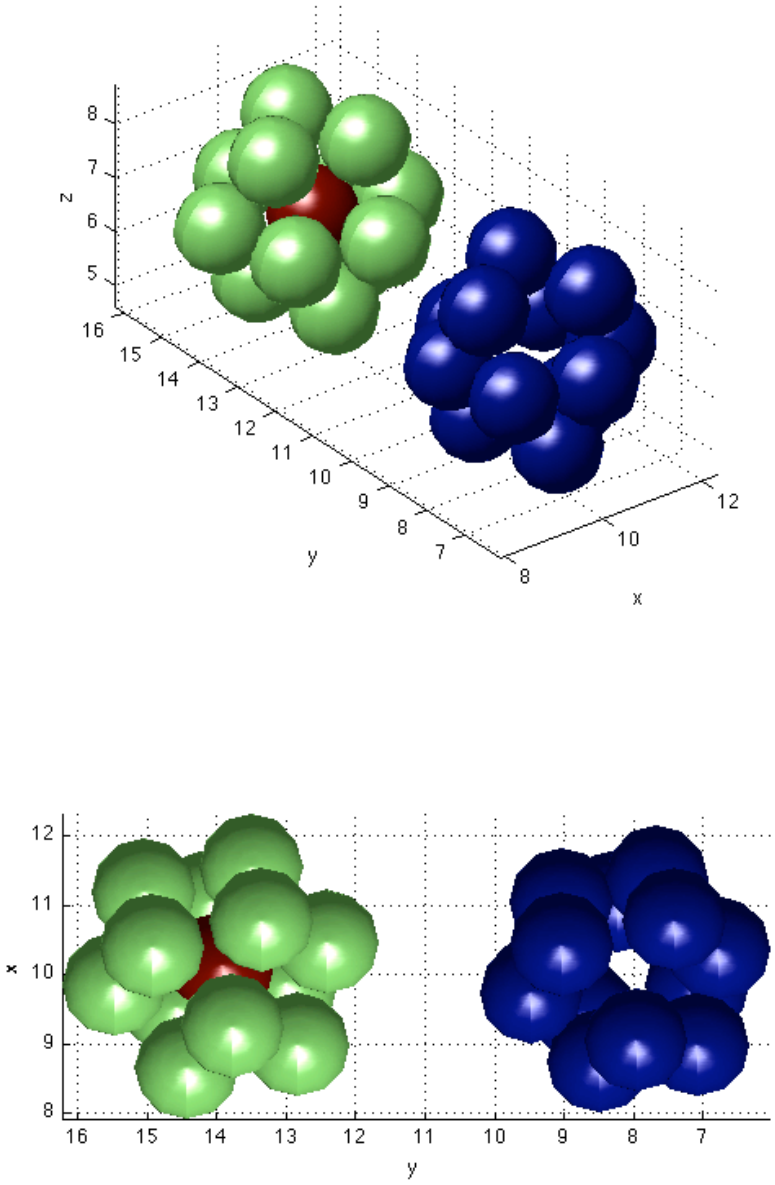

Figure 3.10: Two views of a particle's nearest neighbor shell (green with red center particle in the center) and the vacancy nearest neighbor shell (blue) in the "zoomed-in" {111} data-set. The vacancy shell is noticeably smaller.

same average for the shell around a particle is 1.62 μm, a 7% difference. The average distance of a particle in the second nearest neighbor shell to the center of the shell is 2.26 μm for the vacancy and 2.29 μm for the particle, a 1% difference. This difference can be explained by continuum mechanics [34]. The displacement vector $\bar{u}$ at distance r from a spherical vacancy center takes the form (from spherical symmetry):

$$\bar{u} = \frac{c\bar{r}}{r^3} = -c\nabla\frac{1}{r} \tag{3.27}$$

where c is a constant that measures the defect strength. The volume associated with this displacement is:

$$\Delta V = \int u\dot{d}S = u4\pi r^2 \tag{3.28}$$

So that:

$$u = \frac{\Delta V}{4\pi r^2} \tag{3.29}$$

Therefore, the elastic displacement decreases with increasing distance. For the two shells we measured, this gives:

$$\frac{u_1}{u_2} = \frac{\Delta R_1}{\Delta R_2} = \frac{R_2^2}{R_1^2} \tag{3.30}$$

So that:

$$\Delta R_1 = \frac{2.29^2}{1.62^2}(2.29 - 2.26)\mu m = 0.06\mu m \tag{3.31}$$

The measured ΔR_1 is 0.12 μm, which is much larger, however the "zoomed-in" {111} data-set gives R_1 to be 1.50 μm, which is smaller than the diameter

of the particles, 1.55 μm, simply not possible. (Please see below for an explanation.) If we instead consider 1.55 μm as the minimum nearest neighbor distance then ΔR_1 is 0.07 μm, which is well within our uncertainty. Figure 3.12 shows the horizontal layer cutting through the vacancy, also indicating the relative contraction of the first nearest neighbors.

We can confirm the contraction towards the center of the vacancy visually by plotting the locations of particles in the vacancy layer (green in Figure 3.11) and compare them to locations in a theoretical crystal layer (blue) centered at the vacancy (red). Here it becomes clear that the first nearest neighbors have moved into the open space (as previously noted), but we can also see that the third and fourth nearest neighbors also locating themselves slightly closer to the center of the vacancy.

To investigate further, two cuboctahedra, formed by the centers of the nearest neighbors surrounding a particle and a vacancy were constructed, as shown in Figure 3.13. The volume of the vacancy cuboctahedron is 7.86 μm^3 while that for the particle is 9.24 μm^3. Therefore, the contraction in volume is 15%, which translates to a 5% difference in distance to center.

The obtained nearest neighbor distance of 1.50 μm (as mentioned above) is not the true average of the distance between first nearest neighbors since the average diameter of the particles is 1.55 μm. Instead, when a slow scan is performed for a high-resolution "zoomed-in" image, the image will show a particle center that is the average position of particle during that scan. That average position is different from the actual relative to the

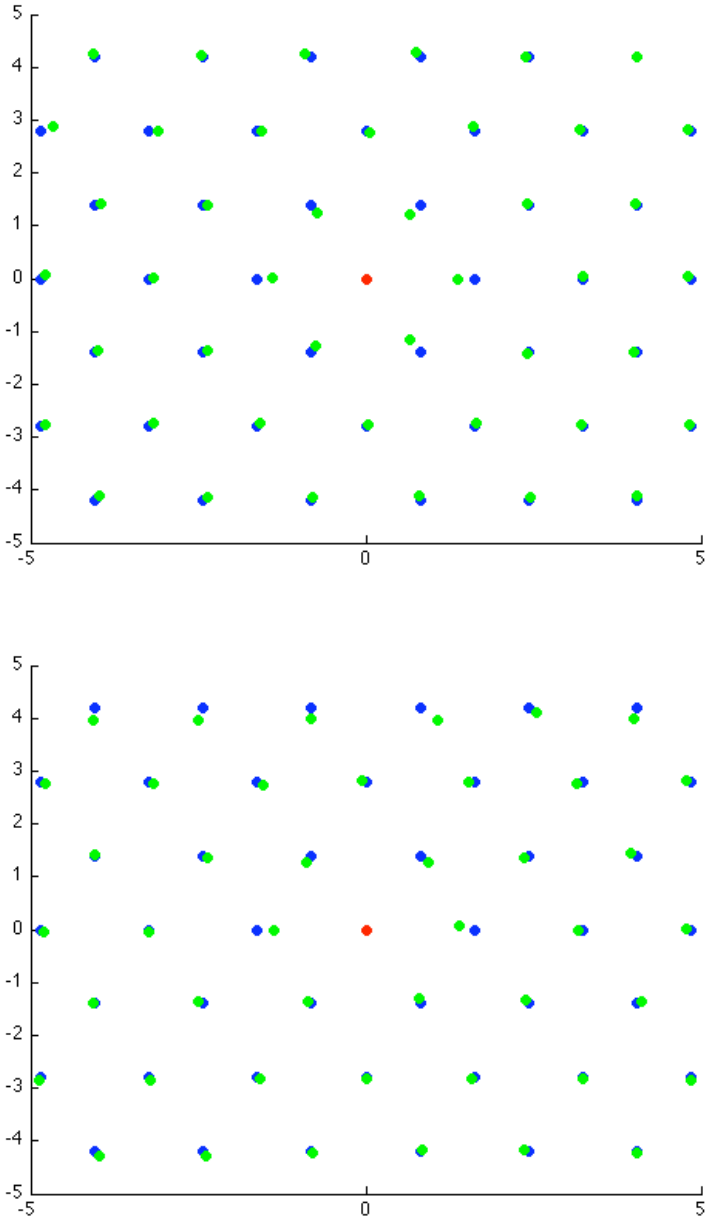

Figure 3.11: The particles (green) in the vacancy layer of the "zoomed-in" {111} data-set together with the locations of particles in a perfect crystal (blue) centered at the vacancy (red). Top picture shows a {111} plane parallel to the template, while the bottom picture depicts one {111} plane that extends through the thickness of the crystal.

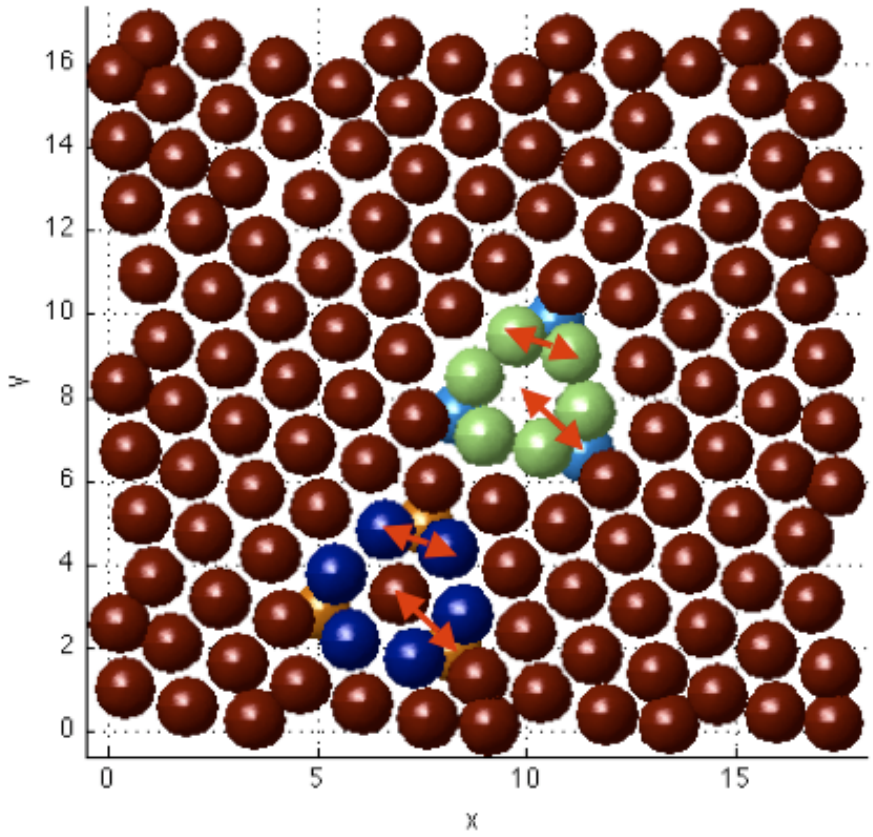

Figure 3.12: Reconstructed image of all particles in the vacancy layer of the "zoomed-in" {111} data-set. The first nearest neighbors are contracted into the vacancy space, giving 1.50 μm spacing between the nearest neighbors, versus 1.62 μm for the nearest neighbors around a particle. The second nearest neighbor distance to the center of the shell is, 2.26 μm for the vacancy and 2.29 μm for a particle.

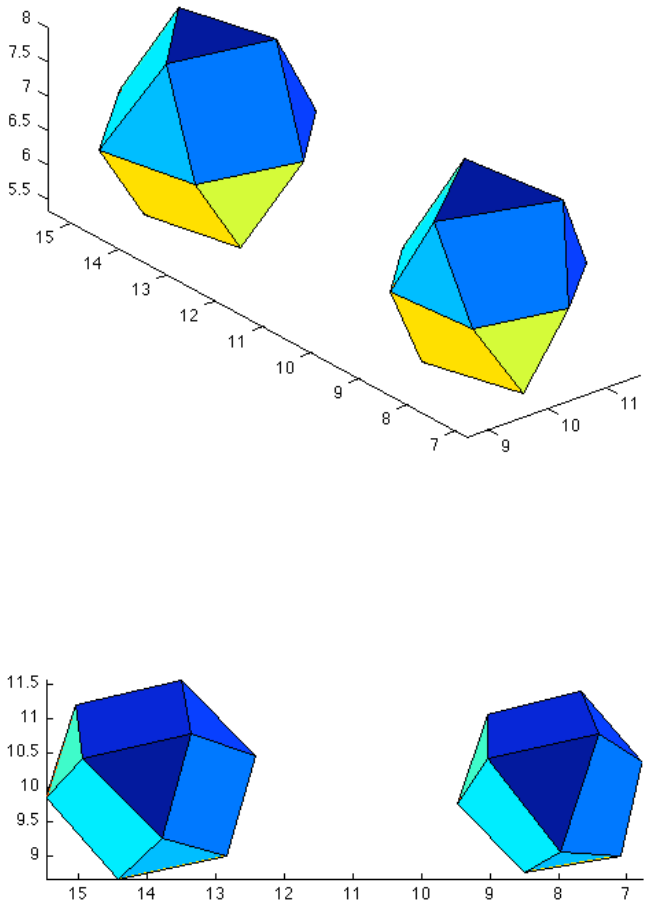

Figure 3.13: The cuboctahedra formed by the centers of the nearest neighbors surrounding a particle (left) and a vacancy (right) in the "zoomed-in" {111} data-set. The volume of the vacancy cuboctahedron is 7.86 μm^3 while the volume of the particle cuboctahedron is 9.24 μm^3.

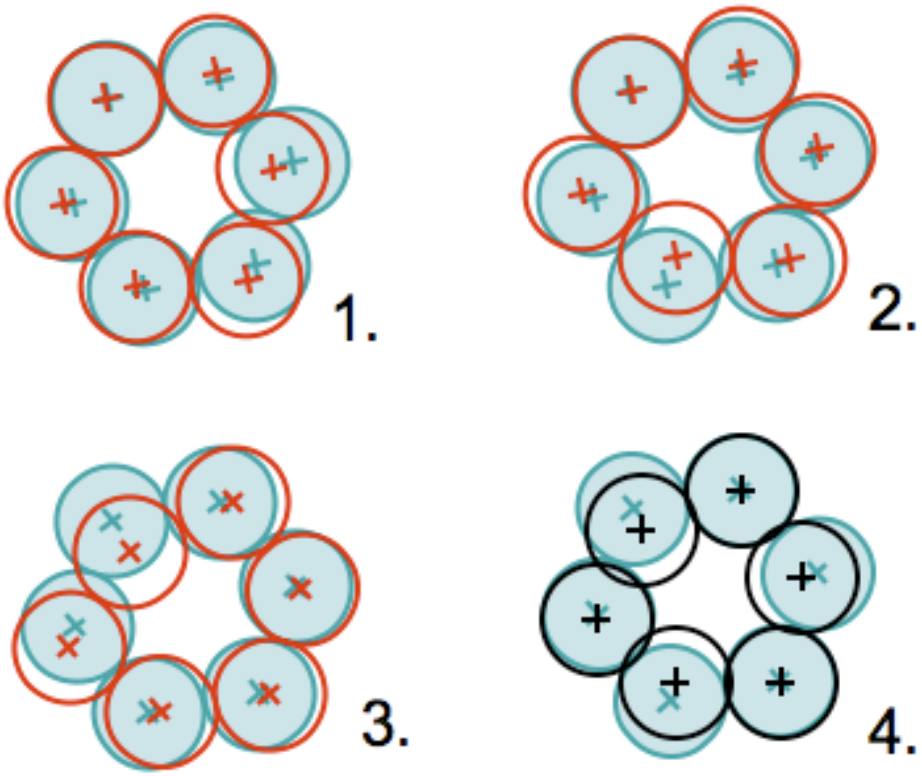

Figure 3.14: Three possible movements of nearest neighbors in a close-packed plane around a vacancy (1-3). The blue particles indicate perfect HCP configuration. The red particles indicates positions (still maintaining hard-sphere distances) when one particle moves in towards the center, pushing its neighbors slightly to the side. The black particles are the average center position for each nearest neighbor when positions from 1-3 are added up.

particle positions at a given moment. A nearest neighbor can find its way into the free space of the vacancy by pushing the other particles slightly sideways, as shown schematically in Figure 3.14. Since the sideways movement of the neighbor particles does not leave these particle much further away from the center than originally, but at the same time, the gain for the particle moving closer to center is large, the average particle position taken over many fluctuating configurations can be closer to the center than for a close-packed shell. This idea explains the larger intensity on the half of the particle facing the vacancy in Figure 3.2.

The statement above is confirmed by observations on the "zoomed-out" {100} data-set. Figure 3.15 shows the nearest neighbor distances for the nearest neighbor shells of all particles (red) and vacancies (blue) for one time step. Here the average of the nearest neighbor distance in the particle shell is 1.59 μm whereas the same average for the vacancies' nearest neighbor shell is 1.58 μm, only a 1% difference. Figure 3.16 shows an initial decrease in nearest neighbor distance from the first to the second quarter. This can be attributed to the layers just above the template being strained due to the offset of the misfit dislocations. The slight increase in the 3rd and 4th layers correlates with the pressure head getting smaller.

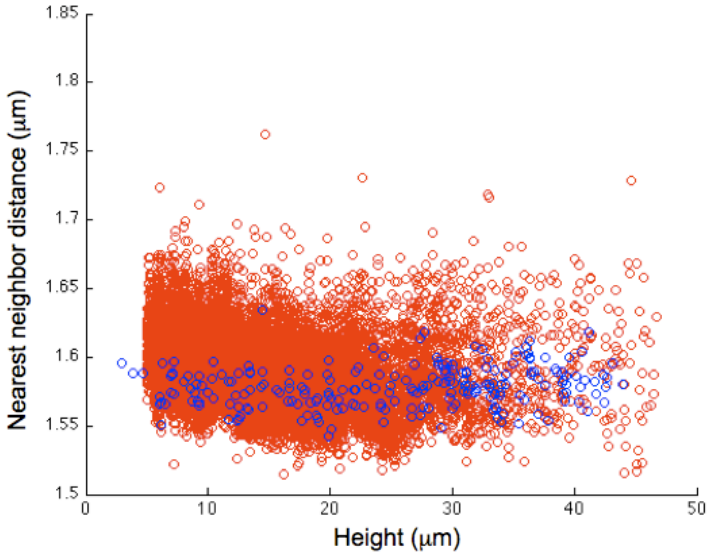

Figure 3.15: The average distance between the particles in the nearest neighbor shell of a particle (red) and the average distance between the particles in the nearest neighbor shell of a vacancy (blue) for one time step plotted as a function of heigh in the crystal in the "zoomed-out" {100} data-set. The average for the particles is 1.59 μm and the average of the vacancies 1.58 μm.

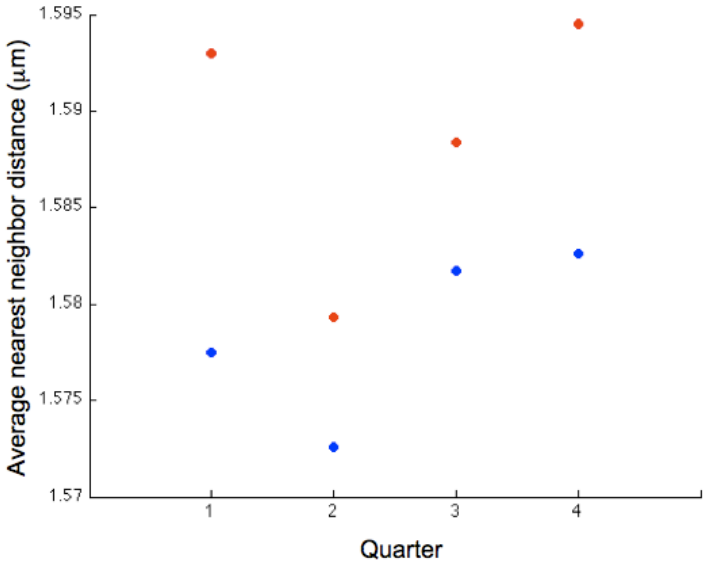

Figure 3.16: The distances of Figure 3.15 averaged per quarter of the crystal; red: particle; blue: vacancy.

3.3.1.3 Voronoi Volume of the bulk Particles

The shape of the Voronoi cells of the actual particles in the crystal is not as perfectly symmetrical as shown in Figure 3.8. The cells might be slightly distorted by nearby line and point defects, or by thermal fluctuations. Therefore, the faces of the Voronoi cells are generally not regular, and sometimes more faces are created. Figure 3.17 shows the Voronoi cell of a particle in the "zoomed-in" {111} data-set.

The particle still has 12 nearest neighbors (as defined by the 80-120% rule of the template spacing), but the number of vertices is now 24 and the number of faces has increased from 12 to 14. This observation applies to 307 particles that have been defined with 12 nearest neighbors in this data set, where the average number of faces is 14. The increase in the number of vertices and faces corresponds to a slight distortion of the cuboctahedral coordination [35]. The two extra faces occur at the vertices where four faces meet. The volume per particle in a perfect FCC crystal with a nearest neighbor distance of 1.62 μm is 3.01 μm^3, which is very close to the average measured Voronoi volume in this crystal, 3.00 μm^3.

Figure 3.18 shows a histogram of the Voronoi volume distribution in the "zoomed-out" {100} data-set. The peak of the histogram occurs at the average particle volume found in Section 3.2.4, 2.74 μm^3. The distribution is not symmetric and has a tail at larger volumes. This tail can be the result of polydispersity. For the polydispersity, a small increase in radius, has a cubic increase in Voronoi volume which, for larger spheres, shows a significant difference in the Voronoi volume distribution.

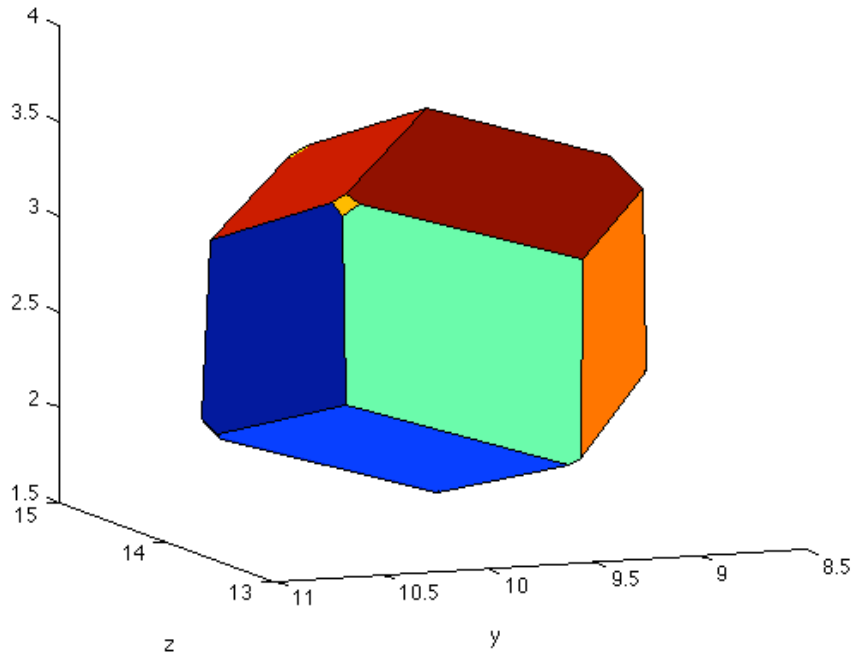

Figure 3.17: Voronoi cell of a particle in FCC structure. This Voronoi cell has 14 faces, compared to a 12 faces for the perfect FCC particle in Figure 3.6

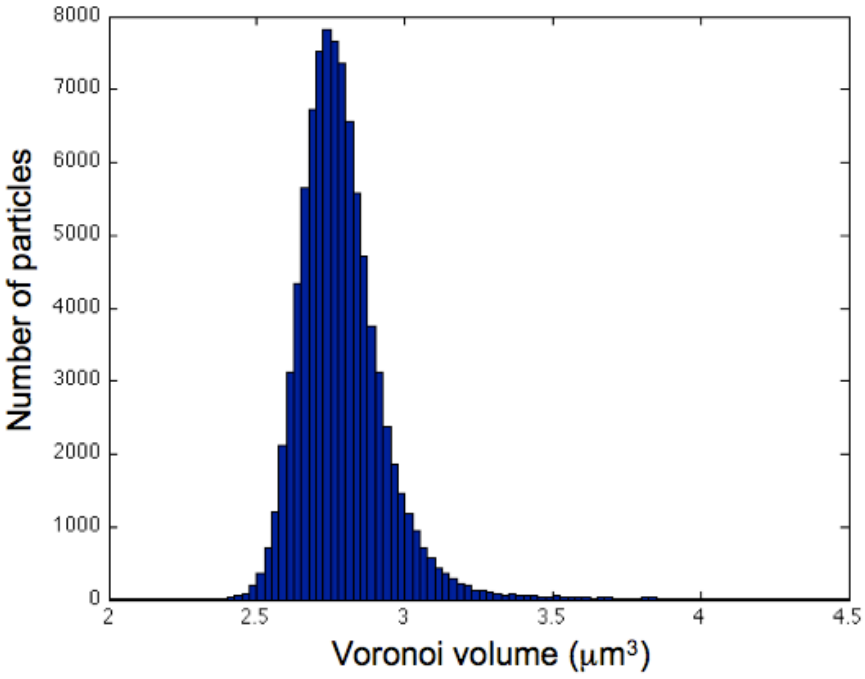

Figure 3.18: Histogram of Voronoi volume of particles in the large {100} data set.

The semi-log plot of Figure 3.19 shows that the top of the right side of the curve looks linear. This can be interpreted by free volume fluctuations which occur with a probability [36]:

$$P(v_f) = \frac{\gamma}{< v_f >} exp \frac{-\gamma v_f}{< v_f >} \tag{3.32}$$

where v_f is the local free volume, $< v_f >$ is the average free volume per particle, and γ is an overlap factor commonly set at 0.5. The slope of the line is -9.62 μm^{-3} and corresponds to $-\gamma/< v_f >$ so that $< v_f > = 0.052$ μm^3. This gives an average particle volume (crystal volume per particle) of:

$$< v_{particle} > = < v_o > + < v_f > = \frac{4}{3}(\frac{1.55}{2})^3 \pi / 0.74 + 0.052 = 2.69 \mu m^3 \tag{3.33}$$

where v_o is the crystal volume per particle for a close-packed crystal. $<v_{particle}>$ is 2% smaller than the value found in Section 3.2.4. Since this value of $< v_f >$ is an upper limit (all other possible contributions to the tail are ignored), the simple free volume theory can not account for the distribution quantitatively.

3.3.1.4 The Voronoi Volume of the Vacancy

The center of the vacancy is defined by the average of the coordinates of its 12 neighbors. The Voronoi cell of the vacancy is shown in Figure 3.20. Figure 3.21 shows Voronoi cells of six of the twelve nearest neighbors when the Voronoi cell from the vacancy center, is removed for the "zoomed-in"

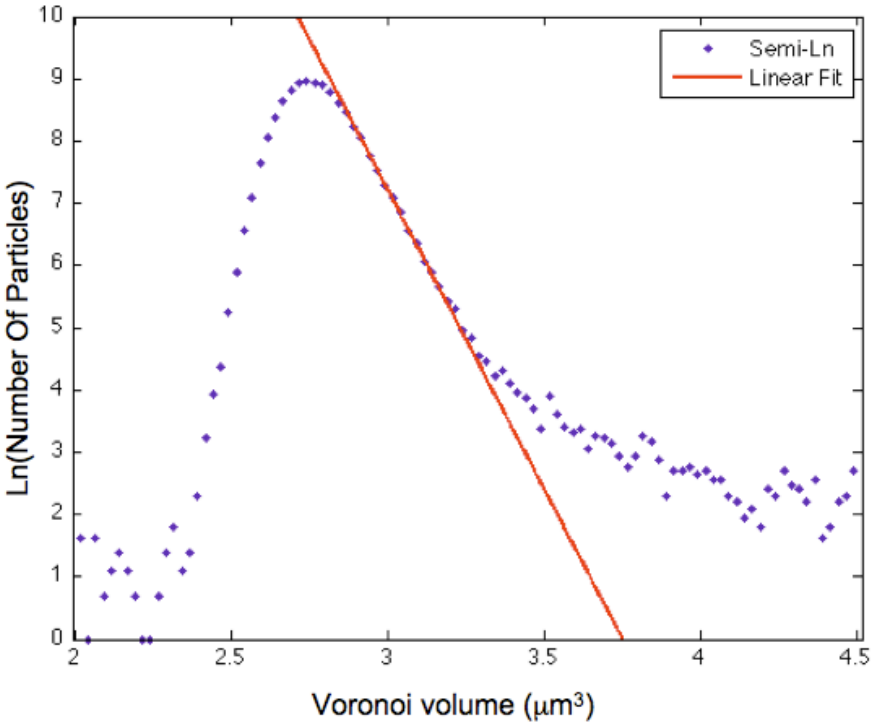

Figure 3.19: Semi-ln histogram of Voronoi volume of particles in the "zoomed-out" {100} data-set.

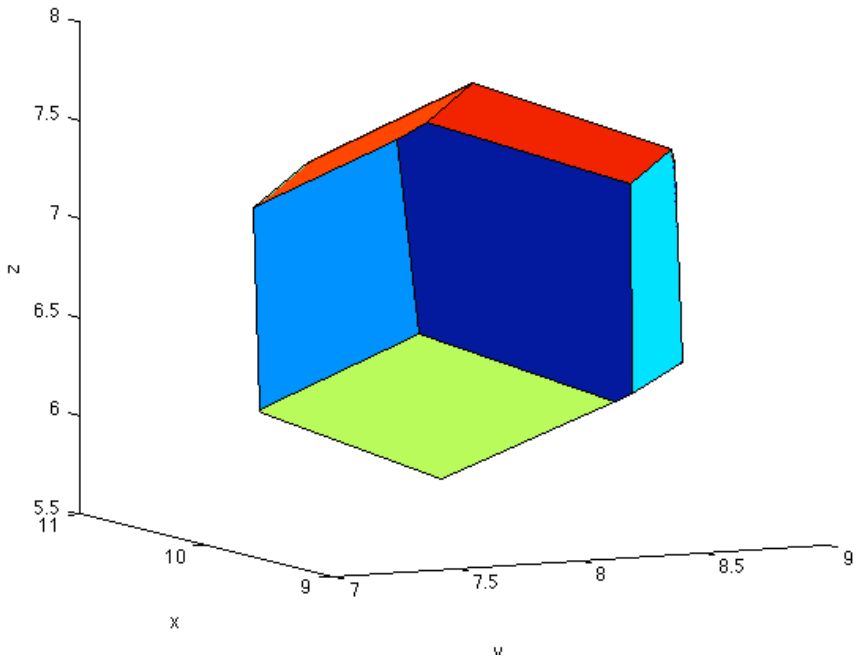

Figure 3.20: Voronoi cell of the vacancy when an artificial data point is put at its center. The Voronoi volume is 2.34 μm^3.

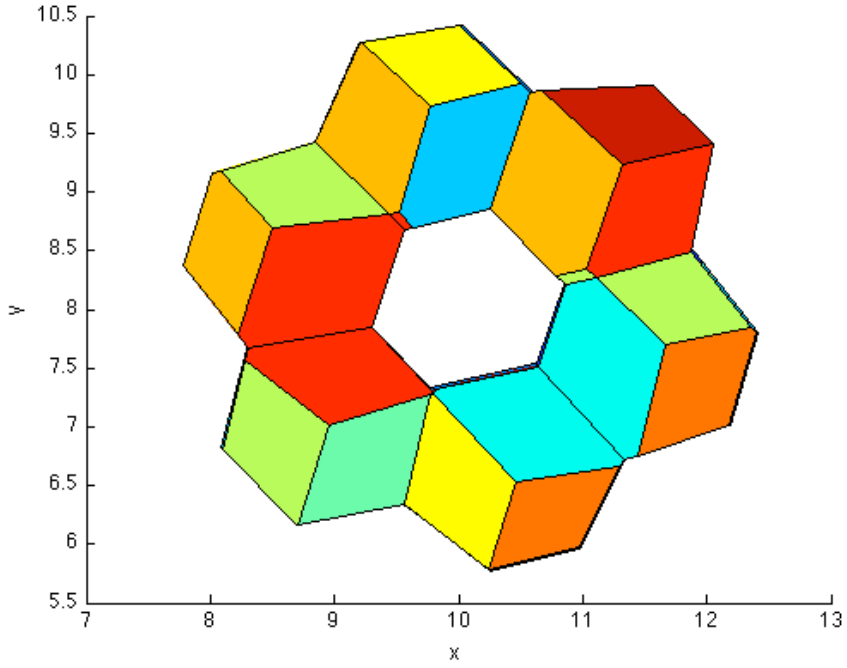

Figure 3.21: Voronoi cells of six nearest neighbors to a vacancy on the same plane, with the Voronoi cell of the vacancy itself removed. The average Voronoi volume here is 2.81 μm^3, 6% smaller than that of an average particle.

{111} data-set. The average Voronoi volume is now 2.81 μm^3, 6% smaller than the average for particles in the defect-free crystal. The Voronoi volume of the vacancy itself is 2.34 μm^3, 22% smaller than that of the average particle in the crystal. This confirms that the 12 particles surrounding a vacancy take up significantly less space than a cluster of 13 particles would in a perfect crystal. In fact, if we try to find the volume of a vacancy by taking the sum of the 12 nearest neigbors' Voronoi volumes and subtracting 12 average particle Voronoi volumes, then the resulting volume is 0.21 μm^3, meaning almost no extra space. It should be kept in mind that the degree of relaxation in this "zoomed-in" {111} data-set is larger than the actual one due to the averaging of the particle positions, as discussed above.

The Voronoi volumes of particles (red) and vacancies (blue) in the "zoomed-out" {100} data-set are shown in Figure 3.22. Here, again, an artificial point is put at the center of the vacancy. The average Voronoi volume of the particles is 2.76 μm^3, but, surprising, the average of the vacancies is slightly larger, 2.78 μm^3. Bennett and Alder [8] point out that at the lower densities the nearest neighbor particles to a vacancy have more room for vibrational entropy and actually expand the lattice. It is surprising, though, that this should hold for the higher densities of our crystals.

Taking out the artificial point in the center of the vacancies, the Voronoi volume of the nearest neighbors of the particles (red) and of the nearest neighbors of the vacancies (blue) is plotted in Figure 3.24 and Figure 3.25 for the "zoomed-out" {100} data-set. The average of the particles nearest neighbors is found to be 2.80 μm^3, while the mean for the vacancies

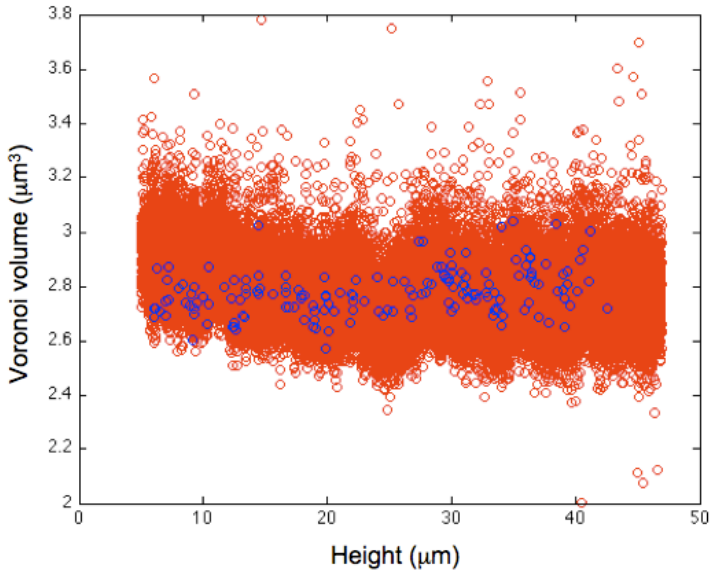

Figure 3.22: The Voronoi volumes of the particles (red) are plotted together with the Voronoi volumes of the vacancies when when an artificial data point is put in the center of the vacancy (blue) for the large "zoomed-out" {100} data-set. The average of the particles is found to be 2.76 μm^3, while the mean for the vacancies is only slightly larger, 2.78 μm^3.

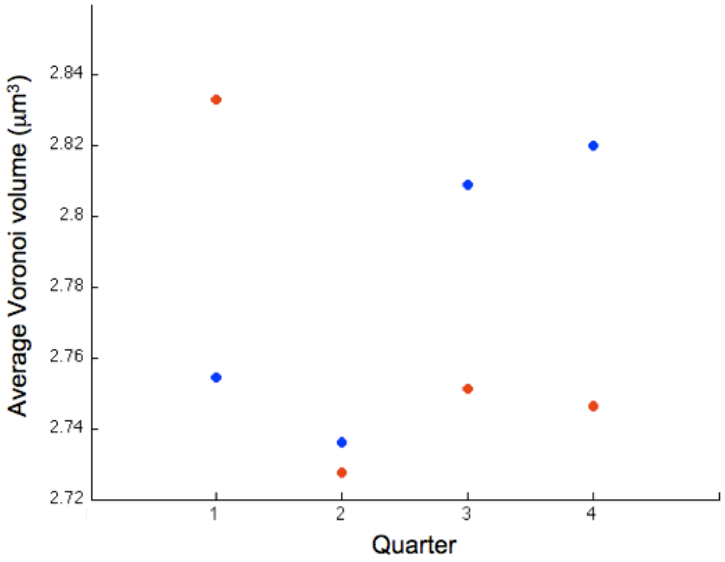

Figure 3.23: The average of Figure 3.22 averaged over the quarters of the crystal height. Particles: red; vacancies: blue.

nearest neighbors is only slightly larger, 2.97 μm^3.

3.3.1.5 Mean Square Displacement Of The Nearest Neighbors Of A Vacancy

For the single vacancies in the "zoomed-out" {100} data-set, the mean square displacements of the nearest neighbors were calculated and compared to those of the neighbors of a particle. The results are shown in Figure 3.26 and Figure 3.27.

Due to the increase in free volume in which they can move, the neighbors of a vacancy have a mean square displacement of, 0.0053 μm^2, which is an order of magnitude larger than the corresponding value for the neighbors of a particle (0.0003 μm^2).

3.3.1.6 Volume of formation of Vacancies

The volume of formation, ΔV_v, of vacancies is the volume change of the crystal upon removing a particle, placing it at the surface, and letting the lattice relax (See Equation 3.34).

$$\Delta V_v = \Delta V_p + \Delta V_{relax} \tag{3.34}$$

In the Sections above several values for these quantities have been calculated for the two data sets. Table 3.4 provides a summary. Equation 3.34 is used to obtain the volume of formation for the "zoomed-out" {100} data-set and plotted versus reduced pressure together with Bennett and Alder's data [8] in Figure 3.28. The reduced pressure $\frac{PV_o}{Nk_BT}$ for our experiment is obtained

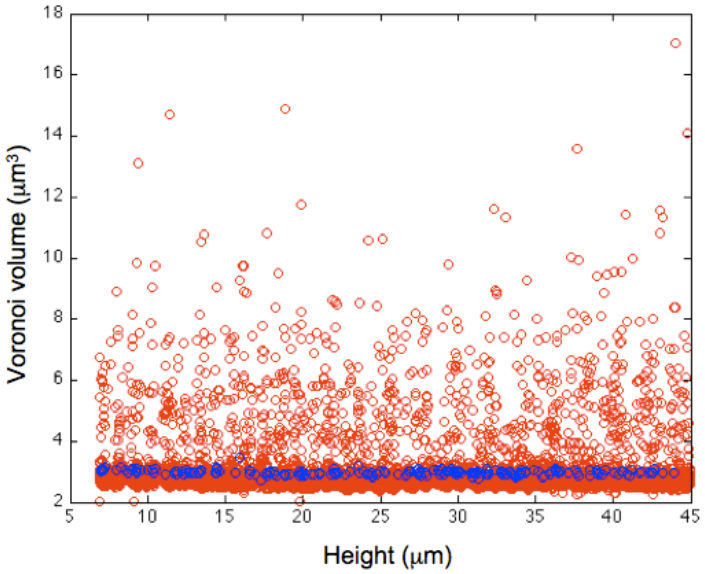

Figure 3.24: The Voronoi volumes of the particles nearest neighbors (red) are plotted together with the Voronoi volumes of the vacancies nearest neighbors (blue) for one time step in the "zoomed-out" {100} data-set. The average of the particles nearest neighbors is found to be 2.80 μm^3, while the mean for the vacancies nearest neighbors is only slightly larger, 2.97 μm^3.

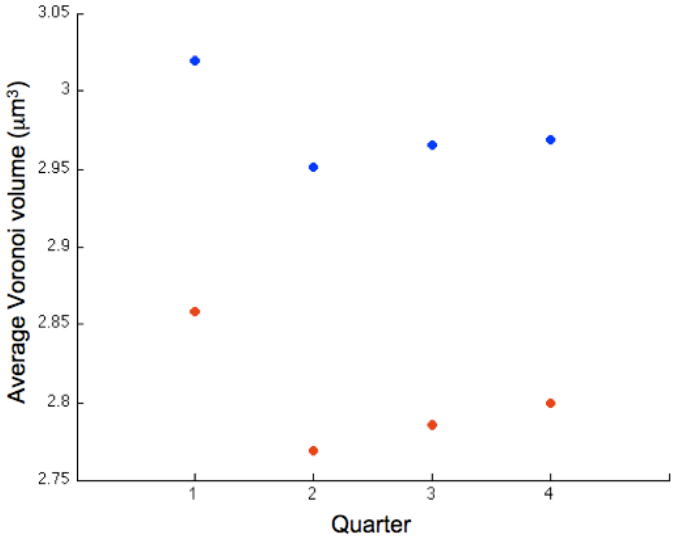

Figure 3.25: The values of Figure 3.24 averaged over the quarters of the crystal height. Particle: red; vacancies: blue.

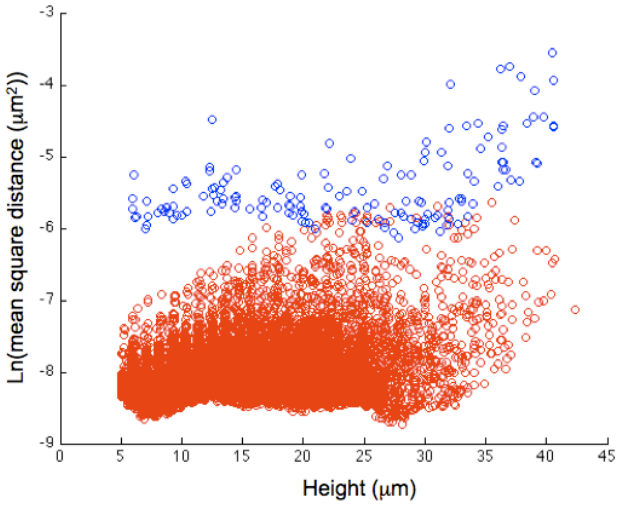

Figure 3.26: The mean square displacement average of the nearest neighbors of particles (red) and vacancies (blue) for the "zoomed-out" {100} data-set as a function of height in the crystal. The average value for the vacancy neighbors is 0.0053 μm^2, and for bulk particles 0.0003 μm^2.

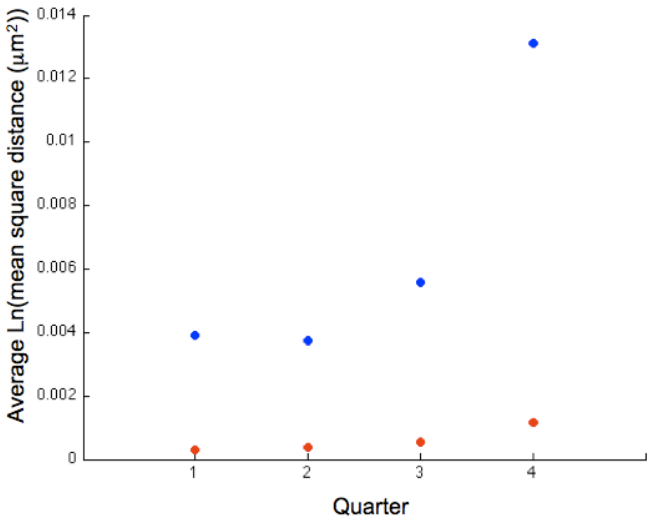

Figure 3.27: The values of Figure 3.26 averaged over the quarters of the crystal height. Particle: red; vacancies: blue.

"Zoomed-in" {111} data set	**Vacancy**	**Particle**	ΔV_{relax}	ΔV_v
Nearest neighbor distance	1.50 μm	1.62 μm	-0.62 μm^3	
Voronoi volume of center	2.34 μm^3	3.00 μm^3	-0.66 μm^3	
Voronoi volume nearest neighb.	3.01 μm^3			
Volume of cuboctahedron	7.86 μm^3	9.24 μm^3	-1.38 μm^3	
Particle Volume		3.02 μm^3		
"Zoomed-out" {100} data set	**Vacancy**	**Particle**	ΔV_{relax}	ΔV_v
Nearest neighbor distance	1.58 μm	1.59 μm	-0.18 μm^3	2.56 μm^3
Voronoi volume of center	2.78 μm^3	2.76 μm^3	0.04 μm^3	2.78 μm^3
Voronoi volume nearest neighb.	2.97 μm^3	2.80 μm^3	0.02 μm^3	2.76 μm^3
Particle Volume		2.74 μm^3		

Table 3.4: Volume relaxation summary of different measurements presented above.

by using the equation of state (Equation 2.8). Since ρ (the number density of particles) $=N/V$, $\frac{p}{k_BT} = \frac{ZN}{V}$ and we get:

$$\frac{PV_o}{Nk_BT} = \frac{ZV_o}{V} \tag{3.35}$$

Our predicted value for the volume of formation over the close-packed volume in Figure 3.28 should be close to 1 because as the density approaches that of close-packed crystals, the volume of formation the close-packed volume should be about the same.

3.3.1.7 Movement of Vacancies

After observing the "zoomed-out" {100} data-set for 13.5 hours, none of the single vacancies had moved. Vacancies close to stacking faults sometimes moved, but these vacancies are not included in our count. Figure 3.29 shows the motion of such a vacancy. These figures are part of a different data-set, in which pictures were taken every minute for 76 minutes. A vacancy, noticeable in the first 7 minutes underneath a layer containing a dislocation line, climbs up to the dislocation in the next time step. The dislocation

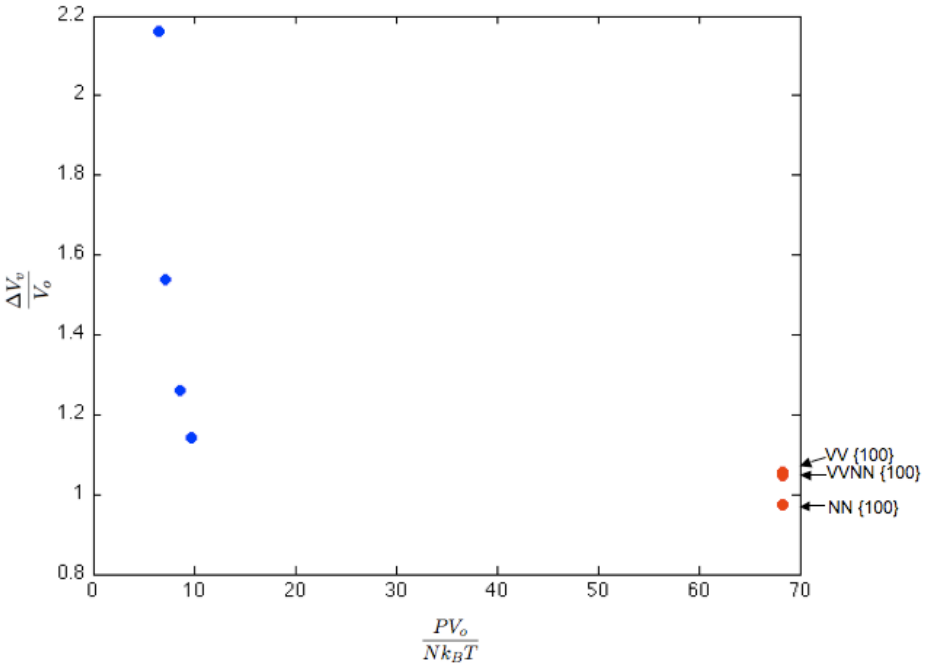

Figure 3.28: Volume of formation over close-packed volume vs. pressure extracted from the different measurements of volume relaxation in Table 3.4. Blue indicated Bennett and Alders data and red indicated our data. VV indicated the volume of formation obtained by creating an artificial point in the center of the vacancy to obtain the Voronoi volume of the vacancy, NN indicates the volume of formation obtained from the nearest neighbor distance around a vacancy, and VVNN stands for Voronoi volume of nearest neighbors, where each nearest neighbor obtains one 12th of the space of the vacancy. The volume of formation is calculated by adding the 12 nearest neighbor Voronoi volumes and subtracting 12 particle Voronoi volumes. See values in Table 3.4.

line had in the same time period moved towards the vacancy and the jog straightens out as a result of the climb, as shown in Figure 3.30. This phenomenon illustrates our earlier explanation why layers with dense line defects contain fewer vacancies.

Since no single vacancies are moving on their own, it is impossible to get an accurate jump frequency. However, an upper limit can be obtained by assuming that one vacancy would have moved in the next time step, meaning after 14 hours. This corresponds to a jump frequency of:

$$\Gamma = \frac{1}{1115} \times \frac{1}{14 \times 3600} = 1.8 \times 10^{-8} sec^{-1} \tag{3.36}$$

Using the attempt frequency, $\nu = 0.6$ sec^{-1} (Equation 3.12), we obtain $\frac{\Delta G_m}{k_B T} = 17.5$ from Equation 3.9. We compare that value with Bennett and Alder's simulations [8] taken on hard sphere systems of much lower density in Figure 3.31. Here, the jump frequency over attempt frequency ($\frac{\Gamma}{\nu}$) vs $\frac{PV_o}{Nk_BT}$ for both Bennett and Alder's data (blue) and ours (red) is plotted. $\frac{PV_o}{Nk_BT}$ can be obtained for our crystal from the equation of state [24] and the particle volume [17], as described in Equation 3.35

The best fit straight line through Bennett and Alder's data (blue) is shown in Figure 3.31. For $\frac{PV_o}{Nk_BT}$ of our data, their extrapolated value for -log($\frac{\Gamma}{\nu}$) is 73.2. In other words, we would need to wait 10^{21} years in order for a jump to occur.

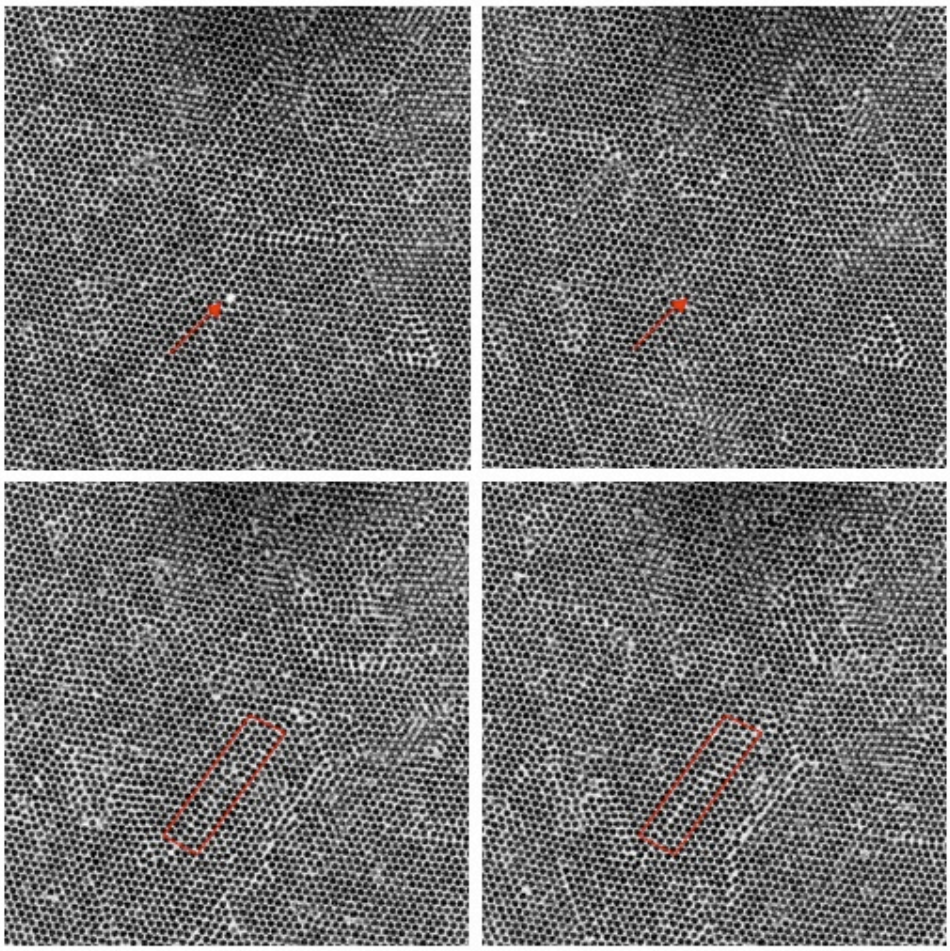

Figure 3.29: A vacancy has been at the same spot of 7 minutes, top left picture. In the layer above a dislocation line with a jog moves over the vacancy, bottom left picture. After 8 min, the vacancy has climbed to the dislocation line (top and bottom right picture respectively). The jog disappeared in the next time step as shown in see Figure 3.30

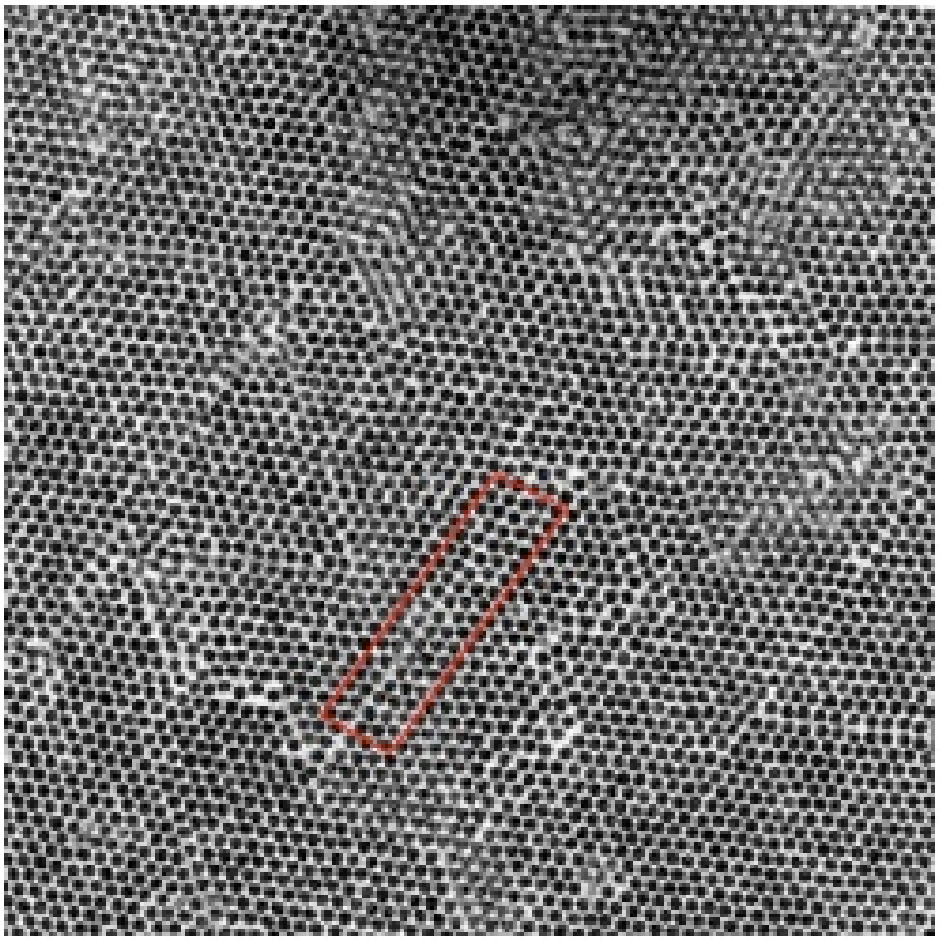

Figure 3.30: One minute later, the jog that was previously present in the dislocation line before the vacancy climb (Figure 3.29) has disappeared.

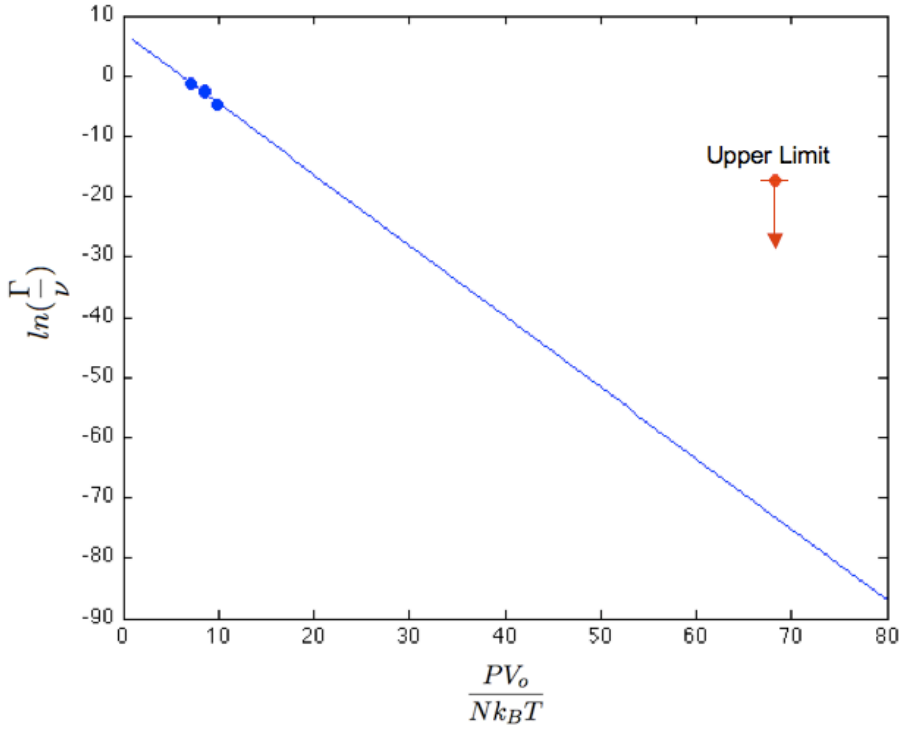

Figure 3.31: Jump frequency over attempt frequency vs reduced pressure for Bennett and Alder's vacancy data (blue) and the upper limit (red) for the "zoomed-out" {100} data-set. The line is a linear fit through Bennett and Alder's data.

3.3.2 Divacancies

3.3.2.1 Concentration of divacancies in our samples

The number of divacancies in the "zoomed-out" {100} data-set is 18. They are distributed unevenly throughout the sample, as depicted in Figure 3.32. There are more divacancies in the top half of the sample, indicating that divacancies might be more likely to form at lower density, where vacancies may briefly have higher mobility and hence a greater chance at associating.

3.3.2.2 Voronoi Volume of divacancies

Figure 3.33 shows the Voronoi volumes around the divacancies, plotted by a color code for each particle on a scale between 2.3 and 3.3 μm^3. This Figure clearly shows that some Voronoi volumes around the divacancies are slightly larger, which might explain the higher likelihood of movement compared to single vacancies. We calculated the average Voronoi volume of the center of the divacancies vs time (as shown in Figure 3.34). The centers of the two vacancies, $\bar{r}_{v1}$ and $\bar{r}_{v2}$, were determined for each time step by solving these simultaneous equations:

$$\frac{1}{12}(\sum_{i=1}^{11} \bar{r}_i + \bar{r}_{v2}) = \bar{r}_{v1} \tag{3.37}$$

$$\frac{1}{12}(\sum_{j=1}^{11} \bar{r}_j + \bar{r}_{v1}) = \bar{r}_{v2} \tag{3.38}$$

where the $\bar{r}_i$ and the $\bar{r}_j$ are positions of neighbors of each vacancy. The mean Voronoi volume over time is 5.59 μm^3, giving 2.80 μm^3 per vacancy, which

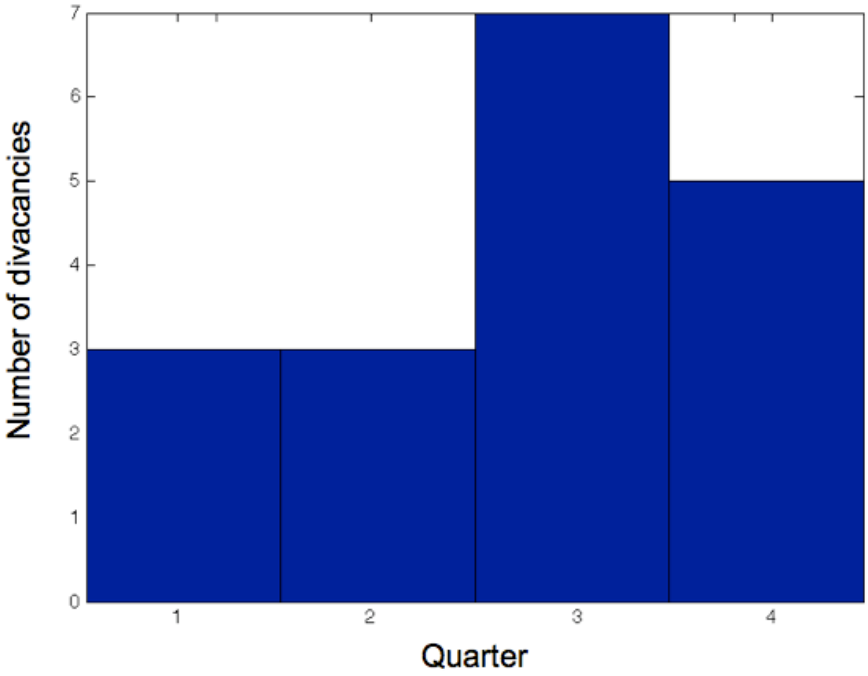

Figure 3.32: Distribution of divacancies in the four quarters of the height. Quarter 1 is closest to the template.

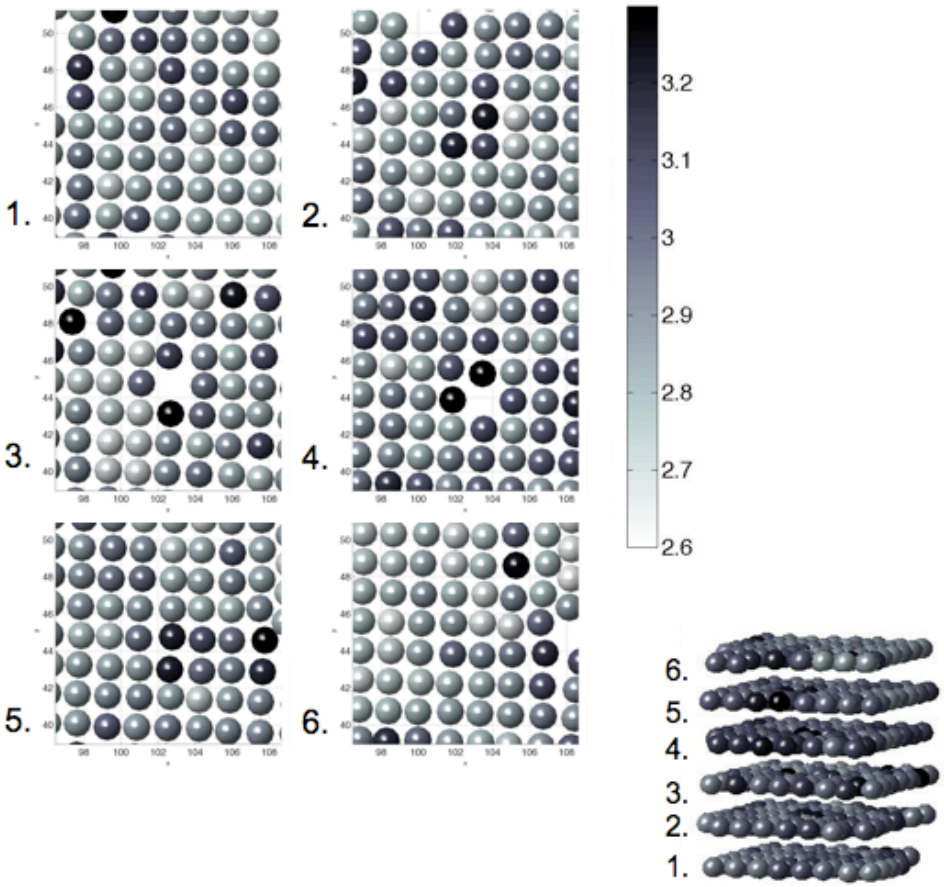

Figure 3.33: Voronoi volumes of particles in layers around the divacancy.

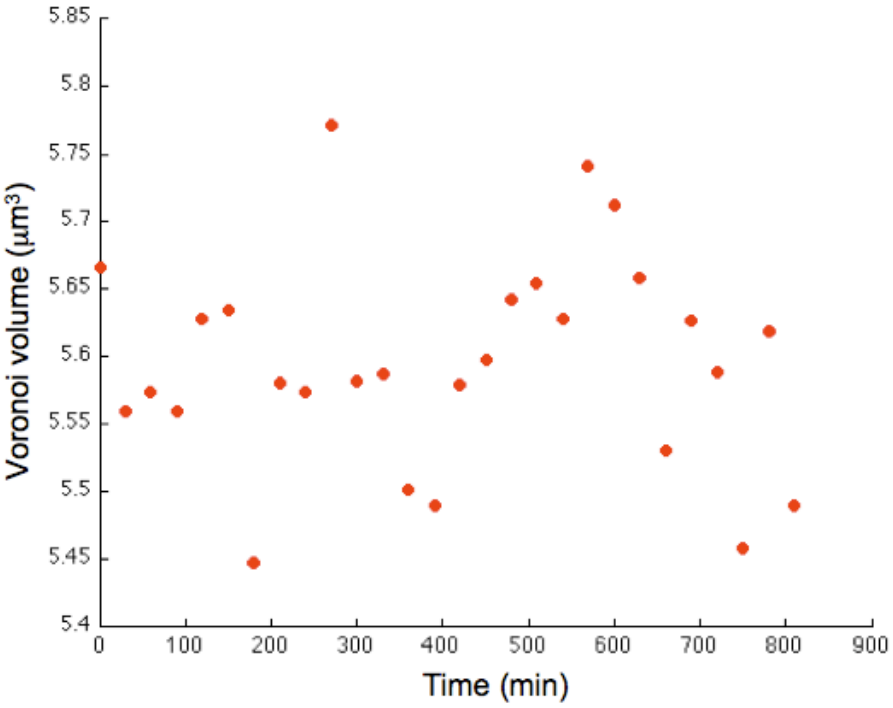

Figure 3.34: Voronoi volume of a divacancy vs. time.

is larger than that of the single vacancy (2.34 μm^3, Figure 3.20). Since the Voronoi volume of a divacancy is greater than twice the Voronoi volume of a vacancy, the contribution of the volume of association, ΔV_a, to the enthalpy of formation of the divacancy, ΔH_a, is positive, the increase in the entropy of vibration upon association, ΔS_a, must be sufficiently large to result in a negative free energy of association $\Delta G_a = \Delta H_a - T\Delta S_a$. The calculations of Bennett and Alder indicate that ΔG_a is indeed negative. The Voronoi cells for three different time steps are shown in Figure 3.35. The average Voronoi volume for the 18 nearest neighbors around the divacancy over time is shown in Figure 3.36. The overall average Voronoi volume is 3.13 μm^3 per nearest neighbor. This divacancy is in the third quarter, which according to Figure 3.23 gives a particle Voronoi volume of 2.75 μm^3, the ΔV_v for the divacancy can be calculated:

$$\Delta V_v = 18 \times (3.13 - 2.75)\mu m^3 = 6.84\mu m^3 \tag{3.39}$$

This gives 3.42 μm^3 per vacancy, which is much larger than that of a single vacancy. ΔV_v gives a V_{relax}= 0.98 μm^3 according to Equation 3.34, which is also significantly larger than that of a single vacancy.

3.3.2.3 Motion of divacancies

Out of the 18 divacancies, only three moved. The three divacancies make a total of four jumps over 13.5 hours, giving a jump frequency of:

$$\Gamma = \frac{4}{18} \times \frac{1}{13.5 \times 3600} = 4.6 \times 10^{-6} sec^{-1} \tag{3.40}$$

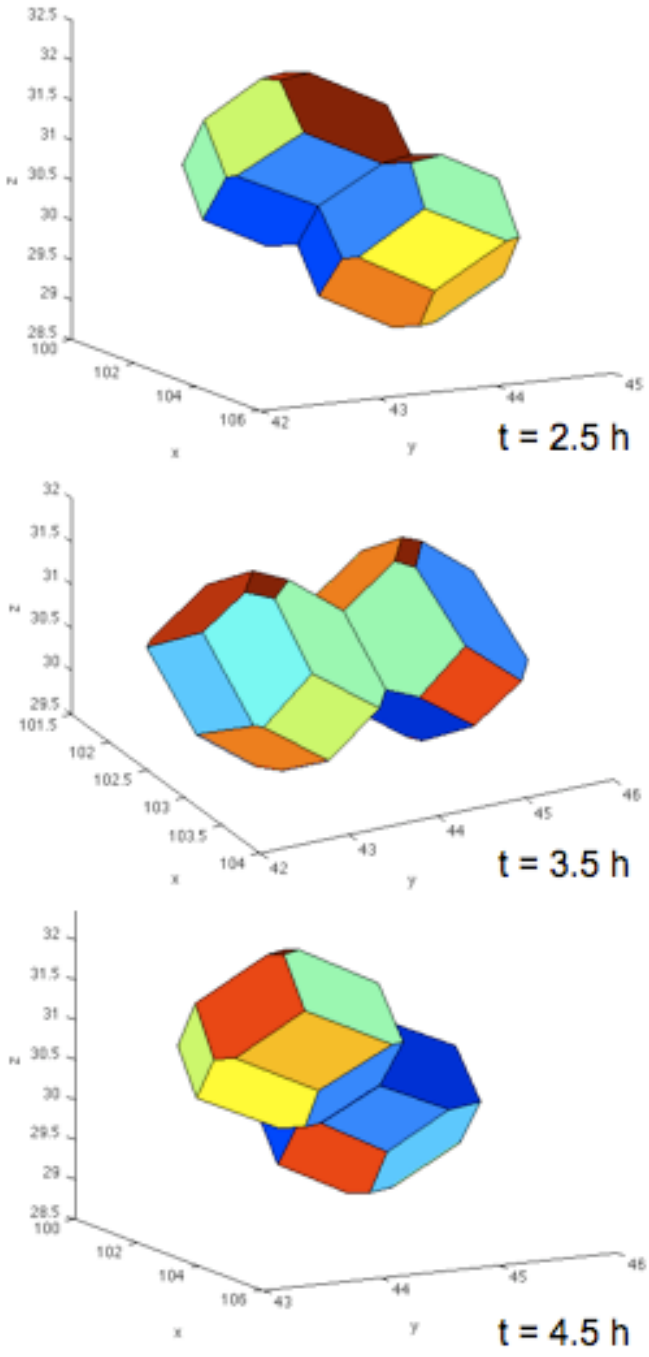

Figure 3.35: The divacancy's voronoi cell.

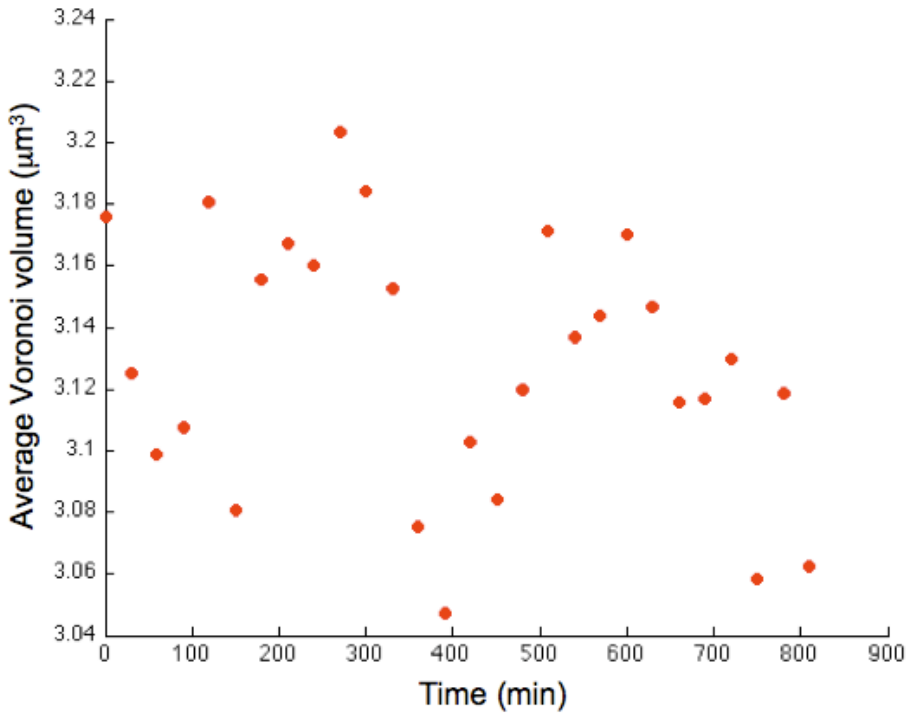

Figure 3.36: Average Voronoi volume for the nearest neighbors of the divacancy vs. time.

The error is $\sqrt{4}$, giving a jump frequency error of $\pm 2.3 \times 10^{-6}$. With the attempt frequency $\nu = 0.6$ sec^{-1} the free energy of motion of the divacancy is obtained from Equation 3.9 to give $\frac{\Delta G_m}{k_B T} = 11.8$, with an error of ± 0.7. The one divacancy that moved twice is featured in Figure 3.37. The first jump happened between 2.5 and 3 hours after the experiment started and the second movement happened between 4 and 4.5 hours.

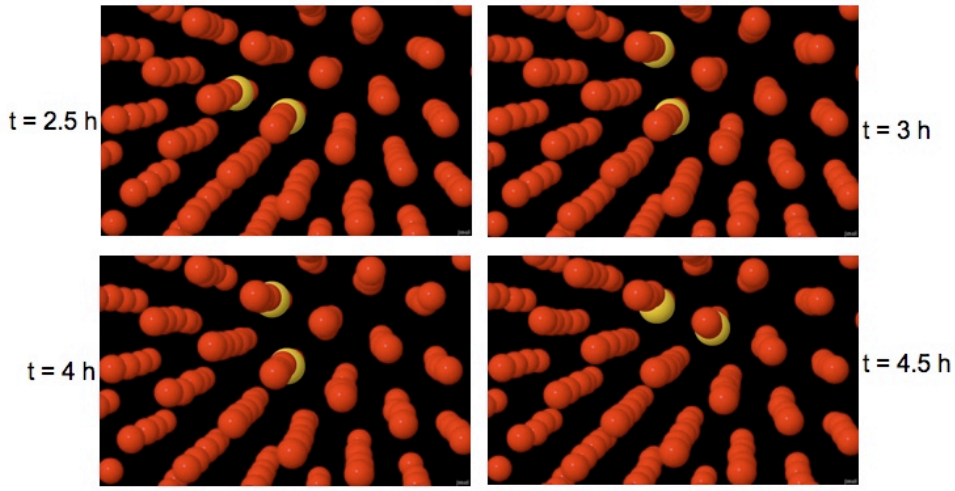

Figure 3.37: The only divacancy to move twice during the 13.5 hours is indicated above with two yellow particles situated at the divacancy's two centers. The first jump occurred after 3 hours. The second jump occurred 4.5 hours into the experiment.

The time of movement of the divacancy vs their height is shown in Figure 3.39. Three out of the four movements happened at the top of the crystal, presumably because of the lower density.

The jump frequency over attempt frequency vs reduced pressure is plotted for Bennett and Alders's data (blue) and our crystal (red) in Figure 3.39. Our data are close to the extrapolation of the simulation data. Considering Equation 3.9, we now have:

$$\log \frac{\Gamma}{\nu} = -\frac{p\Delta V_m}{k_B T} + \frac{\Delta S_m}{k_B} \tag{3.41}$$

We can multiply top and bottom of the first term with V_o:

$$\log \frac{\Gamma}{\nu} = -\frac{pV_0}{k_B T}\frac{\Delta V_m}{V_0} + \frac{\Delta S_m}{k_B} \tag{3.42}$$

The slope of a line through both our and Bennett and Alder's is $\frac{\Delta V_m}{V_0} = 0.18$. The intercept of the line with the frequency axis is $\frac{\Delta S_m}{k_B} = 0.49$. Both these values are plausible.

3.3.3 Vacancy - Interstitial Pairs

3.3.3.1 Concentration

There are five vacancy - interstitial pairs in the "zoomed-out"{100} data-set, in which a vacancy is adjacent to an interstitial. Four of these interstitials are located in the second quarter and one in the third quarter (Figure 3.40) of the sample. There are no intersitials in the upper quarter. The higher mobility in the top layer might limit the chance for them to be trapped as defects.

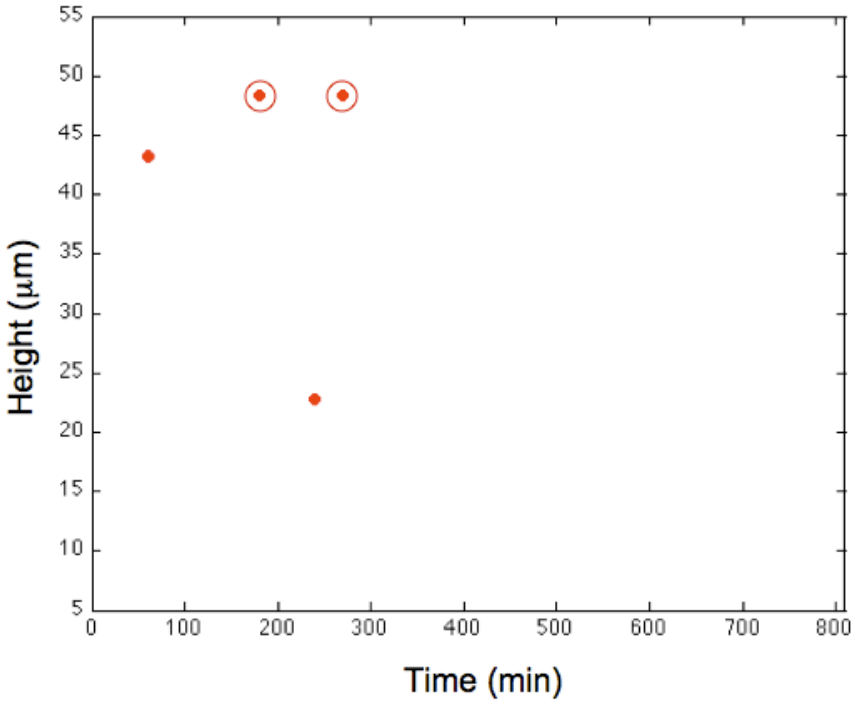

Figure 3.38: Time of the movement of the divacancies as a function of their height. The circled dots indicate the same divacancy.

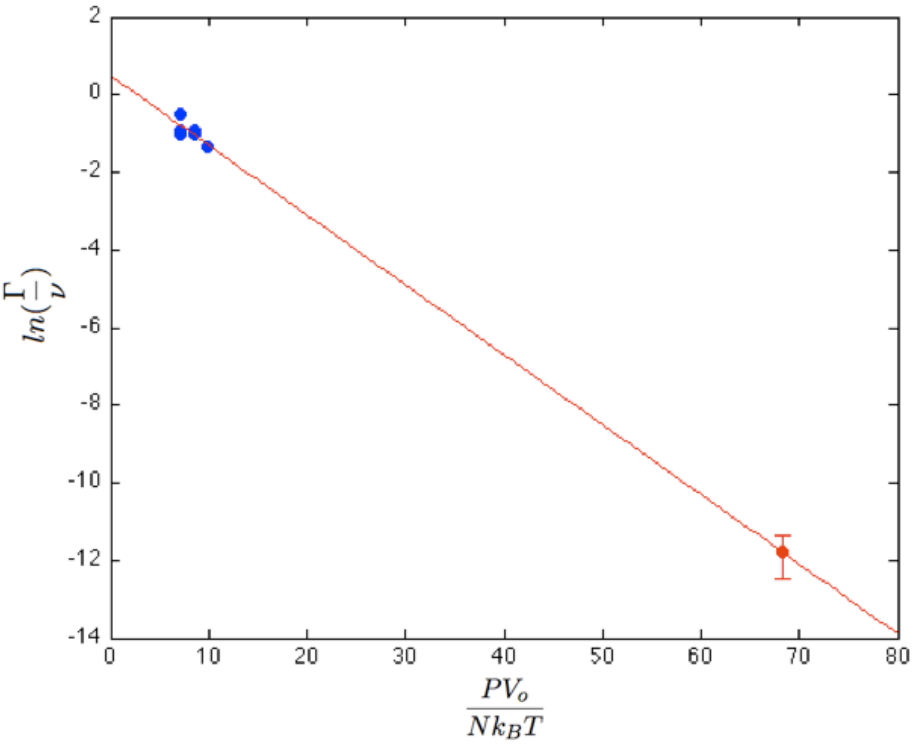

Figure 3.39: Jump frequency of the divacancy over attempt frequency vs reduced pressure for Bennett and Alder's data (blue) and our crystal (red). The line is a fit to Bennett and Alder's data.

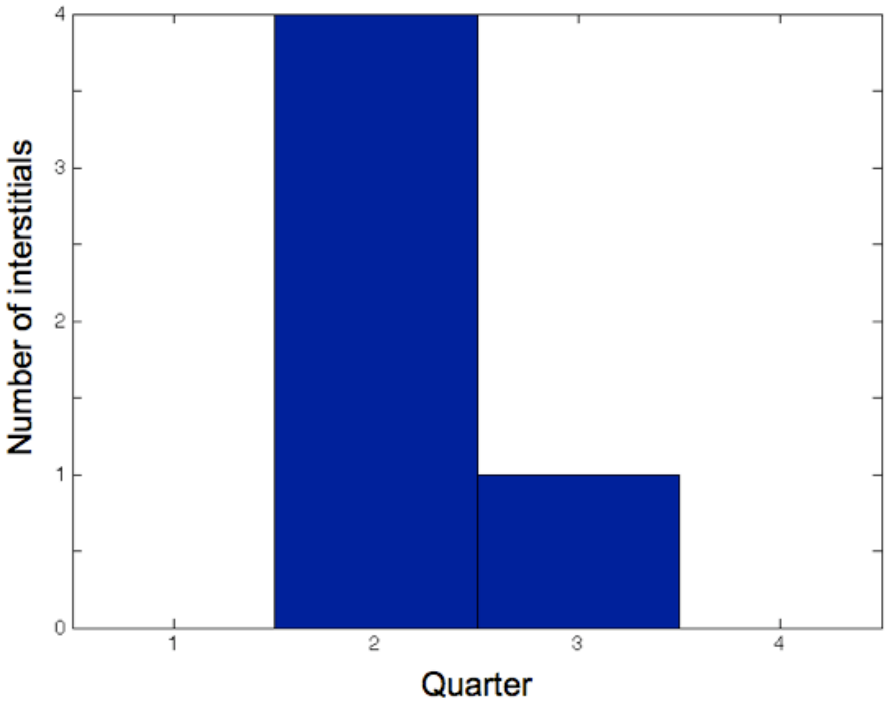

Figure 3.40: Distribution of interstitial - vacancy pairs across four quarters of the height.

3.3.3.2 Motion of the Interstitial into the Vacancy (Annihilation).

An example of an interstitial that moves into the vacant space is shown in Figure **??**. Three out of five move into the vacant lattice site during the duration of the observation, 13.5 hours, which gives a jump frequency of:

$$\Gamma = \frac{3}{5} \times \frac{1}{13.5 \times 3600} = 1.2 \times 10^{-5} sec^{-1} \tag{3.43}$$

The error is $\sqrt{4}$, giving a jump frequency error of $\pm 0.7 \times 10^{-5}$. With the attempt frequency $\nu = 0.6$ sec^{-1} this give from Equation 3.9, $\frac{\Delta G_m}{k_B T} = 10.8$, with an error of ± 0.8. A summary of the vacancy, divacancy, and interstitial-vacany pair's jump frequency and Gibbs free energy is displayed in Table 3.5.

	Jump frequency, Γ (sec^{-1})	**Gibbs free energy of motion, $\frac{\Delta G_m}{k_B T}$**	**$\frac{\Delta G_m}{k_B T}$ extrapolated from simulation**
Vacancy	1.8×10^{-8} (upper limit)	17.5 (lower limit)	73.2
Divacancy	$(4.6 \pm 2.3) \times 10^{-6}$	11.8 ± 0.7	12.3
Vacancy - interstitial pair	$(1.2 \pm 0.7) \times 10^{-5}$	10.8 ± 0.8	

Table 3.5: Jump frequency and Gibbs free energy for the vacancy, the divacancy, and the vacancy - interstitial pair.

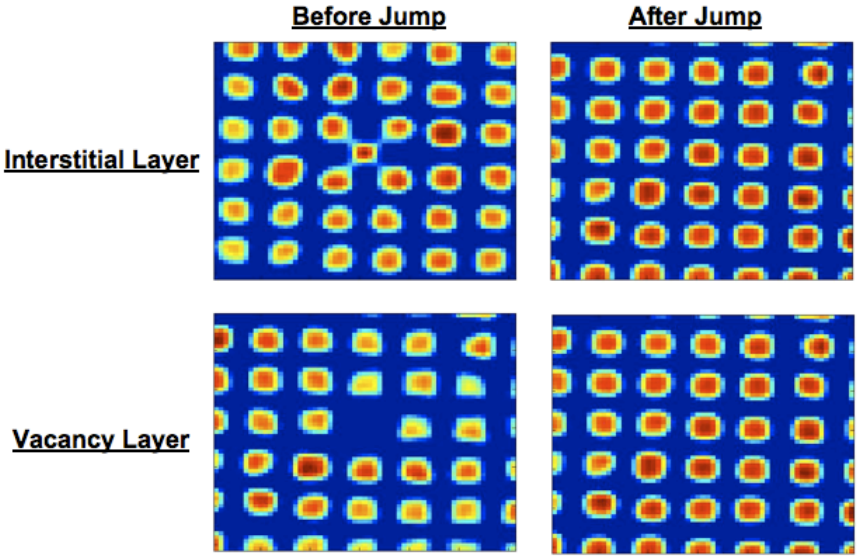

Figure 3.41: Annihilation of a vacancy - interstitial pair. The interstitial is next to a vacancy in the layer below. The right figures show the layers 30 min later. The interstitial has moved into the vacancy.

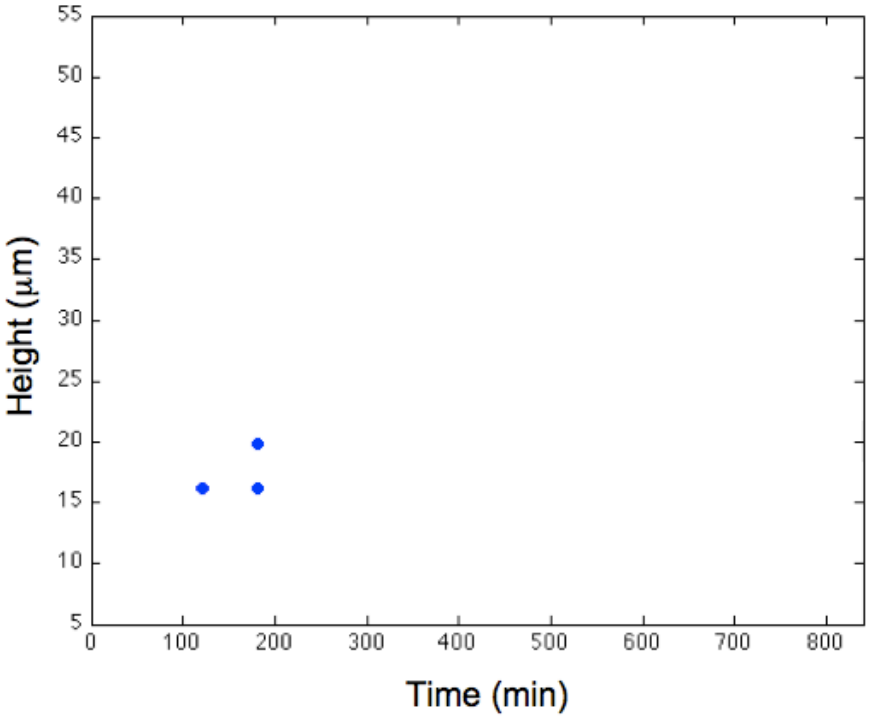

Figure 3.42: Time of the annihilation of the interstitial - vacancy pairs, as a function of their height.

4

Interaction Between A Dislocation and A Twin Boundary In A Hard-Sphere Colloidal Crystal

When a material is undergoing plastic deformation, dislocations nucleate and travel through the material to release strain energy [13]. The dislocation density increases with continuous deformation. When the number of dislocations is sufficiently large the dislocations start to run into each other. The energy required for dislocations to pass or cut one another leads to work hardening. Other defects can have a similar effect: grain boundaries are known to stop dislocations and lead to strengthening of the material by the Hall-Petch mechanism [13] [37]. A grain boundary with high symmetry and low energy is the twin boundary [13] [11]. It presents a well characterized, uniform obstacle for dislocation motion. This chapter investigates the interaction between a dislocation and a twin boundary in a

hard-sphere colloidal crystal.

4.1 Introduction

4.1.1 Twin Boundaries

Twin boundaries are grain boundaries. Their energy of formation is much lower than that of other grain boundaries since they have no density deficit and the coordination number of all the particles is maintained. The energy of formation of a $\{110\}$ $\sum 3$ coherent twin boundary is also lower than that of a stacking fault [13]. This can easily be seen when writing the different ABC layer arrangements. (See Figure 2.2 for showing an A layer, B layer, and a C layer in relation to each other). A perfect FCC has layer arrangements ABCABCABCABC. In a stacking fault, two HCP layers occur right next to each other producing layer arrangement of ABC**ABAB**CABC. For a twin boundary the layer structure is ABCA**BCB**ACBACB, only leaving on HCP layer in the middle. However, in hard-sphere colloidal crystals, both these energies are zero. Figure 4.1 shows the first layer of a $\{100\}$ $\sum$ 5 tilt grain boundary and a twin boundary. The density deficit in the $\sum$ 5 boundary should be noted.

Twins can arise during crystal growth or from shear deformation [13]. In FCC, the deformation twin is formed by displacing successive $\{111\}$ planes by $\frac{1}{6}a < 11\bar{2} >$ vector in the plane (i.e. A $\rightarrow$ B, B $\rightarrow$ C, C $\rightarrow$ A , see Figure 4.2), which produces a homogeneous shear of $\frac{\sqrt{2}}{2}$.

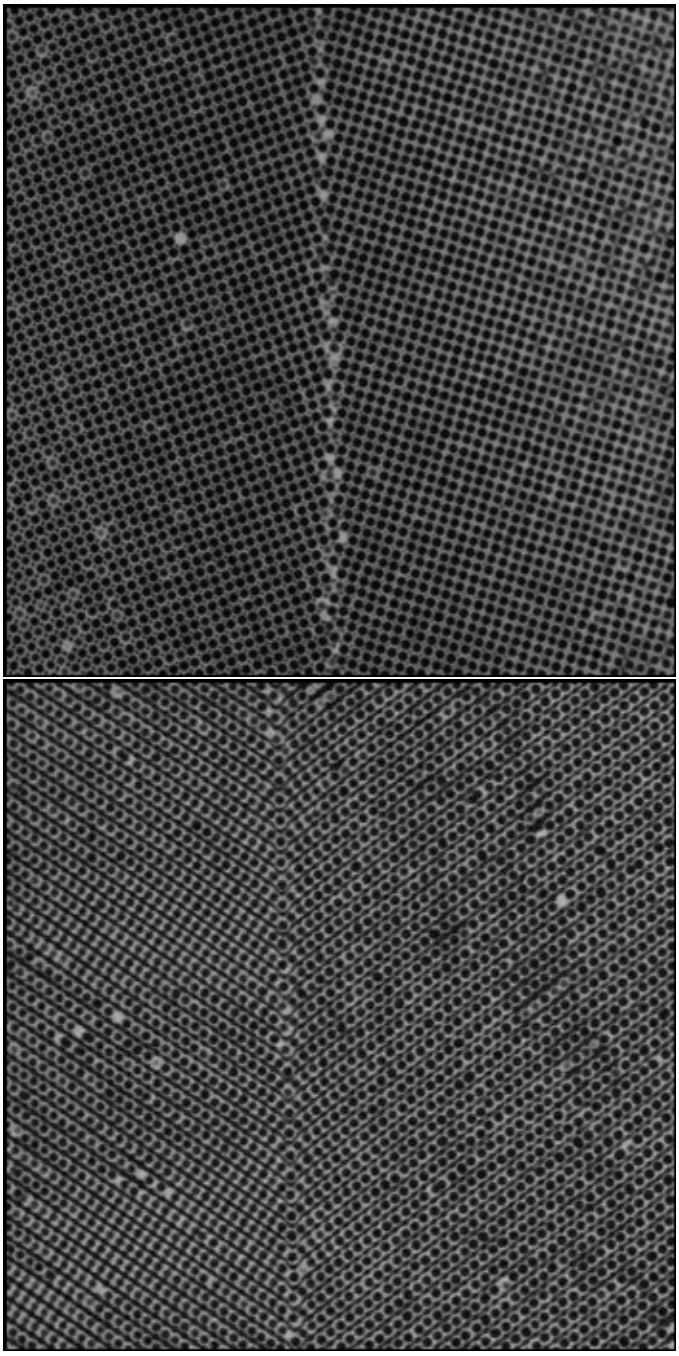

Figure 4.1: Top: the first layer of a {100} $\sum$ 5 tilt grain boundary. Bottom: first layer of a {110} $\sum$3 twin boundary for FCC crystals.

4.1.2 Grain boundaries as barriers to dislocation motion

The ability of grain boundaries to strengthen materials by acting as barriers to dislocation motion has long been known [13]. When the grain size is reduced, the yield stress, flow stress and hardness of metals and alloys usually increases. Hall and Petch found that the yield stress, σ_y, of polycrystalline α-iron is varies according to the relation [13] [37]- [38]:

$$\sigma_y = \sigma_o + kd^{-\frac{1}{2}} \tag{4.1}$$

where d is the grain size. The increase in yield strength arises from dislocation pile-up at the boundary [13]. This suggests that nanocrystalline metals should be materials with high hardness [37]. There is a limit, however, to how small these grains can be. Decreased hardness has been observed on nanostructures with grain size less than 10 nm [14] [16] [37]- [39]. If, however, twin boundaries are created in the grains, it is possible to create even harder materials. In pure Cu with an high concentration of twin boundaries in the normal grains, the yield strength has been found to reach four times its value without twins. Since twin boundaries block the motion of dislocations, their spacing must be considered as well in the Hall-Petch relationship [38]- [40].

4.1.3 Crystallography of twin-dislocation interactions in FCC

When dislocations pile-up next to a twin boundary, their combined stress field helps to press one or a few dislocations into and through the boundary. Sometimes the dislocations dissociate into two dislocations, where one stays at the boundary and the other one goes through. The crystallography of these interactions is presented below. [13] [14] [16] [41] [39]

4.1.3.1 Dislocation interaction with a twin boundary in FCC

In FCC crystals, the slip and the coherent twinning planes are {111}. A slip and a twinning plane meet at a $<1\bar{1}0>$. For an $(\bar{1}11)$ slip plane with lattice parameter a, the possible Burgers vectors for perfect dislocations are [42]: $\pm\frac{1}{2}a[01\bar{1}]$ (parallel to the slip and twin plane intersection), $\pm\frac{1}{2}a[110]$ (with an angle of $\pi/3$ to the slip and twin plane intersection), and $\pm\frac{1}{2}a[101]$ (with an angle of $\pi/3$ to the slip and twin plane intersection).

When a dissociated dislocation glides into a coherent twin {111} boundary, two reactions can occur. A cross-slip, which transforms the incoming dissociated dislocation into a dissociated dislocation in the twin plane, can happen if the incident Burgers vector is parallel to the twin. Burgers vectors not parallel to the twin plane can create an untwinning interaction or a climb in the twin boundary [43]. The first Burgers vector listed above is parallel with the slip plane-twin boundary intersection and therefore becomes a dislocation in the twin plane (indicated with a T below) [42]:

$$\frac{1}{2}a[01\bar{1}] \rightarrow \frac{1}{2}a[0\bar{1}1]_T \tag{4.2}$$

The other two, $\pm\frac{1}{2}a[110], \pm\frac{1}{2}a[101]$, must undergo dissociation reactions where each dislocation creates one slip dislocation in the twin plane and a partial dislocation at the interface. There are two possibilities for each case. For example the $\frac{1}{2}[110]$ can dissociate as [42]:

$$\frac{1}{2}a[110] \rightarrow \frac{1}{2}a[110]_T + 2 \times \frac{1}{6}a[11\bar{2}] \tag{4.3}$$

$$\frac{1}{2}a[110] \rightarrow \frac{1}{2}a[101]_T + \frac{1}{6}a[2\bar{1}\bar{1}] \tag{4.4}$$

These reactions are easily checked on a Thompson tetrahedron [42] [44].

In our colloidal crystals, the most common dislocation by introduced strain is not a full dislocation but a Shockley partial. In an atomic crystal, two Shockley partials bound a stacking fault and minimize its size. In the hard-sphere colloidal crystal, stacking faults have zero energy and therefore the repulsion between the partial dislocation makes them extend all the way through the crystal. For more details, see Section 4.1.5

4.1.4 Simulations and Earlier Experiments

In a simulation by Zhang et al. [14], a perfect dislocation with b=$\frac{1}{2}$[101] situated next to a Σ 3 (111) twin boundary in an FCC crystal was propagated through the boundary via glide. A partial Shockley dislocation with $\frac{1}{6}[\bar{1}\bar{1}\bar{2}]$ remained in the boundary as the perfect dislocation moved through, leaving a step in the boundary [14] [15]. Twin boundaries containing Shockley partial dislocations with a Burgers vector of $\frac{1}{6}a[\bar{1}\bar{1}2]$, have been found experimentally following tensile testing of FCC materials [41]. When the twins are far apart the dislocations pile-up next to the boundary. The stress concentration from that pile-up allows dislocations to slip through the boundary. A nanometer scale spacing is necessary to obtain high hardness [14]. The shorter the spacing between the twin boundaries, the higher the external stress required for the dislocation to cross the twin boundary, since fewer dislocations can pile-up at one boundary. If the spacing is so small that no dislocations can pile-up, a dislocation can still penetrate the twin boundary, but a very high stress is required [41].

4.1.5 Dislocations in Colloidal Crystals

Dislocations in colloidal crystals can be introduced by either deforming the crystal (i.e. by indentation) [6], by introducing a strain in the template (by patterning the holes at distance different from the ideal one for a given crystal height), or by growing a crystal thicker than the critical thickness for a given template [4]. The work in this chapter has concentrated on the third approach.

In order to understand the dislocation behavior in a strained crystal, we need to know the elastic constants of colloidal crystals. The discussion below follows the approach described in Schall and Spaepen's review [18]:

4.1.5.1 Elastic behavior of colloidal crystals

Colloidal crystals have small elastic moduli. The equation of state is:

$$pV = Z(V)k_BT \tag{4.5}$$

The bulk modulus defined as:

$$K = -\frac{V dp}{dV} \tag{4.6}$$

which for the above equation of state is:

$$K = \frac{Zk_BT}{V}(1 - \frac{V}{Z}\frac{\delta Z}{\delta V}) \tag{4.7}$$

For our crystals, K is 1-10 Pa [17].

The shear modulus, μ, can be found by taking the second derivative of the Helmholtz free energy density, Helmholtz free energy over volume, with

respect to the shear strain, γ:

$$\mu = \frac{1}{V}\frac{\delta^2 F}{\delta\gamma^2} \tag{4.8}$$

Since the only internal energy to consider that does not depend on γ is the thermal energy, $U_{thermal}$, we get:

$$\mu = -\frac{T}{V}\frac{\delta^2 S}{\delta\gamma^2} \tag{4.9}$$

In hard-sphere colloidal crystals under our conditions μ has been computed to be 5.0 Pa for the parallel shear and 0.8 Pa for the shear at 45^o [33], which is surprisingly anisotropic.

4.1.5.2 Critical thickness of a strained colloidal crystal

By introducing strain into the template, coherency (or misfit) dislocations may appear to relieve the strain by creation of Shockley partial dislocations with Burgers vectors b=$\frac{a}{6}$<112>. Only the component parallel to the template relieves strain, so that the effective Burgers vector becomes bcos(α), where α is the angle between the plane and the vector.

The growing crystal needs to reach a critical thickness for misfit dislocations to be formed. The strain relieved by dislocations spaced L apart is:

$$\varepsilon = \frac{bcos(\alpha)}{L} \tag{4.10}$$

If the crystal has a Young modulus E and height h, the elastic energy per unit area is:

$$U_{elastic} = \frac{1}{2} E \varepsilon_{elastic}^2 h \tag{4.11}$$

where the elastic strain, $\varepsilon_{elastic}$, is the difference between the initial strain, ε_0, and the strain relief provided by the dislocations, ε:

$$\varepsilon_{elastic} = \varepsilon_0 - \varepsilon \tag{4.12}$$

Using equation 4.11 and 4.12, $U_{elastic}$ becomes:

$$U_{elastic} = \frac{1}{2} E (\varepsilon_0 - \frac{bcos(\alpha)}{L})^2 h \tag{4.13}$$

The energy per unit area of the dislocations is:

$$U_{dislocation} = \frac{1}{L} \frac{\mu b^2}{4\pi(1-\nu)} ln \frac{R}{r_o} \tag{4.14}$$

Here, ν is Poisson's ratio, computed to be 0.37 under our conditions [33], R is the distance away from the dislocation at which the crystal still feels its strain. In this case, R is the height of the crystal, h. r_o is the effective core radius equal to b/4 [13]. By minimizing the total energy with respect to the dislocation spacing, we obtain:

$$\frac{1}{L} = \frac{\varepsilon_0}{bcos(\alpha)} - \frac{1}{4\pi(1-\nu)} \frac{\mu}{E} \frac{1}{cos^2(\alpha)} \frac{1}{h} ln \frac{4h}{b} \tag{4.15}$$

At the critical thickness, h_c, the dislocation spacing is infinite. This gives:

$$h_c = \frac{1}{4\pi(1-\nu)} \frac{\mu}{E} \frac{1}{\varepsilon_0} \frac{b}{cos(\alpha)} ln \frac{4h_c}{b} \tag{4.16}$$

For an isotropic medium, Young modulus, the shear modulus, and

Poisson's ratio are related:

$$\frac{E}{\mu} = 2(1+\nu) \tag{4.17}$$

This is a simplified version. Jensen et al. [17] have incorporated the dependence of the bulk and shear moduli on the compressibility factor, Z, which further depends on the volume fraction, which varies with crystal depth due to the pressure head [24].

4.1.5.3 Offset distance from template

Once the dislocations have nucleated, they move to relieve as much strain energy as possible. However, since there is a boundary condition of zero displacement at the template, the dislocation motion must stop a few micrometers above the glass slide. This offset distance, z_o, can be calculated by considering the elastic energy per unit area. The energy below the dislocations at height z is given by.

$$U_{elastic} = \frac{1}{2} E \varepsilon_0^2 z \tag{4.18}$$

The force acting to pull the dislocation towards the template, when the dislocations are separated L apart, is the vertical gradient of $U_{elastic}$:

$$F_{elastic} = \frac{1}{2} L E \varepsilon_0^2 \tag{4.19}$$

The zero-displacement boundary condition is applied by placing an image dislocation at a distance z below the template, which repels the real dislocation. The vertical repulsive force between the image and the real dislocation is:

$$F_{repel} = \frac{\mu(bcos(\alpha))^2}{4\pi(1-\nu)z} \tag{4.20}$$

The offset distance z_o is found by balancing the forces and solving for z:

$$z_o = \frac{(bcos(\alpha))^2}{2\pi(1-\nu)L\varepsilon_0^2}\frac{\mu}{E} \tag{4.21}$$

This predicts an offset distance of one or two crystal planes, in accordance with observation [4].

4.2 Experiments

4.2.1 Crystal growth

The colloidal suspension was prepared as described in Chapter 2. The sample cell was filled halfway and the crystal was left to grow overnight. Then the sample cell was filled to the top and at the same time placed on a microscope to be scanned during growth every 15 min for 17.5 hours. A grid was mounted 50 μm over the template so that a shearing experiment could be performed after 17.5 hours. However, the event presented in this chapter occurred before shearing started due to 4.5% strain via a misfit template. For the amount of colloids in our sample, and the volume fraction, the expected height can be obtained from Equation 2.16 as 71 μm, which matched the experimental value (Figure 4.3).

The color scheme in Figure 4.3 indicates the order parameter of each particle, based on the nearest neighbor arrangement, as described by Ramsteiner et al. [45]. With nearest neighbors defined within distance $1.025a$,

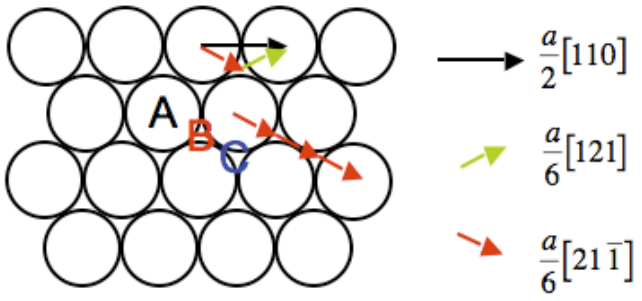

Figure 4.2: Position of an A layer, B layer, and C layer drawn along with the <110> and the $\frac{1}{6}a < 11\bar{2} >$ direction. The red arrow indicates A $\rightarrow$ B $\rightarrow$ C.

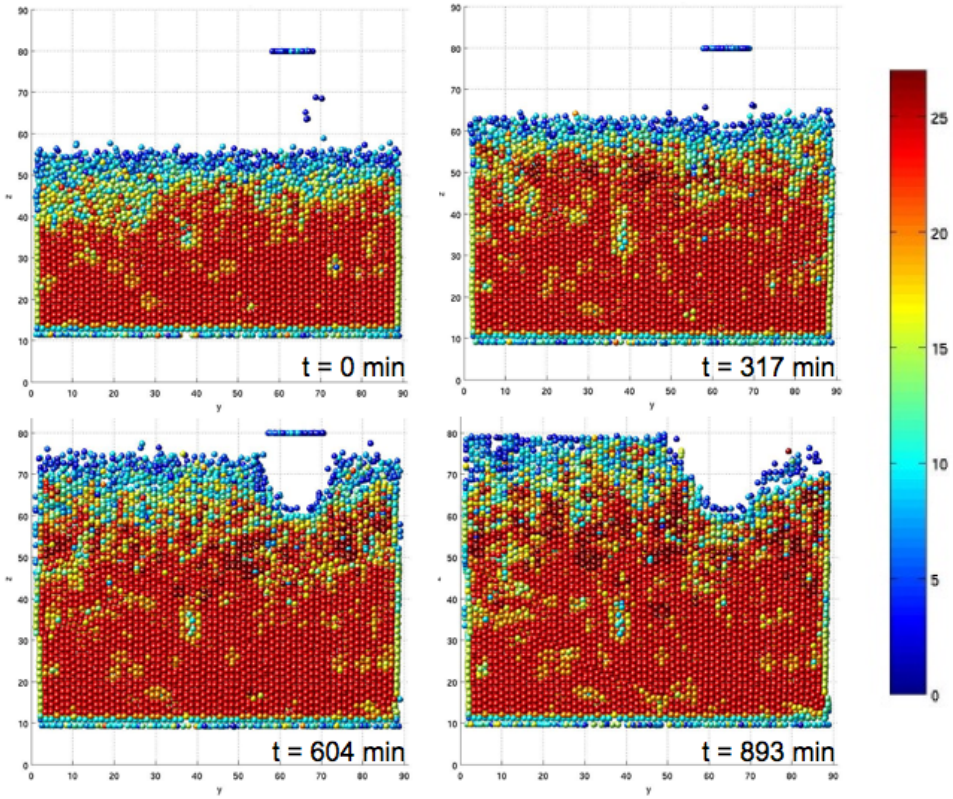

Figure 4.3: Crystal growth versus time after 0min, 317 min, 604 min, and 893 min. The color scheme indicates the order parameter of each colloid. A colloid with an order parameter of 20 or above is considered crystalline.

where a is the template lattice parameter (2.31 μm), a particle is considered to be crystalline if it has an order parameter of 20 or larger. In order to obtain the growth rate of the crystal, shown in Figure 4.5, the number of particles with order parameter equal to 20 or above were counted. That number was divided by the number of colloids that would ideally make up one layer. Each layer is a {110} plane with lattice parameter a, leaving an area per particle, $A_{particle}$:

$$A_{particle} = \frac{a^2}{\sqrt{2}} \tag{4.22}$$

From the radial distribution, Figure 4.4, the lattice parameter is 2.30 μm. The number of particles in a layer is simply the area of a square with length L divided by $A_{particle}$.

$$N_{layer} = \frac{A_{total}}{A_{particle}} = \frac{\sqrt{2}L^2}{a^2} \tag{4.23}$$

Excluding the edges of the layers (since for these no order parameters can be defined), by choosing L to be 85 μm, N_{layer} was 1947. However, each layer has some particles with non-crystalline coordination, as shown in Figure 4.3. The fraction of non-crystalline particles in the first 20 μm of the crystal height is on average 10%. This needs to be taken into account if the right crystal growth rate is to be found. The result is shown in Figure 4.5. We can see a constant growth rate for the first 900 min, whereafter the growth levels off due to lack of colloids in the fluid above.

A linear line of best fit can be performed on the first 900 min data in Figure 4.5. A few layers needs to be added since the bottom layers do not

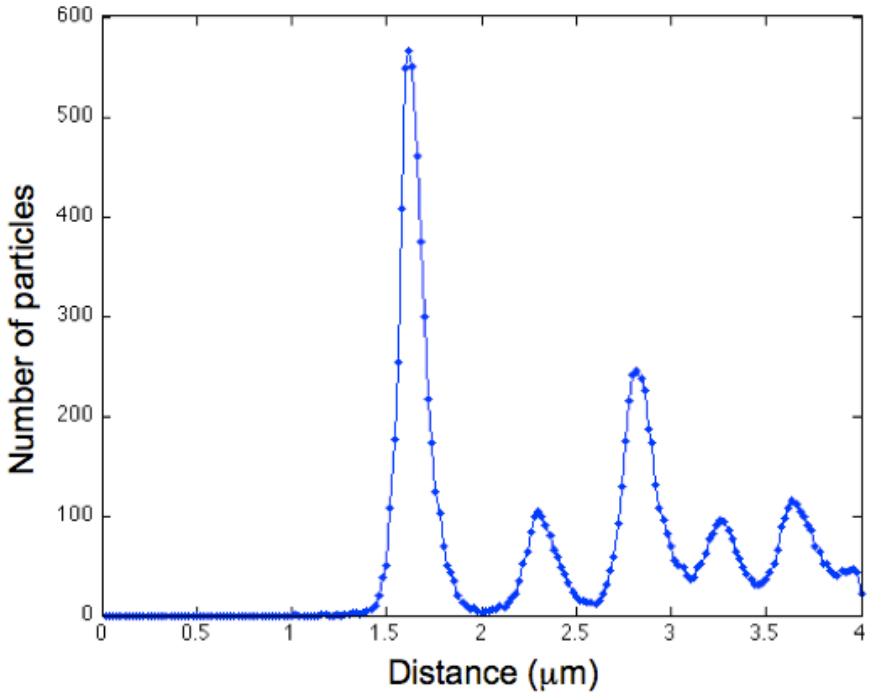

Figure 4.4: Pair distribution of the crystal. The nearest neighbor peak is located at 1.62 μm, and the second nearest neighbor distance (the lattice parameter a) is located at 2.30 μm.

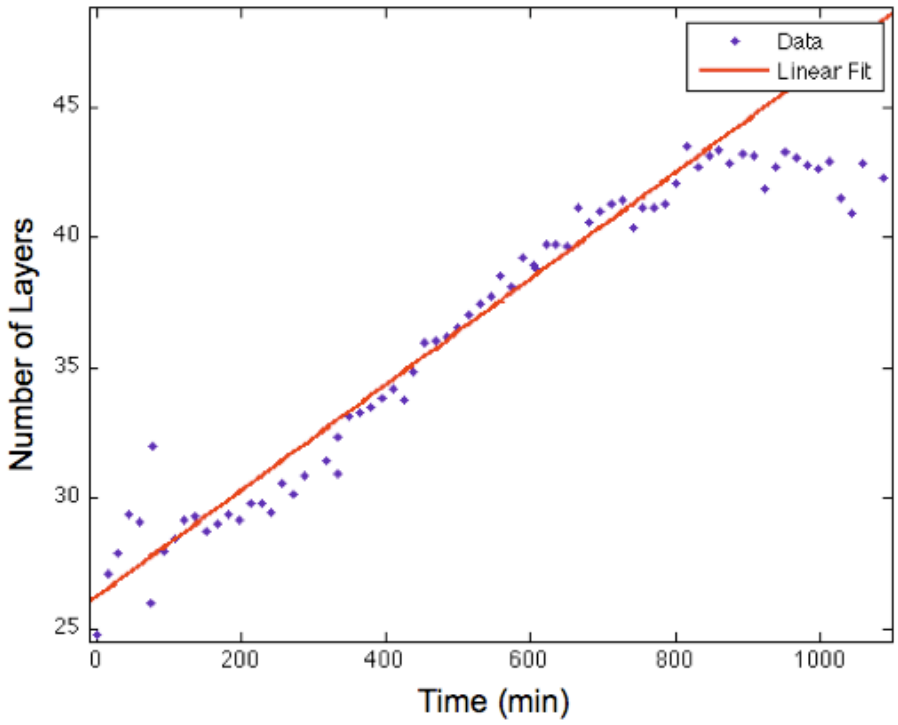

Figure 4.5: Number of crystal layers vs. time. The crystal growth rate is constant for the first 900 min.

show an order parameter of 20 or above, even though they are crystalline (an artifact due to the edge effect of missing neighbors). The result is:

$$h(Number\,of\,layers) = 0.022t + 28.38 \quad (0 \leq t \leq 900min) \tag{4.24}$$

Or, since the thickness of one layer, t_{layer}, is $\frac{a}{2\sqrt{2}}$= 0.82 μm:

$$h(\mu m) = 0.018t + 23 \quad (0 \leq t \leq 900min) \tag{4.25}$$

The expected growth rate can be calculated by considering the flux, J, the settling velocity, $v_{settling}$, times the number density of colloids in the solution, $n_{ColloidsInSolution}$:

$$J = v_{settling} n_{ColloidsInSolution} \tag{4.26}$$

The total amount of particles per time, Γ, is the flux multiplied by the cross sectional area, $A_{CrossSection}$:

$$\Gamma = J\,A = v_{settling} n_{ColloidsInSolution} A_{CrossSection} \tag{4.27}$$

In order to find the number density of colloids in our solution, $n_{ColloidsInSolution}$, we need the density of silica in the raw stock, $\rho_{SilicaInRawStock}$, and the mass of a colloid, $m_{colloid}$, from Chapter 2 and the fraction of raw stock used, $f_{RawStock}$.

$$n_{ColloidsInSolution} = \frac{\rho_{SilicaInRawStock}}{m_{colloid}} f_{RawStock} \tag{4.28}$$

Dividing the Γ by the number of particles per layer, $N_{layer} = \frac{A_{CrossSection}}{A_{particle}} = \frac{A_{CrossSection}}{\sqrt{2}a^2}$ we get the number of layer per time. Further, multiplying this with the thickness per layer, t_{layer}, we get the rate at which the crystal

should grow, h_{Theory}:

$$h_{Theory} = \frac{\Gamma}{N_{layer}} t_{layer} = \frac{v_{settling} \rho_{SilicaInRawStock} f_{RawStock} A_{particle}\, t_{layer}}{m_{colloid}} \tag{4.29}$$

From Chapter 2 we can find $\rho_{SilicaInRawStock}$, $v_{settling}$, and $m_{colloid}$. $A_{particle}$ and t_{layer} are both given above. With a $f_{RawStock}$ of 0.087 we obtain that the crystal grows at a speed of 0.15 μm/min, about an order of magnitude faster than our experiment shows. One reason for the difference could be the presence of a grid covering the top. Some particles settle on top of the grid, as shown in Figure 4.3, but more importantly, due to the grid holder, the density of colloids settling in the liquid, $\rho_{ColloidsInSolution}$, directly above the grid will be less than that of the suspension as a whole.

4.2.2 Determination of Dislocations, Stacking faults, and Twin Boundaries

The dislocations and stacking faults in our sample were identified by the method of Schall et al. [6]. Every particle with twelve nearest neighbors where all opposite pair neighbors make an angle close to 180^o are counted as perfect FCC. If the particle has three opposite pair nearest neighbors with angles near 180^o but also three with angles less than 155^o, its local coordination is that of HCP and its presence indicates a stacking fault or twin boundary, as discussed in Section 4.1.1. A particle that does not meet either the HCP or FCC conditions, with angles between 155-160^o, often lies in a dislocation core.

4.2.3 Observation of the interaction between a stacking fault and a twin

Figure 4.6 depicts the development of a stacking fault (red particles) as it approaches and traverses the twin boundary. The stacking faults are bounded by the dislocations (yellow particles) that drive the motion. The FCC-coordinated particles have been taken out for an easier visualization.

The boundary halts the motion of the dislocation for some time. When the dislocation does go through, another dislocation moves backwards, which can be seen from the bottom of the stacking fault, as shown in Figure 4.7. This dislocation creates a twin plane between the two stacking faults.

Figure 4.8 shows a cross-section view perpendicular to the twin boundary with the FCC-coordinated particles shown. The formation of the new twin plane is clearly visible. We can also see a shift in the position of the boundary, indicating that the event left behind a dislocation at the boundary.

4.2.4 Analysis of the Dislocation - Twin Interaction

First, we need a crystallographic analysis of the conservation of Burgers vectors throughout the entire interaction. Secondly, we need to understand why the dislocation stays a certain amount of time at the boundary and why it stops moving once it has passed through.

4.2.4.1 Rotation of coordinate system

In Figure 4.9 the crystal directions for the left-hand crystal are shown. The unit vectors of the microscope coordinates $(\hat{x}, \hat{y}, \hat{z})$ correspond to the three

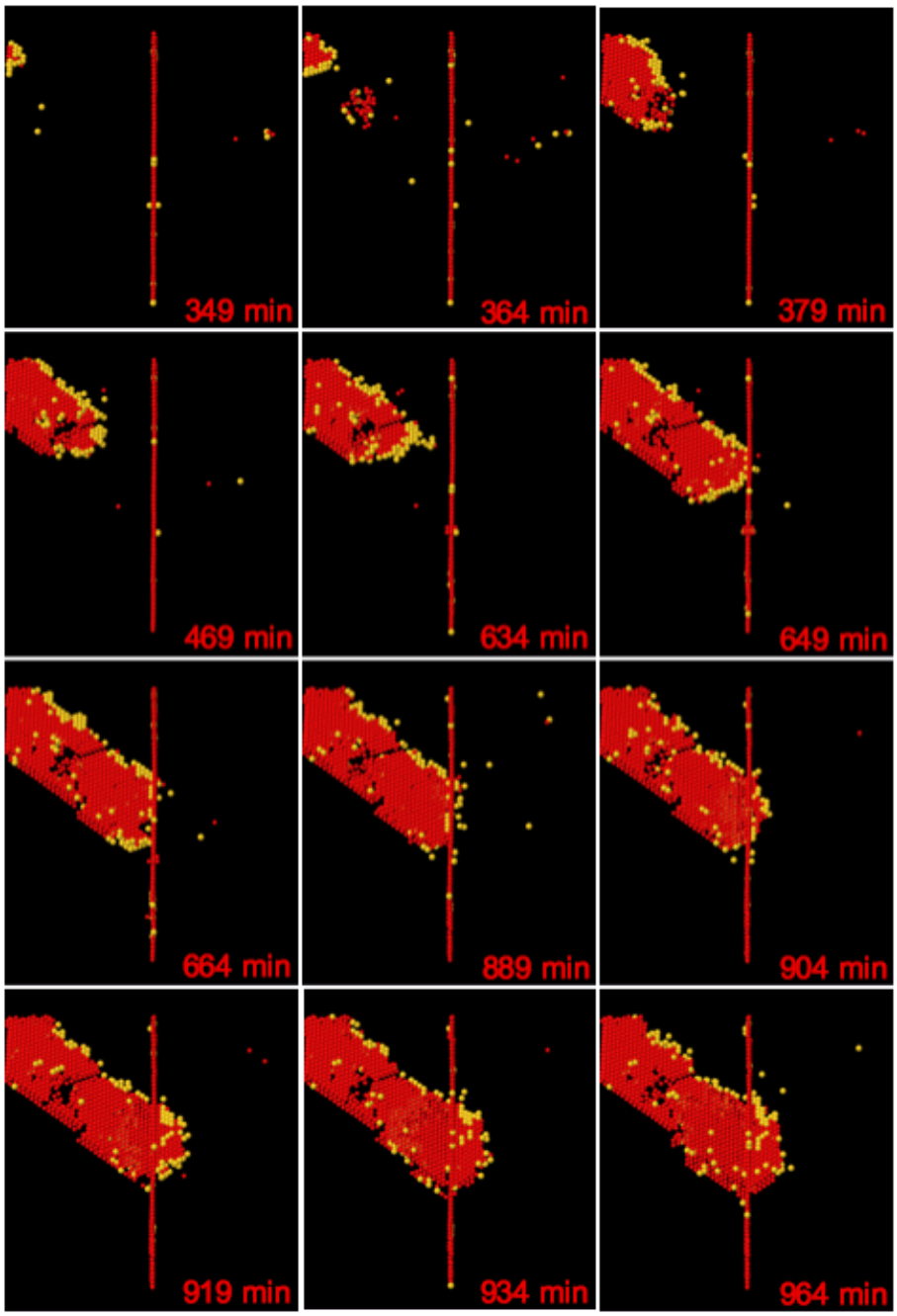

Figure 4.6: Snap shots of a stacking fault and a dislocation moving towards a twin boundary, stopping at the boundary, and later passing through. The red particles indicate stacking faults and twin configurations among nearest neighbors. The yellow particles indicate dislocations. Particles with perfect FCC coordination have been taken out.

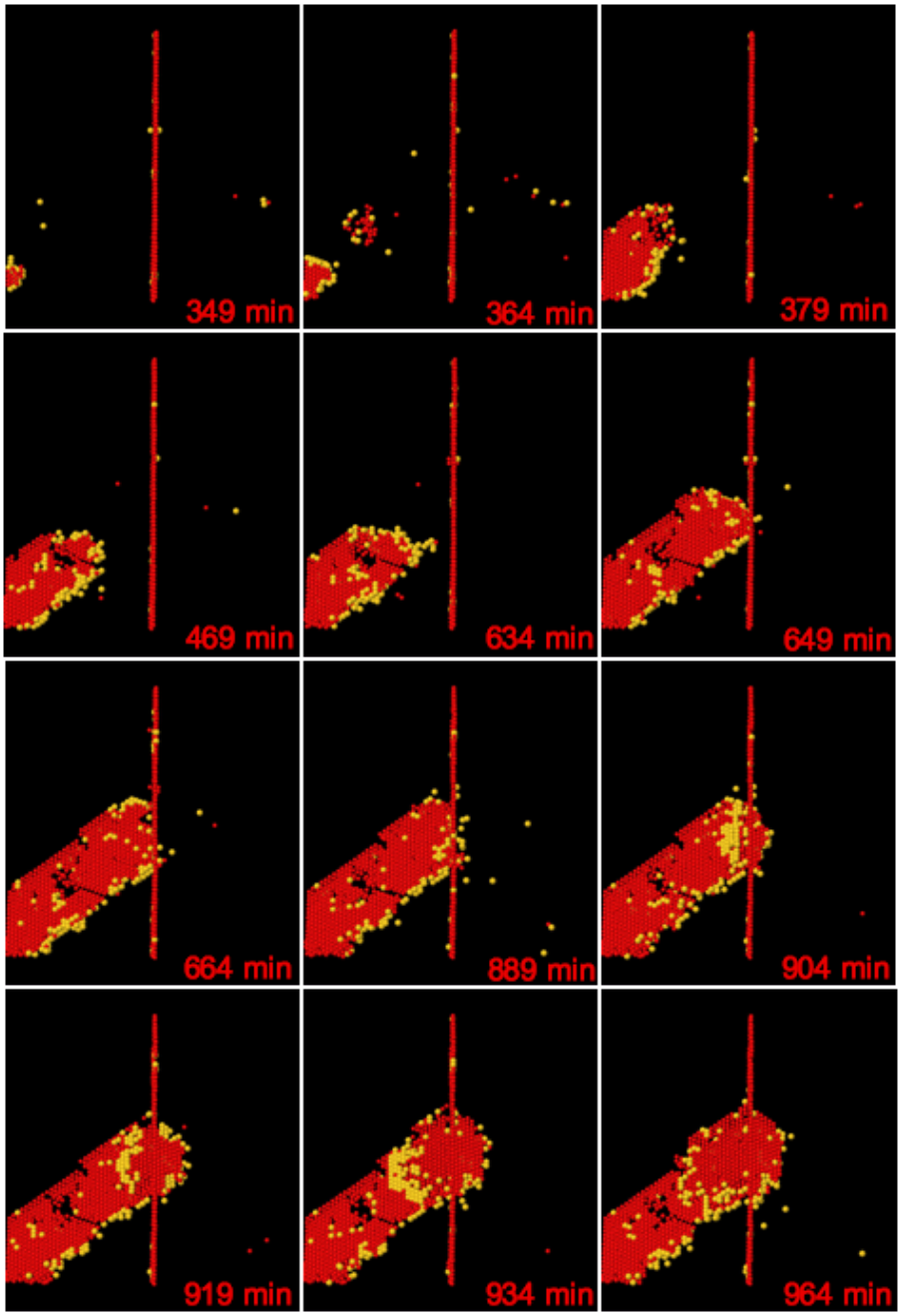

Figure 4.7: Same event as in that shown in Figure 4.6 but with images taken from the bottom. Note that when the dislocation is passing through the boundary, another dislocation is reflected back.

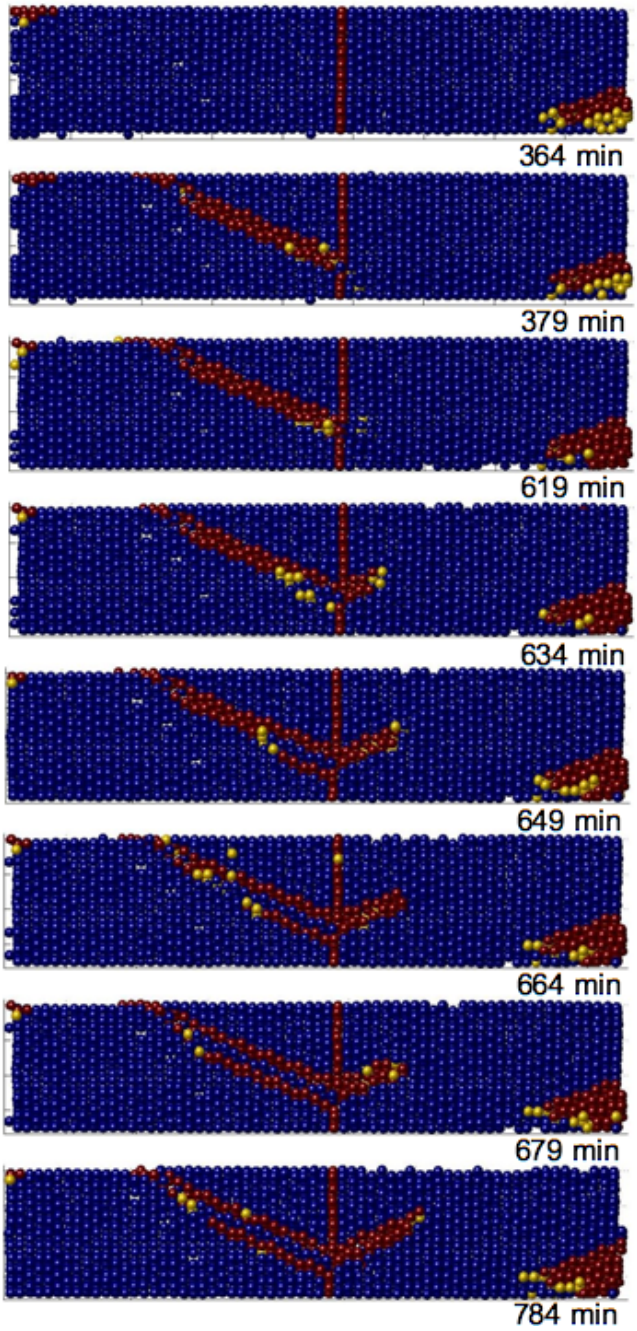

Figure 4.8: Side view of a 5μm thick cut through the stacking fault plane. The blue particles indicate particles with FCC coordination, the red particles indicate the stacking fault and the twin boundary. The yellow particles indicate the dislocation. One can see a step left behind in the twin boundary when the transmitted and reflected dislocation have nucleated.

crystal unit vectors:

$$[\hat{x}00] \rightarrow \frac{1}{\sqrt{6}}[\bar{1}2\bar{1}] \tag{4.30}$$

$$[0\hat{y}0] \rightarrow \frac{1}{\sqrt{3}}[\bar{1}\bar{1}\bar{1}] \tag{4.31}$$

$$[00\hat{z}] \rightarrow \frac{1}{\sqrt{2}}[\bar{1}01] \tag{4.32}$$

These unit vectors are then used to create a rotation matrix to express the particle coordinates in the crystal coordinate system:

	[100]	**[010]**	**[001]**
$[\hat{x}00]$	$-\frac{1}{\sqrt{6}}$	$\frac{2}{\sqrt{6}}$	$-\frac{1}{\sqrt{6}}$
$[0\hat{y}0]$	$-\frac{1}{\sqrt{3}}$	$-\frac{1}{\sqrt{3}}$	$-\frac{1}{\sqrt{3}}$
$[00\hat{z}]$	$-\frac{1}{\sqrt{2}}$	0	$\frac{1}{\sqrt{2}}$

Table 4.1: Rotation matrix for left side of the crystal.

Here, the new, desired, coordinates are written at the top and the old equivalent coordinates in the microscope coordinate system are written on the left side. The same procedure was performed for the right side (Figure 4.10):

$$[\hat{x}00] \rightarrow \frac{1}{\sqrt{6}}[121] \tag{4.33}$$

$$[0\hat{y}0] \rightarrow \frac{1}{\sqrt{3}}[\bar{1}1\bar{1}] \tag{4.34}$$

$$[00\hat{z}] \rightarrow \frac{1}{\sqrt{2}}[\bar{1}01] \tag{4.35}$$

These unit vectors are now used to create the right hand side rotation matrix: Figure 4.11 shows the twinned crystal with its stacking faults and disloca-

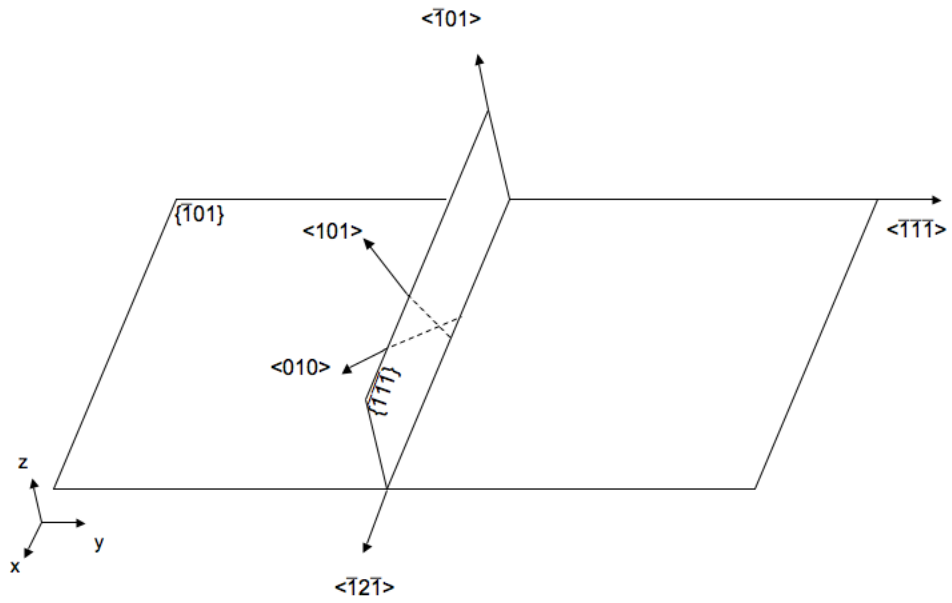

Figure 4.9: Crystallographic directions of the crystal to the left of the twin boundary.

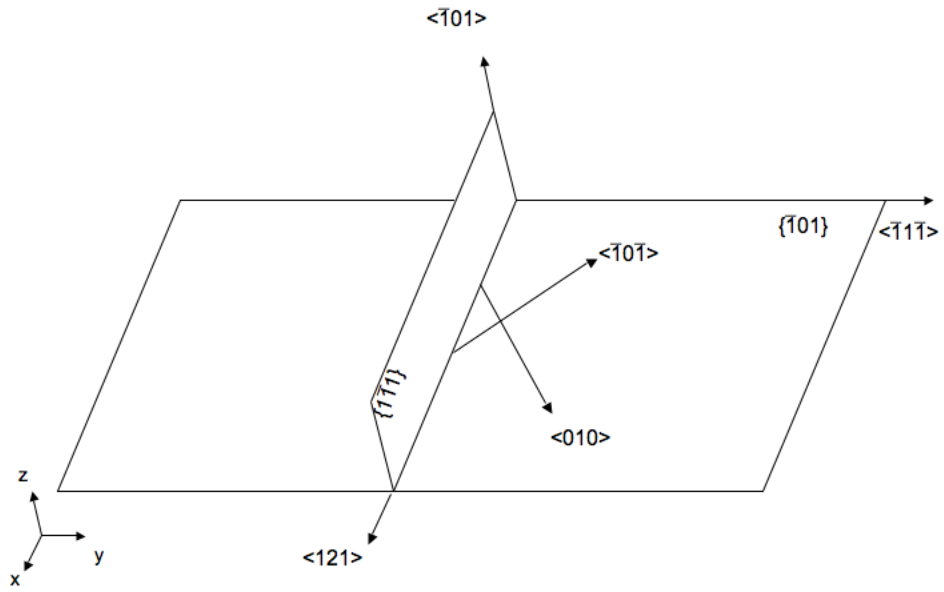

Figure 4.10: Crystallographic directions of the crystal to the right of the twin boundary.

	[100]	**[010]**	**[001]**
$[\hat{x}00]$	$\frac{1}{\sqrt{6}}$	$\frac{2}{\sqrt{6}}$	$\frac{1}{\sqrt{6}}$
$[0\hat{y}0]$	$-\frac{1}{\sqrt{3}}$	$\frac{1}{\sqrt{3}}$	$-\frac{1}{\sqrt{3}}$
$[00\hat{z}]$	$-\frac{1}{\sqrt{2}}$	0	$\frac{1}{\sqrt{2}}$

Table 4.2: Rotation matrix for right side of the crystal.

tions.

4.2.4.2 Determination of the Burgers vectors

Following rotation, the Burgers vectors were found by tracing Burgers circuits around the initial and final states of the process. Figure 4.12 shows the procedure. A Shockley partial dislocation is coming in towards the boundary with a Burgers vector of $\frac{a}{6}[112]$. When it penetrates the boundary it creates three dislocations: one that goes through the boundary with Burgers vector $\frac{a}{6}[112]$, one that moves back, with Burgers vector $\frac{a}{6}[112]$, and one that stays in the boundary with Burgers vector $\bar{b}_t$.

Conservation of Burgers vector requires:

$$\frac{a}{6}[112]_{LeftCrystalSystem} = \frac{a}{6}[112]_{LeftCrystalSystem} + \frac{a}{6}[112]_{RightCrystalSystem} + \bar{b}_t \tag{4.36}$$

Hence

$$\bar{b}_t = -\frac{a}{6}[112]_{RightCrystalSystem} \tag{4.37}$$

If we rotate b_t back to the microscopic coordinate system and multiply by -1, we obtain:

$$\bar{b}_t = [0.2556, -0.8944, -0.1278] \tag{4.38}$$

This Burgers vector was measured in our experiment in multiple steps as

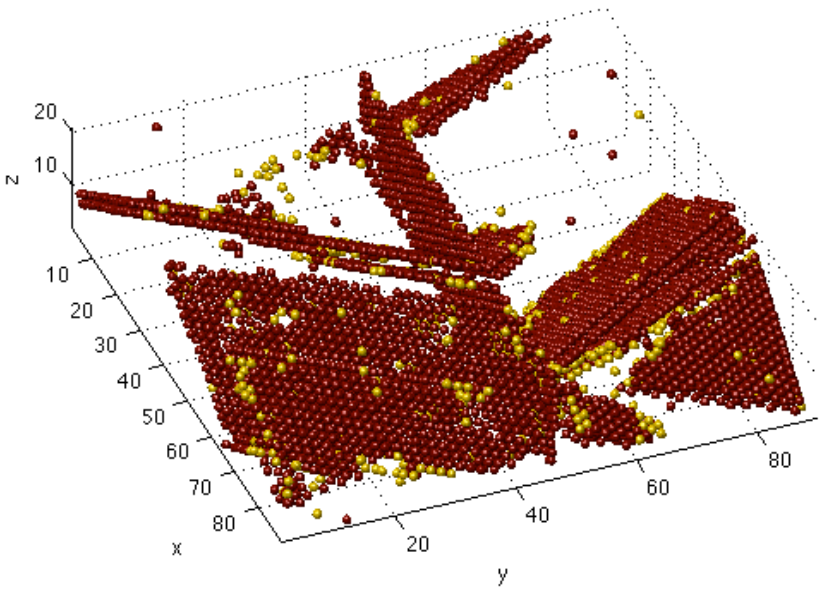

Figure 4.11: The stacking faults (red particles), the twin boundary (red particles), and the dislocations (yellow particles) in the microscope coordinate system. Particles with perfect FCC coordination have been removed.

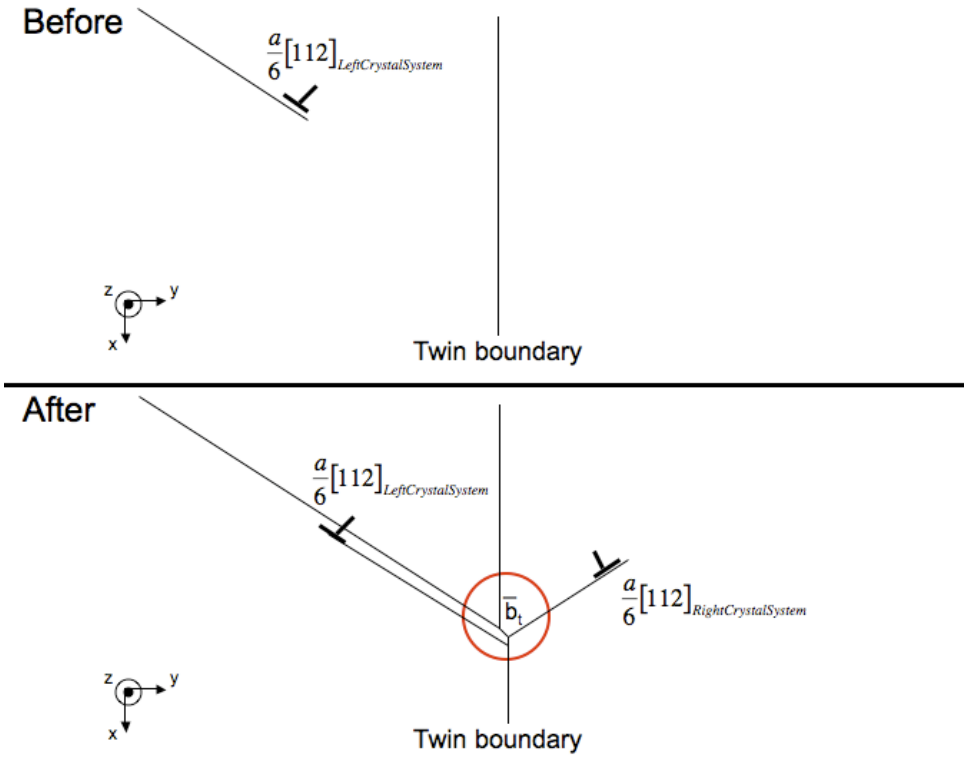

Figure 4.12: Conservation of the Burgers vectors in the interaction between a stacking fault and a twin boundary.

shown in Figure 4.13. First the crystal was rotated to a {100} crystal plane. Second, the two extra half planes were identified. It is easy to see here that the Burgers vectors are equal and opposite. Third, we can find the Burgers vector's direction, identified with help of a Burgers circuit, of the transmitted dislocation. Fourth, the average direction and magnitude of two vectors were found, whose difference is the desired Burgers vector of the transmitted dislocation. Finally, the vector was rotated back to microscopic coordinate system and the result of the vector in the boundary becomes:

$$\bar{b}_{t,exp} = [0.2756, -0.7203, -0.2759] \tag{4.39}$$

The magnitude of the computed Burgers vector is 0.94 μm, while the experimental value is 0.81 μm. A small part of this difference can be explained by the change in nearest neighbor distance as we move away from the template. The computed value is based on the spacing in the template but, when stacking faults relieve this strain energy, they shorten the lattice parameter. Some uncertainty also lies in each rotation performed.

4.2.4.3 Dislocation motion

By plotting the number of particles in the stacking fault belonging to the dislocation versus time, one can see how the dislocation moves forward in steps, as shown in Figure 4.14, and previously observed in Figures 4.6, 4.7, and 4.8.

Both steps involve a build-up time of 4.5 hours before the dislocation moves again. The jumps in stacking fault particles are about the same, 336

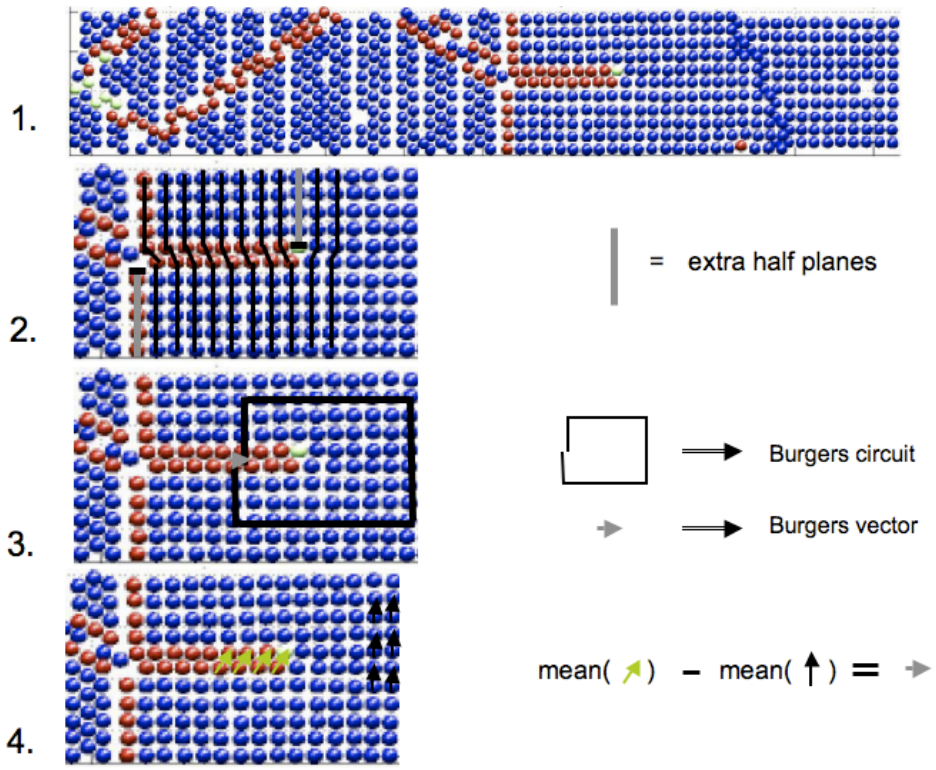

Figure 4.13: The Burgers vector at the boundary was found in four steps: 1. Rotate the crystal to find the perpendicular {100} plane to the template. 2. Identify the two extra half planes. Their Burgers vectors are equal and opposite. 3. Create a Burgers circuit and identify the direction of the Burgers vector around the transmitted dislocation. 4. Find the Burgers vector by measuring the average of the two types of vectors indicated green and black in the picture, subtract the two, and rotate the vector back again. The Burgers vector in the boundary will be equal and opposite.

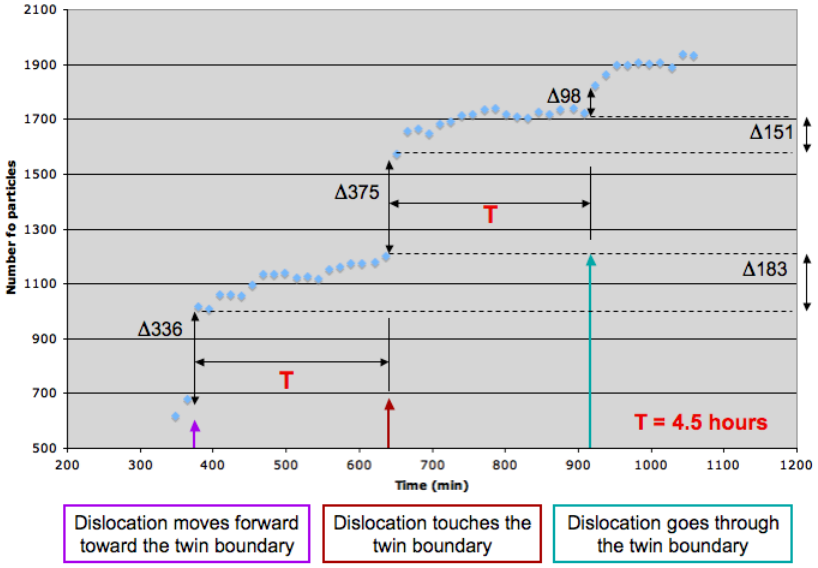

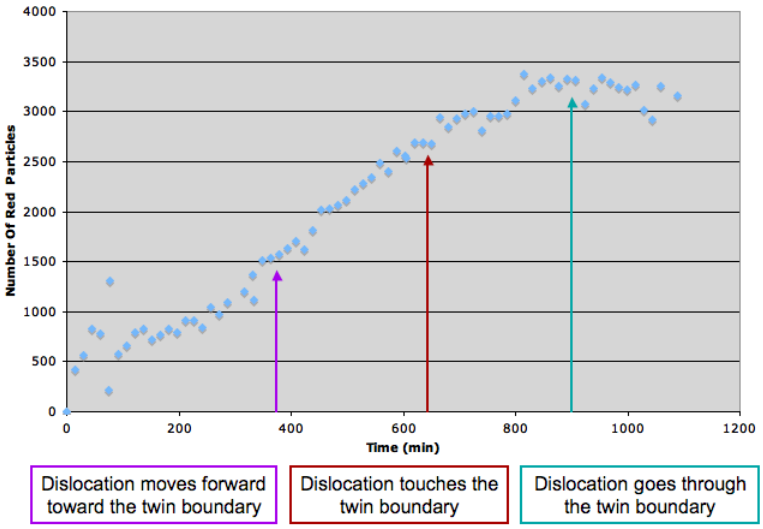

Figure 4.14: Top: the number of particles in the stacking fault bounded by the moving dislocation as a function of time. Bottom: the crystal growth with the dislocations major movements indicated.

at the first step and 373 at the second. The build-up in particles is also similar: 183 and 151.

When the dislocation penetrates the boundary, it leaves a stacking fault behind on one side (penetrated stacking fault) and a twin plane on the other (reflected stacking fault). Figure 4.15 shows that, following penetration, the number of particles in the penetrated stacking fault (blue) is similar to the number of particles in the reflected stacking fault (red).

We will later discuss the strain relieved by the stacking fault. For that analysis we need the area of the stacking faults. Since there are two layers in a stacking fault the area per particle in a stacking fault is half that of a particle in a {111} plane:

$$A_{perParticle} = \frac{\sqrt{3}a^2}{4} \tag{4.40}$$

where a is the lattice parameter.

The length travelled by the stacking fault is compared to the length travelled by the reflected dislocation, featured in Figure 4.16. The reflected dislocation reaches almost twice the distance compare to the transmitted dislocation. However, the reflected stackingfault retracts slightly at the end as the transmitted grows further. The velocity of the dislocation can be extracted from the slopes of this graph. The velocity is high at the beginning, about 0.324 μm/min, and then it levels of to be close to zero. For a more details on the dislocation velocity, see Section 4.2.6. The dislocation does go through the boundary just shortly after the crystal has stopped growing as seen in Figure 4.14. When there is no more strain energy left to relieve, the

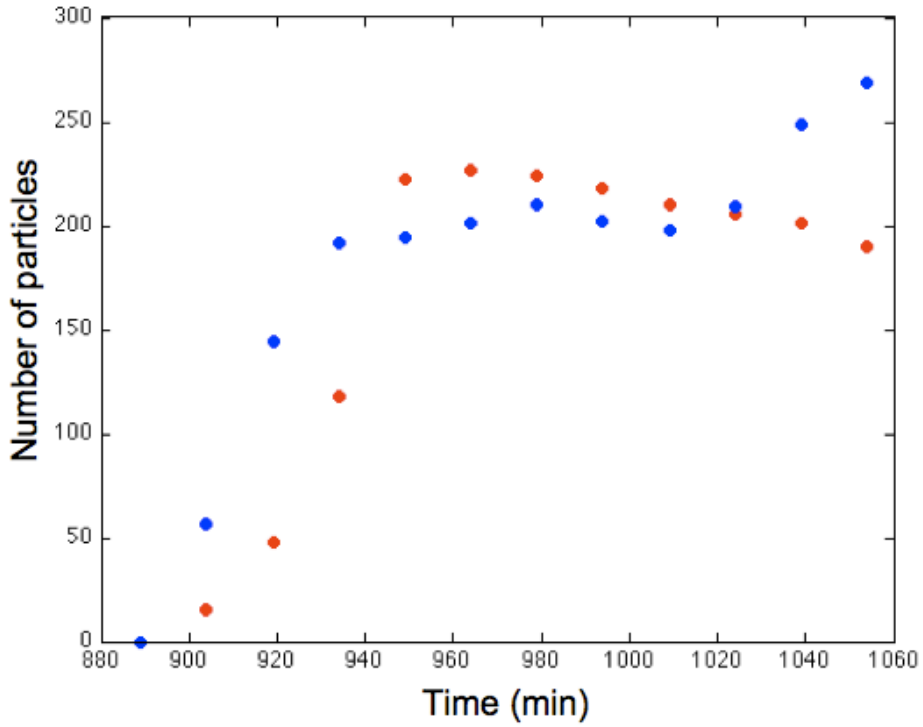

Figure 4.15: Number of particles in the stacking fault following the dislocation going through the twin boundary (blue) and the stacking fault behind the dislocation that is reflected (red)

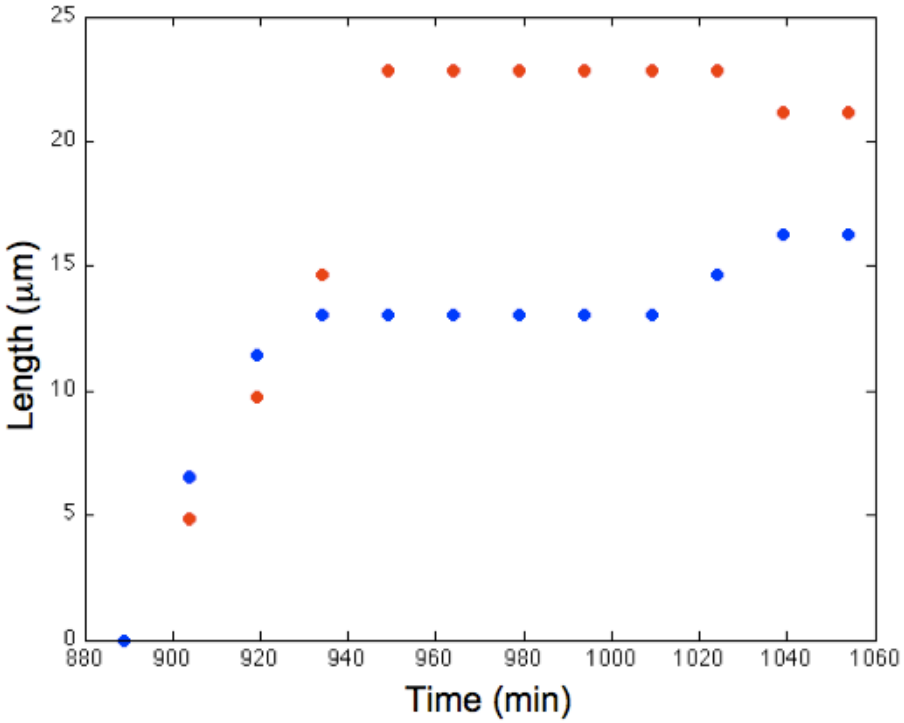

Figure 4.16: Distance travelled by the edge of the stacking fault following the dislocation going through the twin boundary (blue) and by the dislocation that gets reflected (red)

dislocation stops.

4.2.5 Strain Relieved

The dislocation will travel in the crystal until is relieves as much strain energy as possible. The amount of strain relieved by our dislocations can be found by considering the area they sweeps out. In reference to Figure 4.17, the strain relieved by the extra half plane of width L_2 and Burgers vector, b, in a box of length L_1 is:

$$\Delta\varepsilon = \frac{b}{L_1} \tag{4.41}$$

More generally, if the dislocation has a irregular shape, corresponding to a half plane with area A as in Figure 4.17, we need to consider the fraction crystal plane covered by the half plane:

$$\Delta\varepsilon = \frac{b}{L_1}(\frac{A}{hL_2}) = \frac{bA}{V} \tag{4.42}$$

In this experiment the stacking fault is coming in at an angle depicted in Figure 4.19, for which we introduce the effective area, $A_{effective}$, the area perpendicular to L_1:

$$A_{effective} = Asin\alpha \tag{4.43}$$

with α =35.26^o, the angle between [110] and [111]. The Burgers vector is also at an angle and only the component in the L_1 direction should be considered:

$$\bar{b}_{effective} = \bar{b}cos\alpha \tag{4.44}$$

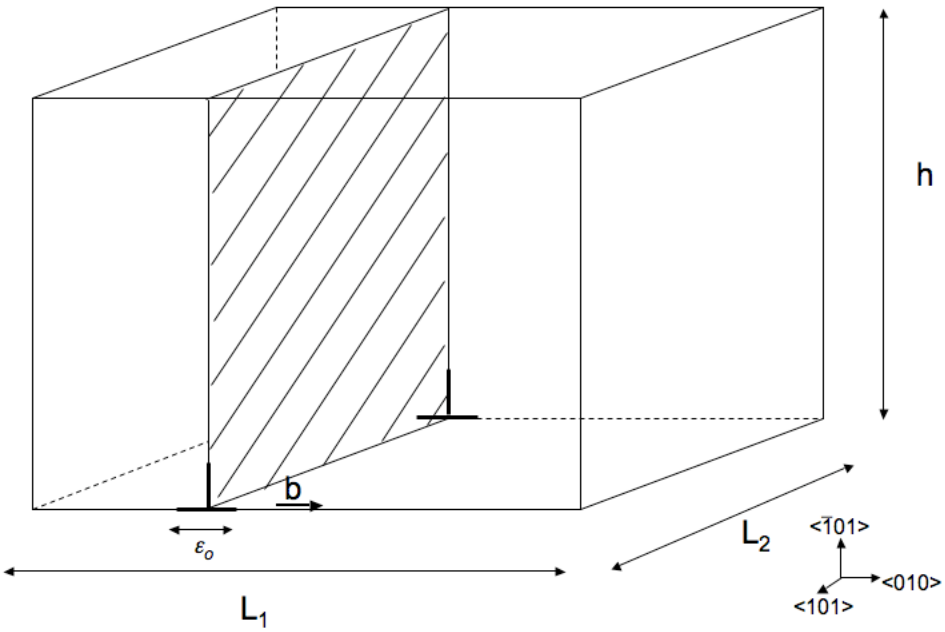

Figure 4.17: Parameters for the strain relieved by an edge dislocation in 3D

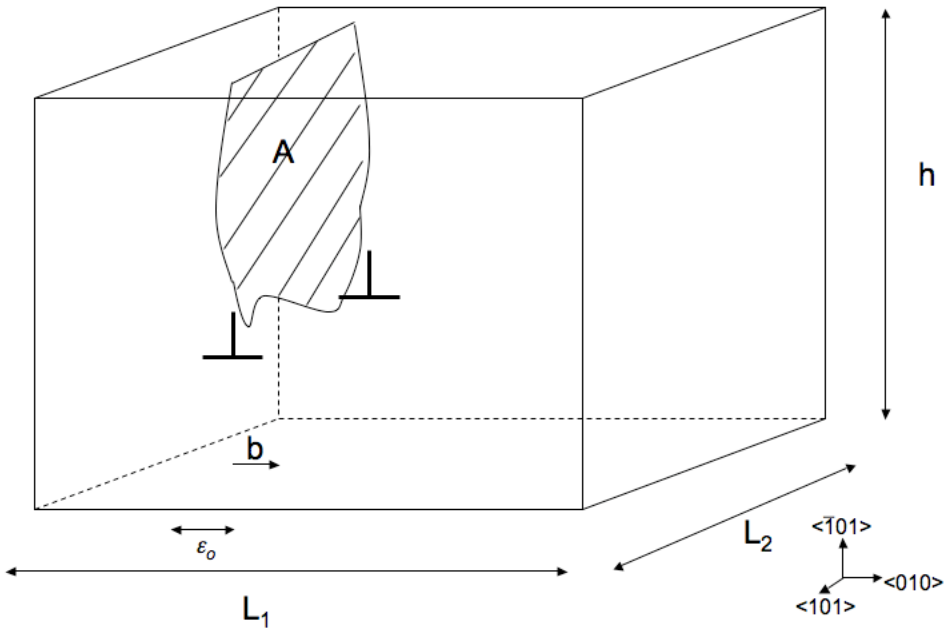

Figure 4.18: Dislocation with an irregular half plane with area A.

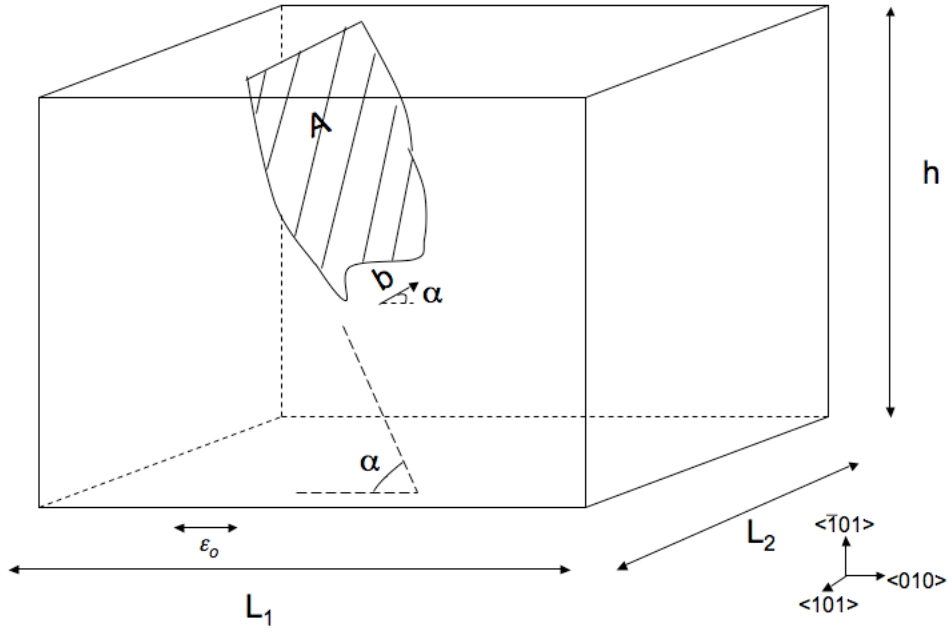

Figure 4.19: Edge dislocation with a general half plane comes in at an angle α to the template.

Therefore we get:

$$\Delta\varepsilon = \frac{bcos\alpha Asin\alpha}{V} \tag{4.45}$$

Since the volume, V, depends on the height, which in turn depends on time, as the crystal grows during the experiment, Equation 4.25 needs to be applied. The strain relieved by the dislocation is shown in Figure 4.20

The dislocation relieves $\sim 8.3\times10^{-4}$ of strain at its first move forward. Then it remains in the same position until it builds up again to relieve another $\sim 9.9 \times 10^{-4}$. As it is now stuck at the twin boundary, more strain energy needs to build up before it can penetrate through the boundary. It finally relieves another $\sim\ 4.0 \times 10^{-4}$. Figure 4.21 shows all the stacking faults. Each stacking fault has been colored to be easily tracked through the strain relief process. Figure 4.22 shows the strain relief for each stacking fault.

About the same time as the penetrating dislocation makes its first move, another dislocation makes a large contribution to strain relief, relieving $\sim 6\times10^{-3}$ in as short time as 100 min (black). Another dislocation relieves almost $\sim\ 2 \times 10^{-3}$ during this same time. This could be the reason why the penetrating dislocation does not make the jump towards the boundary all at once. Instead, it makes its first initial jump and then needs to wait for the crystal to build up more strain. When it finally does make another jump, it has very little competition from the stacking faults around it. Only one of the other stacking faults relieves a slight amount of strain during this time (purple). However, one stacking fault decreases slightly, or heals,

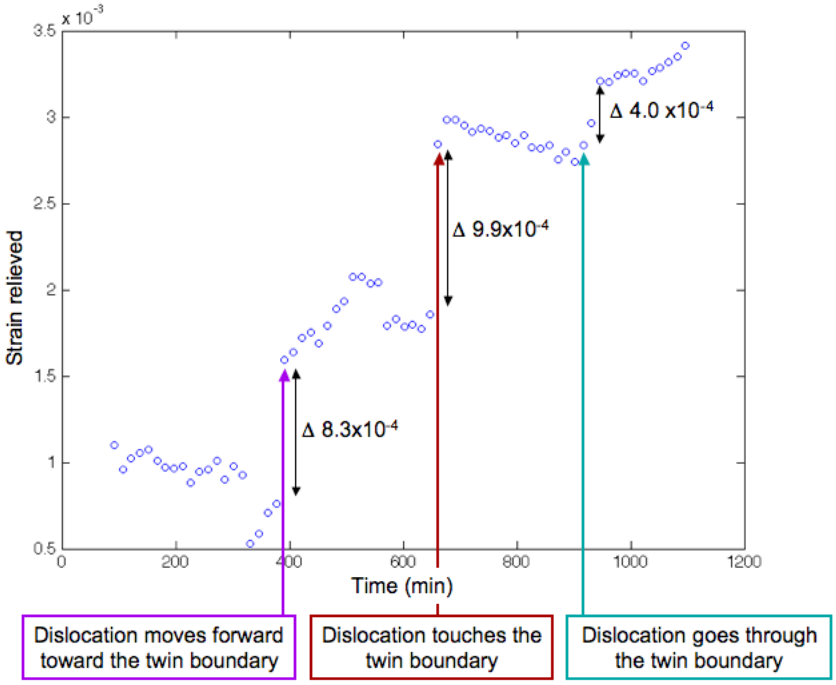

Figure 4.20: The strain relieved by the dislocation versus time.

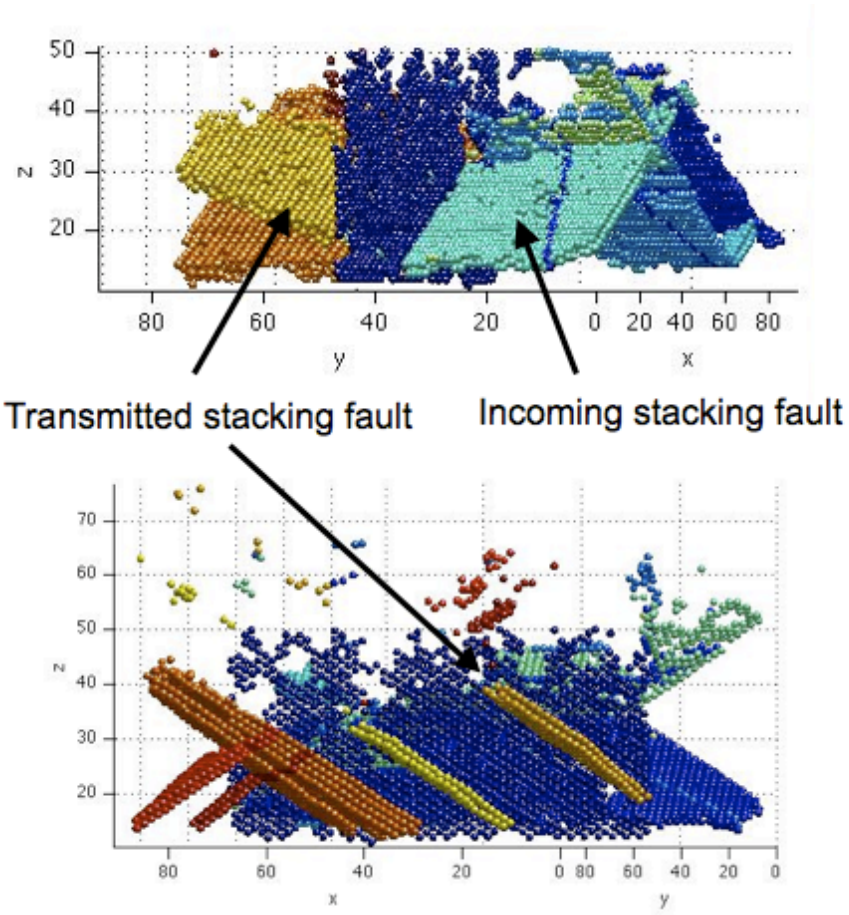

Figure 4.21: Each stacking fault in the sample has been identified and drawn with separate colors. The incoming and transmitted stacking faults in Figures 4.6, 4.7, and 4.8 are indicated.

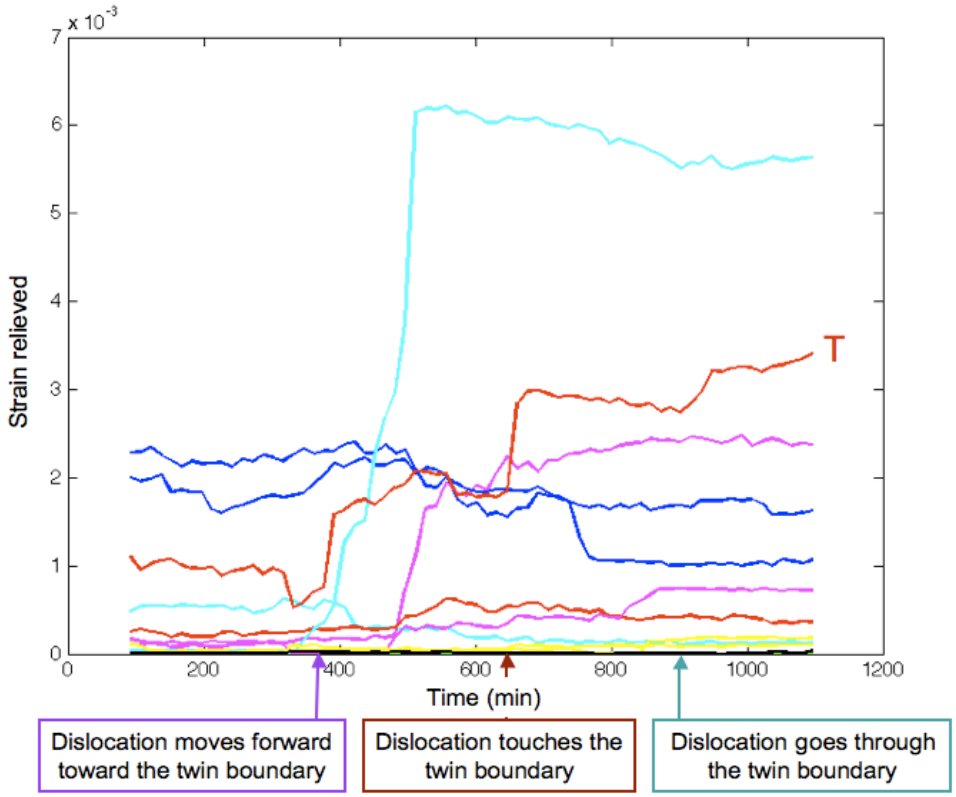

Figure 4.22: Strain relief versus time by each stacking fault in the sample. The stacking fault that penetrates the twin boundary is marked T.

shortly thereafter. In order to get a full picture of the strains evolution the cumulative strain of all stacking faults is plotted in Figure 4.23. Here we can clearly see how the second jump comes after there has been a decline in strain relief (or an increase in strain energy due to crystal growth without any relief from the dislocations.)

4.2.6 Dislocation Dynamics

The force that drives the motion of dislocations is the Peach-Koehler force, F_{PK}. In Figure 4.24 we can see how it drives the dislocation to expand in all directions.

$\bar{F}_{PK}$ depends on the Burgers vector, $\bar{b}$, the external stress, $\bar{\bar{\sigma}}$, and the length of the dislocation, $d\bar{s}$, that the force is acting on:

$$\bar{F}_{PK} = (\bar{\bar{\sigma}} \cdot \bar{b}) \times d\bar{s} \tag{4.46}$$

For motion to occur, the Peach-Koehler force must overcome the drag force and the line tension. Figure 4.25 shows a force balance diagram, from which we get:

$$F_{PK} = F_d + 2F_l \tag{4.47}$$

In our case, the dislocation grows in the <101> direction, bounded by the template and the free surface above, as seen in Figure 4.26. Therefore, we only have one line tension to consider in our force balance equation:

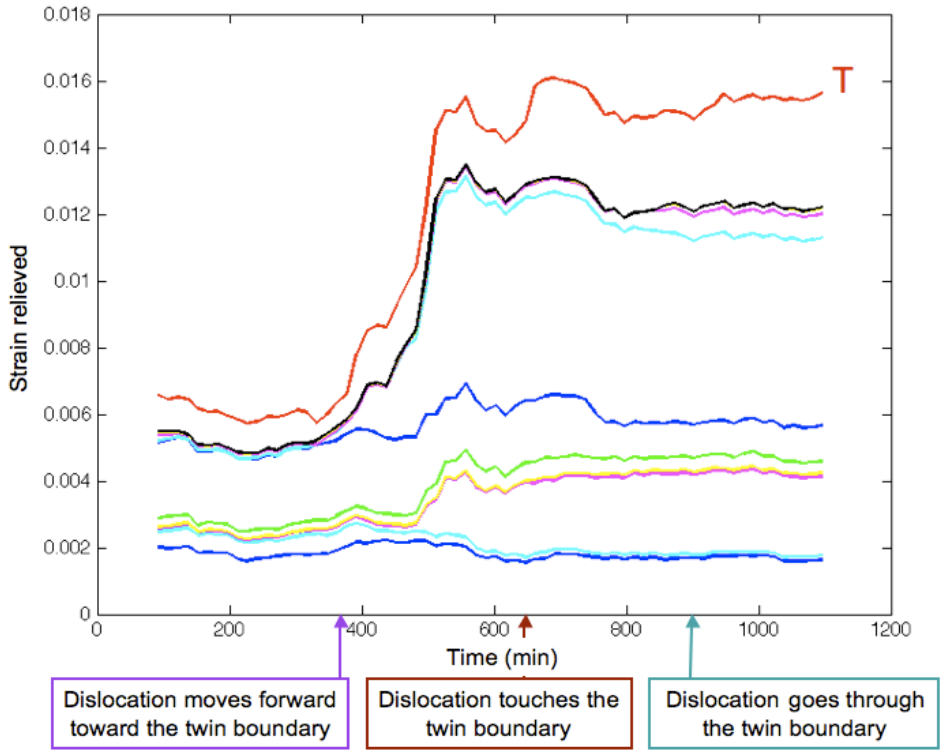

Figure 4.23: Cumulative strain relief versus time by each stacking fault in the sample. The stacking fault that penetrates the twin boundary is marked T.

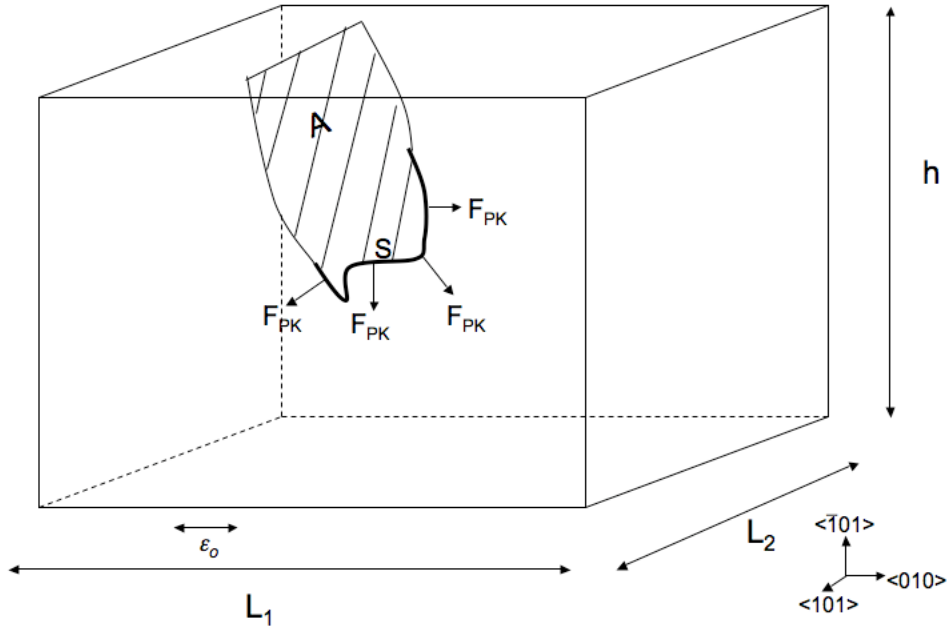

Figure 4.24: The dislocation moves forward due to the Peach-Koehler force, F_{PK}, acting on all sides.

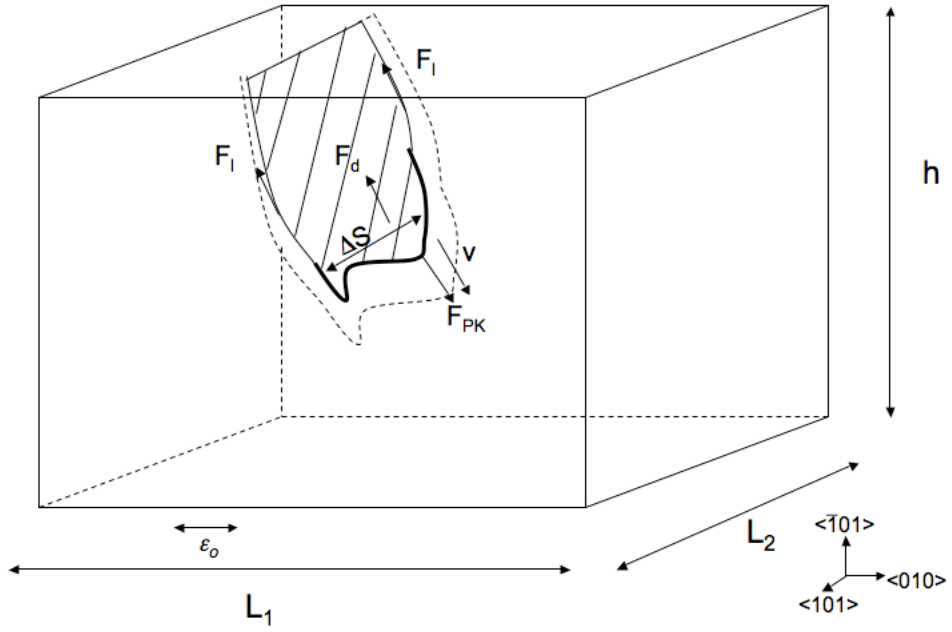

Figure 4.25: The Peach-Koehler force, F_{PK}, is balanced by the line tension, F_l, and the drag force, F_d.

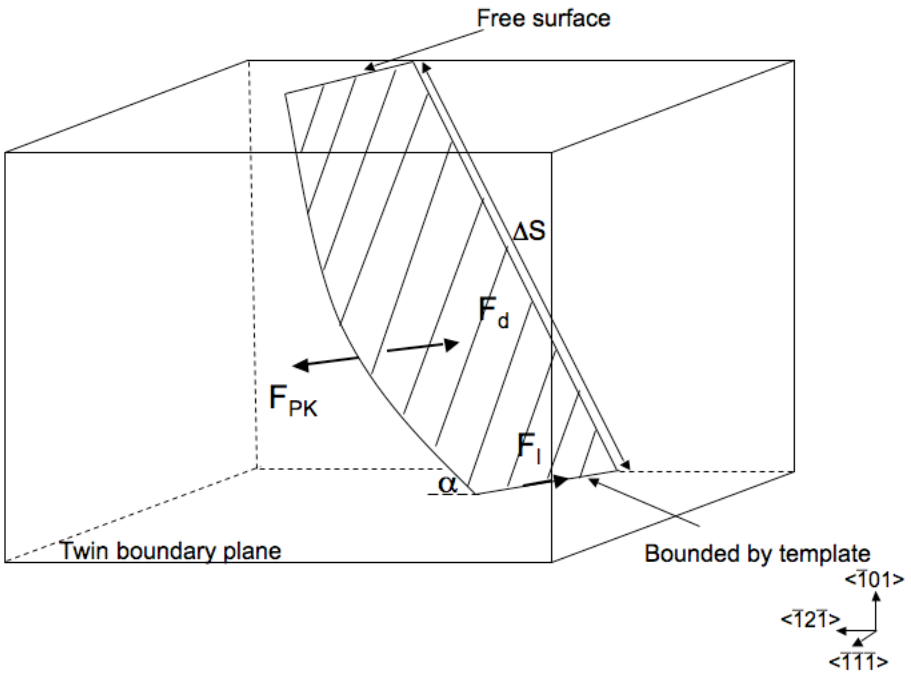

Figure 4.26: The dislocation of interest coming in towards the twin boundary.

$$F_{PK} = F_d + F_l \tag{4.48}$$

The drag force has been calculated as [46]:

$$F_d = \frac{4\eta}{\pi}\Delta S v \tag{4.49}$$

where ΔS is the width of the stacking fault perpendicular to the direction of motion of the dislocation, which here is about 50 μm. η is 1.6×10^{-3} Pa.s [17] and the velocity was calculated for both the transmitted and reflected dislocation (See Figure 4.27) and found to have a maximum at 0.9 μm/min. We obtain a magnitude of the drag force of 1.5×10^{-15} N.

An approximate expression for the line tension is [13]:

$$F_l = \frac{1}{2}\mu b^2 \tag{4.50}$$

With $\mu = 2$ Pa and $b = 0.81\mu$m, the line tension is 6.5×10^{-13} N, two orders of magnitude larger than the drag force. We will therefore ignore the drag force in the force balance equation.

An approximate expression for Peach-Koehler force is:

$$F_{PK} = \sigma\, b\, \Delta S \tag{4.51}$$

where the $\sigma = \mu\Delta\varepsilon = \mu(\varepsilon_o - \varepsilon)$. Using Equation 4.48 and solving for strain we get:

$$\Delta\varepsilon = \frac{\frac{1}{2}\mu b^2}{\mu b \Delta S} = 8 \times 10^{-3} \tag{4.52}$$

which is the strain needed to drive the motion of the dislocation. Since the strain relieved by the stacking faults is $\varepsilon = 0.016$, the remaining strain, $\varepsilon_o - \varepsilon$

= 0.045-0.016 = 0.029, is clearly sufficient to drive dislocation motion.

When the dislocation goes through the boundary, the work done by the Peach-Koehler force needs to supply the energy for two more dislocation of length ΔS, one that stays at the boundary and one that goes through. Define the length the dislocation travels when it goes through the boundary as Δr. The work done by the F_{PK} on the transmitted dislocation is $F_{PK}\Delta r$; the work done on the reflected dislocation is $F_{PK}2\Delta r$, since it travels about twice as far as the transmitted one (Figure 4.16) and it has the same Burgers vector. The total work balance is then:

$$F_{PK}(3\Delta r) = T(3\Delta r) + 2T\Delta S \tag{4.53}$$

Solve for F_{PK} per unit length:

$$\frac{F_{PK}}{\Delta S} = \frac{T}{\Delta S} + \frac{2T}{3\Delta r} \tag{4.54}$$

$\frac{T}{\Delta S}$ is found above to be $8 \times 10^{-3}\mu b$ N/m, hence the strain needed for the dislocation to go through the boundary, $\Delta\varepsilon_b$, is:

$$\Delta\varepsilon_b = 8 \times 10^{-3}(1 + \frac{2\Delta S}{3\Delta r}) \tag{4.55}$$

Δr can be found in Figure 4.16 to be about 12 μm.

Equation 4.55 tells us that the strain needed is 0.030. This value is close to the remaining strain in the lattice ($\varepsilon_o - \varepsilon$=0.029). Most likely, the reason for the dislocation to hold up at the boundary is the need to build-up a small amount of extra strain (by growth, see Figure 4.20) to make nucleation of the new dislocations possible.

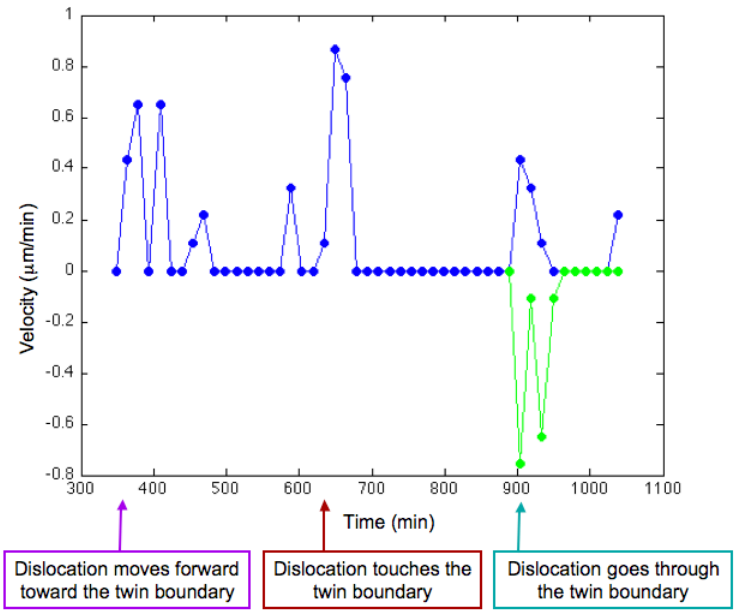

Figure 4.27: Dislocation velocities between the 15 min time steps. Blue indicate the dislocation moving forward. Green indicates the dislocation moving backwards.

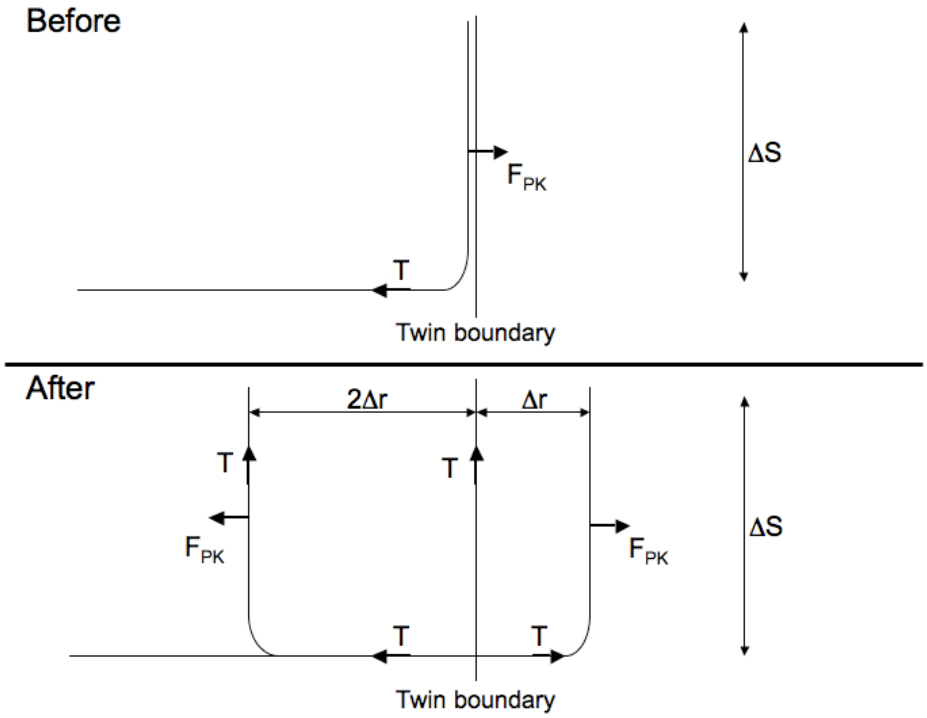

Figure 4.28: The dislocation configuration before and after penetration through the boundary.

5
Conclusions

THIS THESIS HAS SHOWN HOW colloids can be used to study the complex dynamics of defects in hard-sphere crystals.

The vacancies and divacancies in the colloidal hard-sphere crystals studied here are not in equilibrium, since no movement of single vacancies is observed. The lack of mobility is consistent with the extrapolation of earlier simulations at lower densities.

The volume of relaxation of the vacancy has a plausible value for these densities as the volume of formation is approaching the volume in a close-packed crystal. The volume of relaxation for the divacancy is smaller than that of two vacancies, so that the association of two vacancies into a divacancy requires extra volume, and hence extra entropy.

The mean square displacement of the nearest neighbors of the vacancies is an order of magnitude larger than that of the nearest neighbors of

particles.

The mobility of the divacancies is consistent with the extrapolation of older simulations and is similar to that associated with the annihilation of the vacancy-interstitial pair. The volume of motion of the divacancies is $\Delta V_m = 0.19 V_o$ (V_o: close-packed volume) and the entropy of motion is $\Delta S_m = 0.49 k_B T$.

Dislocation-twin boundary interactions can be observed by introducing strain via a misfit template. The dislocations formed are Shockley partials. When a dislocation goes through the boundary, two more dislocations are created: a reflected dislocation and one left at the boundary, both with the same magnitude Burgers vector.

The dislocations relieve a total of about a third of the misfit strain. The remaining strain is sufficiently large to move the dislocation up to the boundary and close to sufficient to move the dislocation through the boundary. A small amount to extra strain energy is needed to cause nucleation of the two additional dislocations after a waiting time.

6
Appendix A

This appendix is a supplement to explain the procedure to produce templates.

6.1 Mask Manufacturing

Templates are made by lithography where UV light shines through a patterned mask and replicates the structure. The first step in template production is manufacturing of the masks.

6.1.1 The design of the pattern

The mask production starts with designing the desired pattern in the computer programs Microsoft word and LayOutEditor. A special script is used where position and diameter of the holes are specified in a .cif file (written in Word but saved as .cif.) Below is an example:

```
DS 1 1 1
L CM;
R 105 50 50
DF;

DS 2 1 1
L CM:
C 1 T 100 100
C 1 T 100 200
C 1 T 100 300
DF;

E
```

The first four lines determine the size of the holes (starting with DS 1 1 1) and the rows that follow determine the locations of the holes (starting with DS 2 1 1). The file always ends with an E. In this code a hole with diameter 105 is repeated three times in a vertical row with spacing 100. The specific locations are:

x	y
150	150
150	250
150	350

The .cif file is read when opened in LayOutEditor with a desired scaling factor. In the example above the scaling factor is $a \times 10^{-4}$, where a is the

desired lattice spacing in μm. This is not translatable to a 105×1.63 μm radius on the final template, as one might think. Instead the radius will later be determined by the two exposure times: the laser exposure time on the mask and the UV light exposure time on the template. Other factors also play a role as will be discussed below. However, the number is not arbitrary. In our case a ratio of 1.05 between the radius and the spacing was ideal. When the code is written, the .cif file can be opened in LayOutEditor and the pattern will be drawn. At this point it is useful to check that the distances between the holes and the ratio of diameter/spacing of the holes are as desired. This is also where a conversion from .cif to .gds is made. The mask machine prefers .gds files.

6.1.2 Writing the pattern

The mask maker used throughout this work was the Heidelberg TM mask maker (DWL66). A 2 mm write head directs the laser to print the pre-designed pattern on a chrome-coated glass substrate. Two filters (1% and 50%) are placed to block some of the intensity of the laser. If these filters are not in place, a dense, micrometer precision pattern will not be easily obtained. However, it does not matter which order they are placed in. One can chose to do one pattern at a time, repeat the pattern multiple times, or draw different patterns on the same mask. The limit of size on one specific pattern is the amount of time it takes to upload the .gds file to the computer. A large pattern takes hours, sometimes days, so smaller patterns are preferred. Therefore, it can be ideal to repeat the same patterns right next to each other to obtain a large but more manageable mask construction. A maximum of 25 patterns can be written in one run. Our patterns have

mostly been sub 5×5 mm^2 and repeated if needed. There are two main parameters that determine the quality of the pattern, the defocus and the energy. The optimal values of each depend on the age and alignment of the laser. Therefore, a test run is required where a small pattern is written multiple times with defocus ranging from 1500 to 1900 and energy ranging from 70 to 110. After the test mask has been developed and etched, the ideal defocus and energy can be determined under the microscope.

6.1.3 Developing and etching the pattern

After the substrate has been exposed to the laser it is time for developing the substrate in 1 part MF351 and 2 parts water for 2-3 min. The substrate is rinsed with water immediately afterwards and then blow-dried with air. One could use this opportunity to examine the pattern under a microscope but this should only be done in the event that something is wrong with the laser exposure or developing step. This is because the microscope light destroys the chrome. If the substrate has not been exposed to a microscope, the next step is to etch in a chromium etching solution 1020 for 3-3.5 min. The time varies depending on the intensity of the laser, the age of the substrate, and the desired radius of the holes. Finally, the substrate is rinsed in water immediately and dried with blowing air. A microscope with light shining from underneath will reveal how well the UV light goes through the mask. If the crome is not completely gone, little or no light will shine through. In this case, the developing time was too short or the energy of the Heidelberg TM was too low.

6.2 Template Processing

VWR micro cover glass slides No. 1.5 are first cleaned for 10 min in acetone, 10 min in methanol, and blow-dried with air. The next step is to coat the slides with a photoresist. In order to get the photoresist to stick to the glass a layer of primer is first spin-coated for 5 seconds at 500 rpm and then 40 seconds at 4000 rpm. Directly thereafter a layer of photoresist Shipley S1805 was spin-coated for the same amount of time and at the same rpm. The glass slide is placed on a 110^{o}C hot plate for 3 min in order to polymerize. The slide is placed in a mask aligner (Suss TM MJB3) for 2-2.5 sec together with the mask. The slides are developed in 1 part MF 351 and 5 parts water for 60-90 sec. Both the exposure time and the developing time vary due to the hole size in the mask, the age of the photoresist, calibration of the mask aligner, and the premixed developer. Usually a few tries are required each time to determine the ideal procedure. (One efficient way to do this is to expose the same glass slide with different exposure times next to each other before developing.) After developing, the slides are dropped into water for 60 seconds and blown-dried with air. For etching the a reactive ion etcher (STS ICP RIE 8) was used. To start off, the chamber needs to be treated with oxygen cleaning plasma for 20 min. Then the RIE will perform 8-10 min etching on the slides, which are attached to a glass wafer with thermal paste. After 10 min oxygen cleaning plasma is introduced again to remove the photoresist from the slide, without etching the glass any further. Once the thermal paste is fully removed with isopropanol the templates are ready to be used. As for the developing time, the etching time is also dependent on the pattern and the quality of the photoresist. The smaller the radii the

longer etching time is required to create deep enough holes for the colloids to fall into (see Section2.2.4 in Chapter 2). It is not a problem if the holes are too deep, and as long as the photoresist is not etched away, little variation in diameter is found with increasing etching time. Figure 6.1 shows a layout of the template processing and Figure 6.2 shows the result of a 110 template.

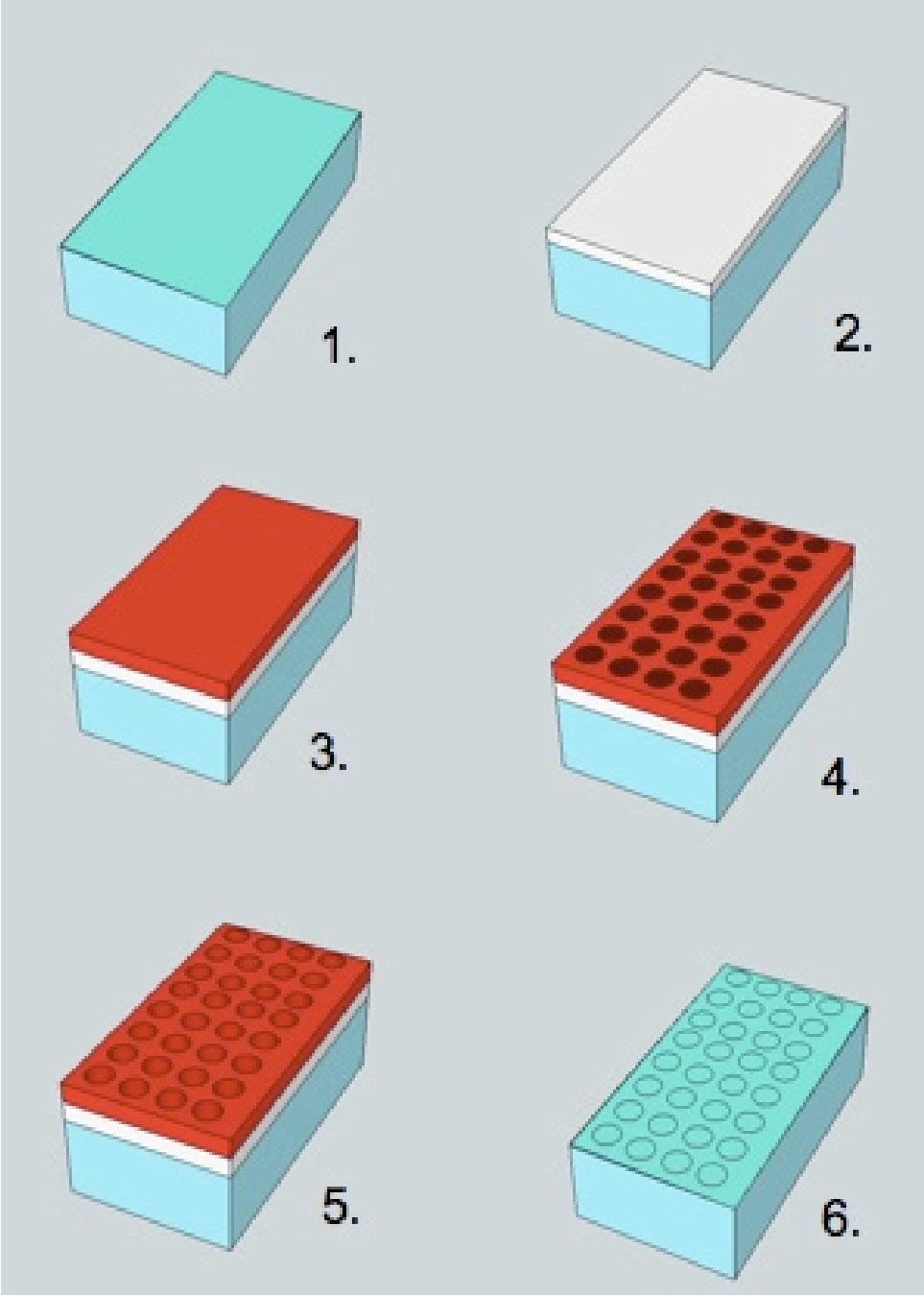

Figure 6.1: Templates are produced in multiple steps: 1) The glass slide is cleaned in acetone and methanol; 2) a primer is spin-coded on top of the glass slide; 3) a layer of photoresist is spin-coded on top of the primer; 4) the glass slide is exposed to UV light; 5) the glass slide is developed to remove the exposed photoresist; 6) the glass slide is etched and the photoresist is removed.

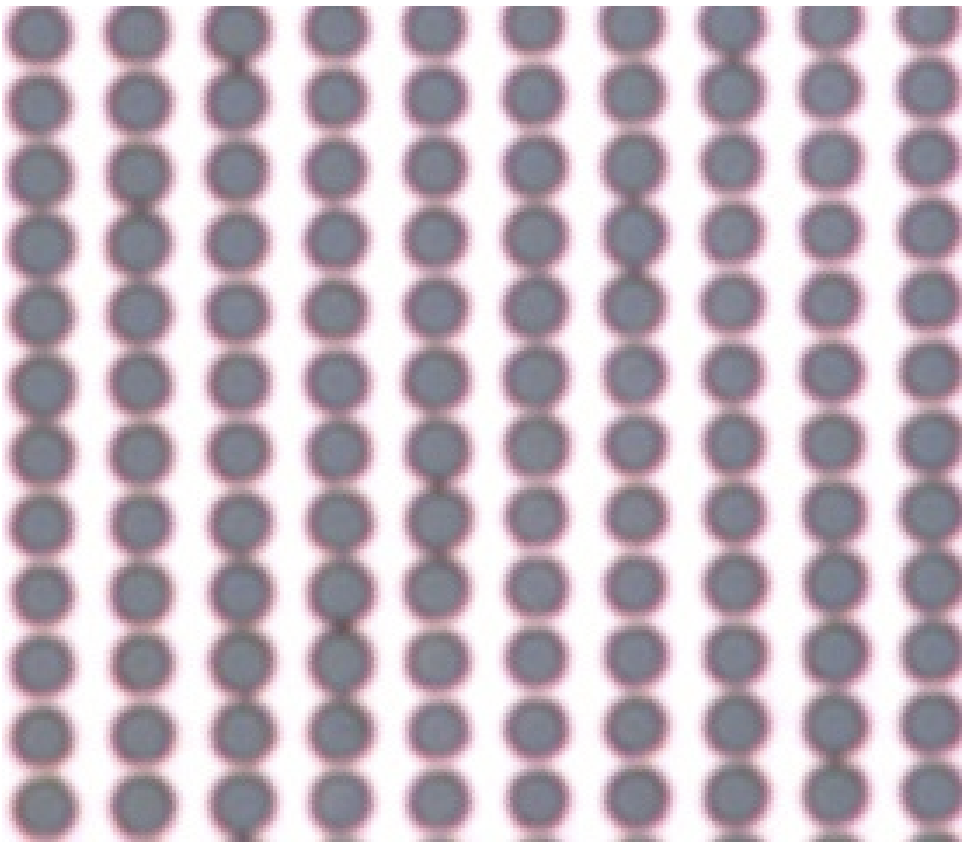

Figure 6.2: Microscope image of a 110 template.

7 Appendix B

This appendix is a supplement to explain image processing used in Chapter 3 and 4 .

7.0.1 Image processing

The raw data from the confocal microscope is processed using Maria Kilfoil's MATLAB package to find particle centers in 3D. [47] (The package can be found at http://people.umass.edu/kilfoil/downloads.html). The are three functions used in this thesis:

1) read_xyz reads in a set of images into MATLAB.

2) bpass3dMB preforms a 3D mask on the raw images to find the center of each particle by labeling it with the most intense pixels.

3) feature3dMB obtains the coordinates of these centers.

There are four code lines written in order to obtain these centers:

XYZ = read_xyz(Foulder,NameOfFiles,[z_start,z_end]);

XYZ=255-XYZ; %(To invert the image and give the center the max intensity)

res=bpass3dMB(XYZ,lnoise,lobject,inputv);

r=feature3dMB(res,diameter,masksz,xyzmax,inputz,sep,masscut,threshold);

The images' pixels intensity ranges from 0 to 255, 2^8 possible values, indicating a range of photons hitting detecter at that specific scanned point. When the 3D mask is performed, using the bpass3dMB function, weighted numbers of intensity from the considered pixels of the mask are summed up, leaving a possible intensity larger than 255.

For detailed descriptions of the parameters above, see the website. The parameter values will be presented in the relevant chapters with exception of the few that do not change between the different data-sets:

inputv=[0 0];

inputz = [1 0 1];

masscut = 0;

threshold = 0.1;

The stored variable r will give the coordinates in pixels. The confocal microscope gives a conversion between pixels and μm for each data-set. This conversion will also be presented in relevant sections.

References

[1] A. van Blaaderen, R. Ruel, and P. Wiltzius, "Template-directed colloidal crystallization," *Nature*, vol. 385, pp. 321–324, 1997.

[2] P. N. Pusey, W. van Megen, P. Bartlett, and B. J. Ackerson, "Structure of crystals of hard colloidal spheres," *Phys. Rev. Lett.*, vol. 63, no. 25, pp. 2753–2756, 1989.

[3] L. Bragg and J. F. Nye, "A dynamical model of a crystal structure," *The Royal Society: Series A. Math. and Phys. Sci.*, vol. 190, no. 1023, pp. 474–481, 1947.

[4] P. Schall, I. Cohen, D. A. Weitz, and F. Spaepen, "Visualization of dislocation dynamics in colloidal crystals," *Science*, vol. 305, pp. 1944–1948, 2004.

[5] E. Maire, M. Persson Gulda, N. Nakamura, K. Jensen, E. Margolis, C. Friedsam, and F. Spaepen, "Three dimensional confocal microscopy study of boundaries between colloidal crystals," *Optical Measurements, Modeling, and Metrology*, vol. 5, pp. 69–74, 2011.

[6] P. Schall, I. Cohen, D. A. Weitz, and F. Spaepen, "Visualizating dislocation nucleation by indenting colloidal crystals," *Nature*, vol. 440, pp. 319–323, 2006.

[7] A. D. Dinsmore, E. R. Weeks, V. Prasad, A. C. Levitt, and D. A. Weitz, "Three-dimensional confocal microscopy of colloids," *Applied Optics*, vol. 40, pp. 4152–4159, 2001.

[8] C. H. Bennett and B. J. Alder, "Studies in molecular dynamics. ix. vacancies in hard sphere crystals," *J. Chem. Phys.*, vol. 54, pp. 4796–4808, 1971.

[9] S. Pronk and D. Frenkel, "Point defects in hard sphere crystals," *J. Phys. Chem. B*, vol. 105, pp. 6722–6727, 2001.

[10] W. Lee, A. Chan, M. A. Bevan, J. A. Lewis, and P. V. Braun, "Nanoparticle-mediated epitaxial assembly of colloidal crystal on patterned substrates," *Langmuir*, vol. 20, pp. 5262–5270, 2004.

[11] P. Mullner and C. Solenthaler, "On the effect of deformation twinning on defect densities," *Mater. Sci. and Eng. A*, vol. 320, pp. 107–115, 1997.

[12] E. A. Marquis, L. Douglas Medlin, and F. Leonard, "Stabilization of extended stacking faults by {1 1 1}/{1 1 2} twin junction interactions," *Acta Mater.*, vol. 55, pp. 5917–5923, 2007.

[13] J. P. Hirth and J. Lothe, "Theory of dislocations," 1982.

[14] X. Zhang, A. Misra, H. Wang, M. Nastasi, T. Embury, E. Mitchell, R. G. Hoagland, and J. P. Hirth, "Nanoscale-twinning-induced strengthening in austenitic stainless steel thin lms," *App. Phys. Lett.*, vol. 84, no. 7, pp. 1096–1098, 2004.

[15] Y.-H. Zhao, X.-Z. Liao, S. Cheng, E. Ma, and Y. T. Zhu, "Simultaneously increasing the ductility and strength of nanostructured alloys," *Adv. Mater.*, vol. 18, pp. 2980–2283, 2006.

[16] Y. Wang, M. Chen, F. Zhou, and E. Ma, "High tensile ductility in a nanostructured metal," *Nature*, vol. 419, pp. 912–915, 2002.

[17] K. E. Jensen, D. Pennachio, D. Recht, D. A. Weitz, and F. Spaepen, "Rapid growth of large, defect-free colloidal crystals," *Soft matter*, 2012.

[18] P. Schall and F. Spaepen, "Dislocations in solids: Chapter 96 dislocations in colloidal crystals," vol. 16, pp. 233–261, 2010.

[19] W. G. Hoover and F. H. Ree, "Melting transition and communal entropy for hard sphere," *J. Chem. Phys.*, vol. 49, pp. 3609–3617, 2009.

[20] W. K. Kegel and A. van Blaaderen, "Direct observation of dynamical heterogeneities in colloidal hard-sphere suspensions," *Science*, vol. 287, no. 5451, pp. 290–293, 2000.

[21] L. V. Woodcock, "Glass transition in the hard-sphere model and kauzmann's paradox," *Ann. N.Y. Acad. Sci., year = 1981, volume = 371, number = , pages = 274–298,.*

[22] J. L. Finney, "Random packings and the structure of simple liquids. i. the geometry of random close packing," *Proc. Roy. Soc. A.*, vol. 319, pp. 479–493, 1970.

[23] B. J. Alder and T. E. Wainwright, "Studies in molecular dynamics. ii. behavior of a small number of elastic spheres," *J. Chem. Phys*, vol. 33, no. 5, pp. 1439–1451, 1960.

[24] K. R. Hall, "Another hard-sphere equation of state," *J. Chem. Phys.*, vol. 57, pp. 2252–2254, 1972.

[25] M. H. Chestnut, "Confocal microscopy of colloids," *Current Opinion in Colloid and Interface Science*, vol. 2, no. 2, pp. 158–161, 1997.

[26] S. M. Allen and E. L. Thomas, "The structure of materials," pp. 251–253, 1999.

[27] S. Pronk and D. Frenkel, "Large effect of polydispersity on defect concentrations in colloidal crystals," *J. Chem. Phys.*, vol. 120, pp. 6764–6769, 2004.

[28] S. P. Singh, C. Kaur, and S. P. Das, "Optimum vacancy concentration in a crystal," *Phys. Rev. E*, vol. 72, pp. 021603–1–021603–5, 2005.

[29] R. W. Balluffi, S. M. Allen, and W. Craig Carter, "Kinetics of materials," 2005.

[30] A. Kelly, G. W. Groves, and P. Kidd, "Crystallography and crystal defects," pp. 285–291, 2000.

[31] Data-set taken by Dan Pennachio, a REU summer student in Professor Spaepen's lab who was supervised by Katharine Jensen.

[32] K. E. Jensen, D. A. Weitz, and F. Spaepen, "A three-dimensional calibration device for the confocal microscope.," *(submitted).*

[33] M. V. Jaric and U. Mohanty, "Density-fuctional theory of elastic moduli: Hard-sphere and lennard-jones crystals.," *Phys. Rev. B*, vol. 37, no. 9, pp. 4441–4457, 1988.

[34] F. Seitz and D. Turnbull, "Solid state physics advances in research and applications.," vol. 3, pp. 107–108, 1956.

[35] D. R. Nelson and F. Spaepen, "Polytetrahedral order in condensed matter," *Solid State Physics*, vol. 42.

[36] D. Turnbull and M. H. Cohen, "On the free-volume model of the liquid-glass transition," *J. of Chem. Phys.*, vol. 52, no. 6, pp. 3038–3041, 1970.

[37] J. Schiotz and K. W. Jacobsen, "A maximum in the strength of nanocrystalline copper," *Science*, vol. 301, pp. 1357–1359, 2003.

[38] D. Y. W. Yu and F. Spaepen, "The yield strength of thin copper films on kapton.," *J. of App. Phys*, vol. 95, no. 6, pp. 2991–2997, 2004.

[39] J. R. Youngdahl, C. J anf Weertman, R. C. Hugo, and H. H. Hung, "Deformation behavior in nanocrystalline copper," *Scripta Mater.*, vol. 44, no. 8-9, pp. 1475–1478, 2001.

[40] W. J. Babyak and F. N. Rhines, "The relationship between the boundary area and hardness of recrystallized cartridge brass," *Trans. Metal. Soc.*, vol. 218, no. 1, pp. 21–23, 1960.

[41] Y. F. Shen, L. Lu, Q. H. Lu, Z. H. Jin, and K. Lu, "Tensile properties of copper with nano-scale twins," *Scripta mater*, vol. 52, pp. 989–994, 2005.

[42] L. Remy, "Twin-slip interaction in f.c.c. crystals," *Acta Metallurgica*, vol. 25, pp. 711–714, 1977.

[43] V. Yamakov, D. Wolf, S. R. Phillpot, and H. Gleiter, "Dislocation-dislocation and dislocation-twin reationc in nanocrystalline al by moleculer dynamics simulations," *Acta Mater.*, vol. 51, pp. 4135–4147, 2003.

[44] L. Remy, "Twin-twin interaction in fcc crystals," *Scripta Metallurgica*, vol. 11, no. 3, pp. 169–174, 1977.

[45] I. B. Ramsteiner, K. E. Jensen, D. A. Weitz, and F. Spaepen, "Experimental observation of the crystallization of hard-sphere colloidal particles by sedimentation onto at and patterned surfaces," *Phys. Rev. E*, vol. 79, no. 011403, 2009.

[46] M. Jorand, F. Rothen, and J. Pieranski, "Dislocation motion in colloidal crystals," *J Physique C3*, vol. 46, no. 3, p. 245, 1985.

[47] Y. Gao and M. L. Kilfoil, "Accurate detection and complete tracking of large population of features in three dimensions," *Optics Express*, vol. 17, no. 6, pp. 4685–4704, 2009.

Colophon

This thesis was typeset using LaTeX, originally developed by Leslie Lamport and based on Dan Recht's TeX. A template that can be used to format a PhD thesis with this look and feel is freely available online at `https://github.com/suchow/`.